Radiation impact of collimation beam losses in the LHC and HL-LHC

Eleftherios Skordis

Department of Physics

University of Liverpool

This dissertation is submitted for the degree of

Doctor of Philosophy

University of Liverpool 2019

I would like to dedicate this thesis to my wife and daughter as well as my loving parents and sister.

Declaration

I hereby declare that except where specific reference is made to the work of others, the contents of this dissertation are original and have not been submitted in whole or in part for consideration for any other degree or qualification in this, or any other University. This dissertation is the result of my own work and includes nothing which is the outcome of work done in collaboration, except where specifically indicated in the text. This dissertation contains less than 65,000 words including appendices, bibliography, footnotes, tables and equations and has less than 150 figures.

Eleftherios Skordis

2019

Acknowledgements

Now, more than ever, the progress of human knowledge rests in the shoulders of the many working together to expand the frontier of the unknown. While a thesis dissertation might often seem to be a lonely path it is always the culmination of the fruitful interactions of the author with his peers.

To begin with, I would like to thank my professor and supervisor Prof. Dr. Carsten P. Welsch, for entrusting me to embark in this journey as a doctoral student in the University of Liverpool as well as for his guidance and experience that he transferred to me. Furthermore, I want to express my deep gratitude to Dr. Anton Lechner, for his supervision and collaboration at CERN as well as the valuable time he spent on the betterment of the current document.

For all the helpful advice and productive discussions, I would like to thank Dr. Francesco Cerutti and Dr. Vasilis Vlachoudis offering technical and theoretical solutions at times where they were needed the most.

Furthermore, I am very thankful to all my colleagues at the Beam Matter Interactions section at CERN, with whom I enjoyed both working and spending quality coffee time. I acknowledge the great body of work that has been performed by previous members of the section which became the foundations on top of which I built this thesis. A special thanks goes to my officemates over the years, Dr. Alessio Mereghetti, Dr. Philippe Schoofs, Dr. Maria Ilaria Besana and Dr. Mohammad Varasteh with who I have had many hours of discussions about various topics that greatly contributed in enriching and developing a proper scientific mindset.

For all their support regarding the experimental data extraction from the LHC I acknowledge the great contribution of Dr. Oliver Stein, Mr Kacper Bilko and Dr. Ruben Garcia Alia.

For the valuable time spend in English proofing of the thesis I would like to give special thanks Dr. James Hunt former member of the QUASAR group and current member of the BMI section.

To my close friends, I am extremely grateful for their psychological and sentimental support over the troubled times and especially towards Dr. Vivian Anastasiou, MD Nick Fountoulakis, Dr. Anastasios Mangelis,, Dr. Zoi Paschalidi, MD Ioannis Tsoukakis and Dr. Vassia Vardakastani. To my extended family in Switzerland, Mrs Afroditi Skevi and Dr. Apostolos Perdikakis, I offer my gratitude for making the time abroad all the more familiar and closer to home.

To my father Ioannis Skordis, I owe a great debt for being there through the hardships and the happy times. He has been the greatest influence on who I am, and it always puts a smile to my face when I catch my self thinking “what would my father do?”. He really stepped up to fill the void left from the passing of my beloved mother Ioulia Skordi who raised me to be the man that I am today. I would also like to give special thanks to my mother in law, Evanthia Kastriotou, with whom I had the traditional mother-son quarrels that I missed so much.

I could not have been more grateful to have in my live my lovely sister Eleni Skordi together with my adorable nephews Konstantinos and Ioannis. I would like to sincerely thank her for all the support and comfort she has so generously offered to my family.

I would like to give special thanks to my mother in law, Evanthia Kastriotou, with who I had the traditional mother-son quarrels that I missed so much.

Last but not least, I started on this path together with my amazing and loving wife Dr. Maria Kastriotou without whose seer determination I would not have been able to reach the end of. She not only supported and helped me push through the hardest of times but also gifted me with an extra member in the family, my beautiful daughter, Lily. They say happiness when shared, is doubled, but I believe in our case it is at least a factor of three.

Abstract

Beam dynamics and Monte Carlo beam-matter interaction simulations play a vital role in the design and performance assessment of high-energy proton and ion colliders. The collimation system of the Large Hadron Collider (LHC) is leading by example with its proven ability to protect and assure an unobstructed operation during the past years. This thesis aims to further develop the complex simulation chain involved in the study of the collimation related beam losses as well as to accurately estimate its predictive capabilities. An unprecedented benchmark against Beam Loss Monitor (BLM) measurements is presented with extensive analysis of particle showers and their origins. Furthermore, the proton losses during the Run 2 operational period (2015-2018) in the betatron cleaning insertion region are estimated. Predictions for upcoming High Luminosity-LHC (HL-LHC) are made utilising a new scaling method based on the integrated proton intensity. The new scaling method and the proton loss estimates for Run 2 are benchmarked against passive dosimeter measurements during the same years. In addition, the tools are then applied in order to quantify the radiation impact that beam losses have in the collimation system itself as well as in the normal and Super-Conducting (SC) magnets. The short term radiation effects concerning the collimator material robustness and the power deposited in the SC coils are examined. Lastly, the long-term degradation of organic (dose) and crystalline materials (DPA), found in the magnets and collimator absorber blocks, respectively, are presented for the HL-LHC lifetime.

Contents

Contents xi
List of Figures xv
List of Tables xxi
Chapter 1 Introduction 1
Chapter 2 High energy accelerator collimation 3
2.1 The Large Hadron Collider 3
Layout 3
Superconducting magnets 5
Beam Loss Monitors 6
2.2 The collimation system of the LHC 6
Beam lifetime and particle loss rate 7
Collimator types 7
Collimator settings 10
2.3 Simulation tools and method 11
2.3.1 Software tools 11
MAD-X 11
Sixtrack 12
FLUKA 12
Sixtrack-FLUKA coupling 13
LineBuilder and the FLUKA Element DataBase 13
2.3.2 Physical quantities 14
Energy deposition 14
Dose 14
Displacement Per Atom 15
2.3.3 Simulation chain 15
Chapter 3 Simulation benchmark for betatron collimation losses 17
3.1 Introduction 17
3.2 Collimation quench tests 2015 18
3.2.1 Proton collimation quench test 19

3.2.2 Ion collimation quench test of 2015 21
3.3 Benchmark against the proton collimation quench test 24
3.3.1 SixTrack-FLUKA coupling tracking simulations for protons 24
3.3.2 FLUKA simulations for protons 28
Long straight section (warm section) 28
Simulation setup 29
BLM signal comparison 30
Dispersion Suppressor (cold section) 32
Simulation setup 33
BLM signal comparison 34
Loss contribution disentangling 35
3.4 Imperfection studies 36
3.4.1 Tracking studies 37
3.4.2 FLUKA simulations with TCP misalignment 40
3.5 Ion benchmark against BLMs 43
3.5.1 SixTrack-FLUKA coupling tracking simulations for ions 43
3.5.2 FLUKA simulations for ions 45
Simulation setup for ions 45
BLM comparison for the 2015 ion quench test 46
Long straight section (warm section) 46
Dispersion Suppressor (cold section) 48
3.6 Conclusion 50
Chapter 4 Run 2 betatron cleaning loss analysis and HL predictions 51
4.1 Introduction 51
4.2 Method for determining proton losses in the betatron cleaning insertion 52
4.2.1 Experimental data split into beam modes 52
4.2.2 Data analysis process 54
Data pre-processing 54
Data processing for proton loss evaluation 55
4.3 Evaluation of annual betatron losses in LHC Run 2 56
4.3.1 Top energy losses (6.5 TeV) 57
Beam 2 6.5 TeV losses for 2015-2018 57

Beam 1 6.5 TeV losses for 2015-2018 59
4.3.2 Injection energy losses (450 GeV) 61
Beam 2 Injection proton losses for 2015-2018 61
Beam 1 Injection proton losses for 2015-2018 63
4.4 Benchmarking annual loss values against passive dosimeter measurements 65
4.5 Loss scaling methods 69
Losses overview and luminosity scaling 69
New scaling quantity (time-integrated intensity) 72
4.6 Conclusion 76
Predictions of betatron collimation losses for the HL-LHC era 76
Chapter 5 Radiation impact on collimators 79
5.1 Introduction 79
Short term effects 79
Long term effects 80
5.2 Energy deposition sharing in IR7 81
5.3 Short term radiation impact on collimators 84
5.3.1 Study of the primary collimators 85
HL-LHC considerations 89
5.3.2 Study of the most impacted secondary collimator 91
5.4 Long-term displacement damage on collimator absorber blocks 98
5.4.1 Setup for calculating DPA in the collimator jaws 98
5.4.2 Primary collimators 100
Disentangling DPA contributions 100
Comparison of peak DPA levels 102
5.4.3 Secondary Collimator 104
Disentangling DPA contributions 104
Comparison of maximum DPA levels 105
5.5 Conclusion 106
Chapter 6 Radiation Impact on magnets 109
6.1 Introduction 109
Long term effects 109
Short term effects 110
6.2 Radiation-induced failures of normal conducting magnets 110

6.2.1 Warm Dipoles 114
6.2.2 Warm Quadrupoles 116
6.3 Quench margin for superconducting magnets 120
Evaluation of quench levels for 6.5 TeV 122
6.3.1 The 2015 proton quench test 123
6.3.2 The 2015 ion quench test 126
6.4 Conclusion 127
Long term effects 127
Short term effects 128
Chapter 7 Conclusions and outlook 131
References 1

List of Figures

Figure 2-1: LHC layout and insertion region description (1)..... 4

Figure 2-2: Cross section of an MB magnet of the LHC (10)..... 5

Figure 2-3: BLMs attached to the SC magnets (left) and to the primary collimators (right)(13). 6

Figure 2-4: Individual collimator jaw (left) and collimator assembly (right) with two jaws inside a collimator tank. An opening that the beam passes through exists between the two jaws (17). 8

Figure 2-5: Schematic representation of the LHC collimation system (18,19)..... 10

Figure 3-1: Left: Beam intensity during the proton quench tests in 2011-2015. Right: Power loss calculated from the BCT for the same years (40). 20

Figure 3-2: BLM signals measured at the moment of peak power loss of 585 kW during the 2015 proton quench test (40). 21

Figure 3-3: Intensity and power loss calculated from the BCT during the quench test (41). 22

Figure 3-4: BLM signals measured at the moment of maximum power loss of 15 kW during the 2015 lead ion quench test. The signals are normalized with respect to the maximum signal (41) 24

Figure 3-5: Tracking simulation proton loss map showing the location of protons impacting the beam pipe aperture or being lost in the collimators..... 25

Figure 3-6: Primary horizontal collimator (TCP.C) FLUKA geometry (left) and proton impact positions “touches” (right). (s=z) 26

Figure 3-7: (Top) LSS measurements vs simulations of BLM signals during the 2015 proton quench test. (Bottom) Equivalent FLUKA geometry of the IR7 LSS of the LHC..... 32

Figure 3-8: Geometry rendering of the last TCLA of beam 2 before the radiation shielding separating the warm and cold sections (right) Energy density map of the particles escaping the radiation shield (a.u) (left)..... 34

Figure 3-9: (Top) DS measurements vs simulations of BLM signals during the 2015 proton quench test. (Bottom) Equivalent FLUKA geometry of the IR7 long straight section of the LHC. 35

Figure 3-10: Measurements vs simulations of BLM signals in the DS during the 2015 proton quench test. The FLUKA patterns disentangle the contribution of high energy protons lost inside the SC magnet aperture and the contribution of upstream showers originating from outside the beam pipe. 36

Figure 3-11: Different misalignment scenarios with |θ|=200 μrad (53)..... 38

Figure 3-12: Beta function and sigma at the TCP (top). Sigma values with θ=200 μrad and incurred gap difference Δg (Bottom) (53) 39

Figure 3-13: Transverse impact parameter distribution on the primary horizontal collimator (TCP.C) for each misalignment scenario considered in Figure 3-11. Only first impacts are shown, while multi-turn impacts are neglected (53). 39

Figure 3-14: Measurements vs simulations of BLM signals in the LSS during the 2015 proton quench test comparing the ideal collimator settings vs a 400 μrad parallel jaw tilt of the primary collimator jaws. 41

Figure 3-15: Measurements vs simulations of BLM signals in the DS during the 2015 proton quench test. Simulation results of protons lost inside the SC magnets for misaligned (400 μrad tilt, red curve) and ideally aligned primary collimator jaws (blue curve). For the latter case, the figure also displays the contributions of upstream showers originating from outside the beam pipe (green curve) as well as their cumulative effect (black curve). 42

Figure 3-16: Tracking simulation energy loss map for the 2015 lead ion quench test (41). 44

Figure 3-17: (Top) Measurements vs simulations of BLM signals in the LSS during the 2015 $^{208}Pb^{82+}$ ions quench test. (Bottom) Equivalent FLUKA geometry of the IR7 LSS of the LHC. 47

Figure 3-18: (Top) Measurements vs simulations of BLM signals in the DS during the 2015 $^{208}Pb^{82+}$ ions quench test. (Bottom) Equivalent FLUKA geometry of the IR7 long straight section of the LHC..... 49

Figure 4-1: 2015 cumulative BLM signals for injection (450 GeV) and top energy (6.5 TeV). 54

Figure 4-2: Cost function plot, evaluating losses for top energy (6.5 TeV) protons in Beam 2. The losses mentioned in the legend are the ones that bear the minimum fitting cost for each year. 57

Figure 4-3: Comparison of simulated and measured BLM patterns (2015-2018) for Beam 2 proton losses at top energy (6.5 TeV). The measurements were divided by the number of protons lost in each year, determined in the previous figure. 58

Figure 4-4: Comparison of simulated and measured BLM patterns (2015-2018) for Beam 1 proton losses at top energy (6.5 TeV). The simulated pattern includes the crosstalk from beam 2 for the BLMs between -120m to -100m. The measurements were divided by the number of protons lost in each year, determined in the Figure 4-5. 59

Figure 4-5: Cost function plot, evaluating losses of top energy (6.5 TeV) protons from Beam 1. The losses mentioned in the legend are the ones that bear the minimum fitting cost for each year. 60

Figure 4-6: Comparison of simulated and measured BLM patterns (2015-2018) for Beam 2 proton losses at injection energy (450 GeV). The measurements were divided by the number of protons lost in each year, determined in Figure 4-7. 62

Figure 4-7: Cost function plot, evaluating losses for injection energy (450 GeV) protons in Beam 2. The losses mentioned in the legend are the ones that bear the minimum fitting cost for each year. 63

Figure 4-8: Cost function plot, evaluating losses for injection energy (450 GeV) protons in Beam 1. The losses mentioned in the legend are the ones that bear the minimum fitting cost for each year. 64

Figure 4-8: Comparison of simulated and measured BLM patterns (2015-2018) for Beam 1 proton losses at injection energy (450 GeV). The measurements were divided by the number of protons lost in each year, determined in Figure 4-8. 64

Figure 4-10: Picture of the return coil of a separation dipole (MBW) in IR7 with the RPL holder (encircled) (top), and the equivalent FLUKA geometry with the dose measured in one cubic centimetre in air (bottom). 66

Figure 4-11: Comparison of RPL measurements and FLUKA simulated dose in air for the years 2015-2017 (left axis). Line thickness represents a 15% statistical and experimental error. Bar graph shows the % contributed from injection losses to total dose from simulations (right axis). 67

Figure 4-12: The LHC machine cycle, illustrated by the beam energy and beam intensities. There are seven stages: 1) injection; 2) ramp; 3) flat top; 4) squeeze; 5) stable beams; 6) beam dump; 7) ramp down (64). 73

Figure 5-1: Energy sharing between IR7 beam 2 collimators during a horizontal loss scenario of beam 2, 6.5 TeV protons, with the 2015 collimation quench test settings. 83

Figure 5-2: Tertiary collimator FLUKA model (left) and superimposed with an absorbed dose map (right) for an asynchronous beam dump scenario (75). 84

Figure 5-3: Photograph and FLUKA model of the primary collimator assembly (jaws and tank) with the relevant dimensional quantities illustrated. 86

Figure 5-4: (Top) Peak power density over the length of the TCP.C6 for 7 TeV protons under a total power load of 500 kW, corresponding to 0.2h beam lifetime (BLT). (Bottom) Transversal peak power density profiles in the cleaning plane at selected longitudinal locations. 87

Figure 5-5: Peak power density over the length of the TCP.C6 induced by the inelastic interaction products of 7 TeV protons under a total power load of 500 kW corresponding to 0.2h BLT 88

Figure 5-6: Longitudinal peak power density distribution over the primary collimator length for 7 TeV protons under a total power load of 500 kW corresponding to 0.2h BLT. 90

Figure 5-7: Different secondary collimator jaw tapering designs considered for the HL-LHC (77). 92

Figure 5-8: Peak power density profiles over the active TCSG blocks in AC150GPH (left) and MoGR (right) for 7 TeV, 1h BLT, 2 sigma retraction. 93

Figure 5-9: Transverse (x, y) cross-section at +50 cm in the Z direction of the energy deposition map on the TCSG.A6R7 with MoGR absorber blocks, 7 TeV protons and HL-LHC settings. 94

Figure 5-10: Temperature map (left) and total directional deformation (right) of the TCSPM in MoGR 7 TeV protons, 0.2 h BLT (940 kW total power), HL-LHC settings (78)) 95

Figure 5-11: (top) 3D power deposition map on the most impacted TCSPM jaw with a Molybdenum coating. 7 TeV protons, 0.2 h BLT (500 kW total power), LHC

settings. (bottom) 1D peak power density over the jaw length, same collimator and settings. 97

Figure 5-12: Longitudinal profile of DPA in the TCP.C jaw (AC150GPH) predicted for Np_{7TeV} =10^{17} lost protons. The contribution from the different particles is disentangled. 100

Figure 5-13: Longitudinal profile of DPA in the TCP.C jaw (AC150GPH) predicted for Np_{7TeV} =10^{17} lost protons. The contribution from the different particles is disentangled. DPA is scored only after the first inelastic interactions of the impacting protons. 101

Figure 5-14: Longitudinal profile of total DPA in TCP.C (Hor) and TCP.B (Skew) jaws (AC150GPH and MoGR) predicted for Np_{7TeV} =10^{17} lost protons with fine (5x5 μm^2) and coarse (400x400 μm^2) scoring meshes. 103

Figure 5-15: Longitudinal profile of DPA in the TCSG.A6 (AC150GPH) predicted for Np_{7TeV} = 10^{17} lost protons in the CS. The contribution from different secondary products is also shown. 105

Figure 5-16: Longitudinal profile of total DPA in the active jaw of the TCSG.A6 in AC150GPH and MoGR and in its foreseen Mo coating for Np_{7TeV} = 10^{17}. 106

Figure 6-1: IR7 layout of the warm magnets relative to Beam 2 collimators (not to scale) 111

Figure 6-2:MQW spacer resin degradation due to cumulative dose (86) 112

Figure 6-3: FLUKA geometry visualisation of IR7 (right) with notable magnetic elements. Zoom of the MQW (top left) and MBW (bottom right) FLUKA models with their radiation shielding. 113

Figure 6-4: Picture of MBW.B6R7 followed by the MBW.A6R7 of the LHC. The tungsten radiation shield is also visible in front of the magnet return coils in the inner Beam 2. 114

Figure 6-5: Cumulative dose map projected on the MBW return coils for Np=10^{17}. Beam 2 enters the picture in the left beam pipe. 115

Figure 6-6: Longitudinal peak dose profile for Np=10^{17} in the MBW.B5 front return coil. The dose in the upper and lower coils is shown in green and red, respectively. The two upper curves are for the case without shielding while the two lower curves are with shielding. 115

Figure 6-7: Picture of MQW.E5R7 of the LHC with the rest of the cell 5 quadrupoles following. The tungsten radiation shield is also visible in front of the magnet return coils in the inner beam 2. 116

Figure 6-8: FLUKA dose scoring and other quantities of interest of an accidental beam impact in MQWH.E5R7 117

Figure 6-9: Total energy deposited to the various geometrical elements of the MQW.E5R7. Beam 2 enters the left beam pipe. 118

Figure 6-10: Dose map projected on the MQW (right) and a zoom of the most impacted coil and spacer (left) for Np=10^{17}. Beam 2 enters the picture on the left beam pipe. 119

Figure 6-11: Peak dose profile for Np=10^{17} in the MQW.E5 middle centre coil. 119

Figure 6-12: The LHC superconducting bending dipole (left) and quadrupole (right) magnets (89) 121

Figure 6-13: (Right) The NbTi Rutherford superconducting cables used at the LHC (90). (Left) The MB coil cross section (91) 121

Figure 6-14: LHC interconnect picture (right) and FLUKA model (left)..... 122

Figure 6-15: Peak power density profile in the SC coils of DS magnets for 585 kW proton losses in the collimation system. The beam direction is from the right to the left. 123

Figure 6-16: Power density cylindrical scoring on the MB.A9L7 FLUKA model (right) and a zoom in the most impacted longitudinal point as seen in Figure 6-15 for 585 kW total losses. Beam 2 enters the picture on the left. 124

Figure 6-17: Peak power density profile in the SC coils for 585 kW proton losses in the collimation system for perfect machine and with 400 μrad jaw misalignment. 125

Figure 6-18: Peak power density profile in the SC coils for 15 kW of ion losses during the 2015 ion quench test vs the 585 kW proton losses in the proton quench test. .. 126

List of Tables

Table 2-1: Run 2 collimator settings at top energy protons for each collimator family in IR7 (22-24). All settings are expressed in units of σ for the nominal β-function (25) and an emittance of ϵ_n=3.5 μm. 11

Table 3-1: Tracking simulation settings for the 2015 proton quench test, ideal machine. 27

Table 4-1 – Sample of the cumulative BLM signals according to beam modes for the year 2015 53

Table 4-2: Loss evaluation overview for Top Energy protons (6.5 TeV) and integrated luminosity for ATLAS and CMS 70

Table 4-3: Top energy (6.5 TeV) losses scaling according to the average integrated luminosity of ATLAS and CMS..... 71

Table 4-4: Loss evaluation overview for injection energy protons (450 GeV) and integrated luminosity for ATLAS and CMS 71

Table 4-5: Injection energy (450 GeV) losses scaling according to the average integrated luminosity of ATLAS and CMS 72

Table 4-6: **450 GeV (injection) collimation loss** estimates, integrated intensity measurements and scaling factors for Beam 1 and Beam 2 in the years 2015 – 2018. 74

Table 4-7: **6.5 TeV collimation loss** estimates, integrated intensity measurements and scaling factors for Beam 1 and Beam 2 in the years 2015 – 2018 75

Table 4-8: Estimated # of betatron proton losses for the full HL-LHC (12 years) lifetime. The most conservative scaling factors from section 4.3 were used. A safety factor of 3 is applied on top of the scaling factors..... 78

Table 5-1: Sharing of beam energy deposition in IR7. Missing energy has been converted to mass or carried away by neutrinos..... 82

Table 5-2: Total energy deposition loads on the new secondary collimator designs of TCSP and TCSPM at the TCSG.A6 positions of IR7 for current LHC and future HL-LHC upgrade scenarios (Last row) Total sagitta of the directional deformation (thermal + self-weight + tolerances) (72) 96

Table 5-3: Total DPA for the most impacted primary and secondary collimators for the HL-LHC. Results are shown for the presently used CfC grade (if it would be kept throughout the HL-LHC era) and for the MoGR compound. 108

Table 6-1: Maximum cumulative dose at the end of the HL-LHC era (Np_{7TeV} = 3 x 10^{17}protons lost) in the coil and the coil spacers of warm magnets in IR7, with and without the tungsten (W) shielding. 128

Table 6-2: Overview of the estimated power density achieved during Run 2 quench tests with 6.5 TeV protons and 6.37 Z TeV lead ions. 129

Chapter 1 Introduction

As of 2020, CERN is home to the most powerful collider in the world. Its mission is to expand the frontiers of human understanding of the universe through fundamental physics research. Powerful superconducting magnets are utilised in order to transport highly energetic particles. The Large Hadron Collider (LHC) (1) currently holds many world records such as that of the largest machine in the world. In the experimental physics category, it holds the energy record of 6.5 TeV per proton accelerated and the centre of mass collision energy records of 13 TeV for protons and almost 1 PeV for ions (2). In addition, it holds the intensity and luminosity records as well as total stored energy circulating in the accelerator (3). The construction of the LHC is a project that is surpassing 15 years of world class collaboration between numerous scientific disciplines including physicists, engineers, computer scientists and others.

A sophisticated collimation system is needed in order to safeguard against the high intensities and energy stored in the accelerator and ensure the unobstructed operation of the machine. The collimation system installed in the LHC plays a vital role in the prevention of magnet quenches from regular beam diffusion, the detection of abnormal beam losses with subsequent beam aborts, radiation protection and passive protection of the SC magnets in failure scenarios. The operational conditions will become more challenging after the High Luminosity-LHC (HL-LHC) (4) upgrade, when the stored beam energy increases to almost 700 MJ, while entirely new collimation concepts might be necessary for future colliders like the FCC-hh (5), which are planned to operate with multi-GJ beams. However, despite its remarkable performance, the current technology comes with limitations and performance constraints when looking at the future HL-LHC and beyond.

This thesis aims to establish and benchmark a simulation chain capable of handling all aspects of the radiation impact of the collimation beam losses on the LHC. This framework is then utilised to study the radiation impact toll that befalls on the magnets and collimators in the betatron cleaning collimation region of the LHC. To this end, an extensive development and advanced utilisation of sophisticated tools for particle tracking in vacuum and their interaction with matter was performed.

The first ever large scale comparison of simulated and measured beam loss monitor signals is analysed, and the performance of the simulation chain and their individual tools is presented in Chapter 3. A detailed analysis of the particle leakage allowed for the justification of discrepancies and the effect of machine imperfections.

A detailed analysis of the Run 2 operational period of the LHC (between the years 2015 and 2018), determining the total proton losses in the collimation system for the different years, is presented in Chapter 4. Additionally, a first ever benchmark of such a calculation against passive dosimeter measurements and simulations for the LHC is shown. In order to allow for future predictions of beam losses and their impact, two loss scaling methods based on measurable and predictable quantities are studied in the same chapter.

These results allowed for the evaluation of short and long term effects of radiation on the collimation system and its surroundings. Chapter 5 addresses the robustness and performance aspect related with the analysis and development of the collimation system. Present and future collimator material performance under radiation induced stresses are presented. Moreover, their long-term displacement damage in their crystalline lattice is assessed to provide reference for external material irradiation studies.

Lastly, in Chapter 6 the lifetime estimation of the normal-conducting magnets in the vicinity of the collimators are presented along with the effectiveness of radiation shielding designs. The permitted radiation levels on the super-conducting magnets (quench levels) are also evaluated in close correlation to the collimation system settings and performance for both ions and protons.

Chapter 2 High energy accelerator collimation

In this chapter, a short introduction to the Large Hadron Collider (LHC) and its model high energy collimation system is presented as well as the tools that are utilised for its development and performance optimisation studies.

2.1 The Large Hadron Collider

The LHC comprises two counter rotating particle beams bent by high field superconducting magnets (8.3 T) forming a 27 km synchrotron. In a sense, the LHC is made from two semi-autonomous particle accelerators, each as powerful as the other, bringing particles into collision in four predetermined locations where large detectors are placed to study the collision products.

Layout

The LHC layout is shown in Figure 2-1. The LHC comprises eight Insertion Regions (IR) four of which house the main detectors for the ATLAS (6), ALICE (7), CMS (8) and LHCb (9) experiments. The IRs contain the straight sections that apart from the experiments also house the operational infrastructure of the machine, such as the momentum cleaning in IR3, the radiofrequency cavities providing the acceleration in IR4, the beam dumps in IR6 and the betatron cleaning in IR7. Each IR contains an Interaction Point (IP) at its centre, inheriting the same numbering convention, even though there are only 4 beam crossings that allow for particle collisions to occur. The straight sections are about half a kilometre long with the rest of the machine connected by the Dispersion Suppressor (DS) and ARC regions. The DS and ARC regions are

filled with a periodic assembly of superconducting dipole (MBs) and quadrupole (MQs) magnets that provide the bending and focusing forces necessary for the beam transport around the ring.

Beam 1 (B1) circulates in clockwise direction (blue colour in Figure 2-1) and Beam 2 (B2) circulates in counter-clockwise direction (green colour in Figure 2-1). The position of each element in the LHC is usually associated with either its distance from IP1 in clockwise direction or the distance from its respective IP, becoming negative on the counter-clockwise direction.

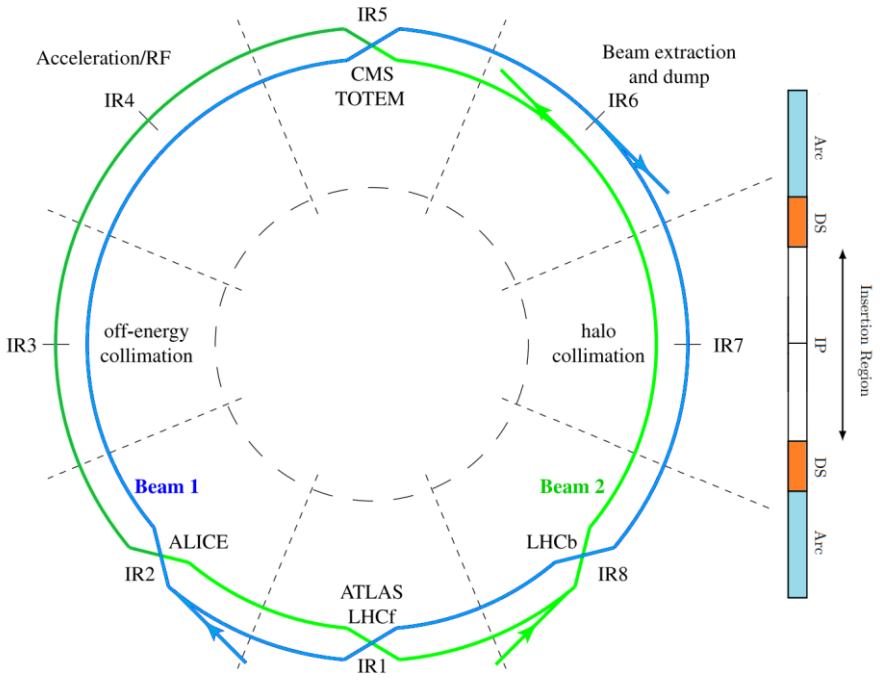

Figure 2-1: LHC layout and insertion region description (1)

Each machine element is assigned a distinctive identifier name. This name contains a cell number, corresponding to the number of quadrupoles located between the elements and the closest IP (apart from some exceptions). In IR3 and IR7 there are also less powerful normal conducting magnets. In order to produce the same focusing effect as a superconducting one they are split into multiple modules notated by a letter before the cell number. For example, the name MQW.E5R7 denotes the module 5 (E)

of the MQW type normal conducting quadrupole in cell 5 right (R) of IP7. Most of the elements are common between the two beams but some (e.g. corrector magnets, collimators, etc.) are assigned to each beam and are given a .B1 or .B2 additional notation.

Superconducting magnets

The main dipole magnets (Main Bends, MBs), occupy around 2/3 of the 27 km ring while the remaining length is mostly dedicated to beam focusing (Main Quadrupoles, MQs) including around 6000 corrector magnets. In total 1232 MBs (1104 in the arc and 128 in the DS sections) 15 meters in length and 392 MQs (360 in the arc and 32 in the DS) 3 meters in length are installed (10).

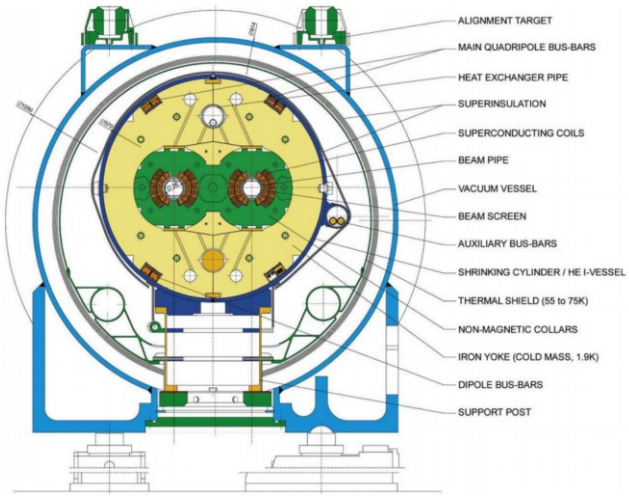

Figure 2-2: Cross section of an MB magnet of the LHC (10).

A cross section of the MB magnet is shown in Figure 2-2. The MBs are designed to deliver a magnetic field of up to 8.3 T inside the beam pipe. They provide a bending radius of 2804 m, for a maximum particle energy of 7 Z TeV. Their superconducting coils are made out of NbTi cables which are cooled down to a temperature of 1.9 K using liquid helium.

There are multiple kinds of quadrupoles installed in the LHC. The majority of them are identical to each other and are called MQs and are essential for the beam transport around the ring. They can achieve a field gradient of up to 223 T/m and their

superconducting coils are similar to and operate at the same conditions as the ones of MBs. This thesis will be focused on these most abundant quadrupoles. However, four more types of superconducting quadrupoles exist in the IRs the details of which can be found here (1).

Beam Loss Monitors

The main Beam Loss Monitors (BLMs) used in the LHC are ionisation chambers (11,12). There are more than 4000 BLMs installed around the LHC tunnel. Each BLMs is able to detect beam losses and, when the level of radiation exceeds certain thresholds, trigger the dump of the beams. BLMs are either attached on the SC magnets or installed in special BLM holders on other equipment such as collimators (Figure 2-3). The BLM chambers are filled with N_2 gas slightly pressurised at 1.1 bar. Their size is about half a meter in length with a sensitive volume of around 1.5 x 10^{-3} m^3 that makes it suitable for covering large scale accelerators such as the LHC.

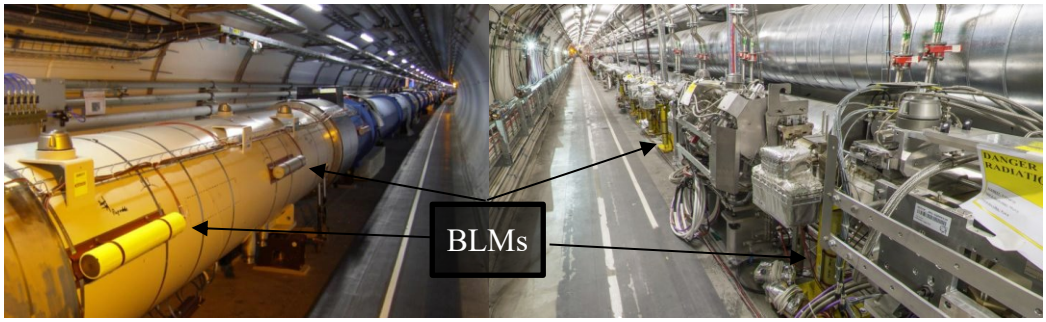

Figure 2-3: BLMs attached to the SC magnets (left) and to the primary collimators (right)(13).

Even though BLMs do not measure directly the physical quantities of interest (Section 2.3.2) they provide one of the few experimental measurements suitable for benchmarking the radiation simulation studies.

2.2 The collimation system of the LHC

The LHC is designed to store a record breaking maximum energy of 362 MJ per beam of protons. This is equivalent to the energy released by 78 kg of TNT explosive material. Uncontrolled beam losses may lead to equipment failures and catastrophic

damage to the machine elements. However, even a very small portion of the stored energy can lead to an increase of the temperature of the SC coils above their operating ones, causing them to quench. Nonetheless, no matter how well the beam is controlled by the magnetic elements, some losses would inevitably be present on the aperture of the SC magnets.

Beam lifetime and particle loss rate

For regular loss scenarios (i.e. not accidental), the collimation system is designed to cope with a maximum expected beam loss rate which is determined by the beam lifetime (τ_b) (14). In most cases the circulating beam intensity, $I(t) = I_0 e^{-t/\tau_b}$, is modelled by an exponential decay function with the beam lifetime defined by the time constant $\tau_b \equiv \tau_b(t)$ and I_0 as the initial beam current. In a linear approximation of the maximum loss rate at the start of the decay the beam loss rate can be calculated as:

$$\frac{dI}{dt} \cong \frac{I_0}{\tau_b} \tag{2.1}$$

This formula is used to calculate the particle loss rate in the collimation system for high beam lifetimes that can only be sustained for a few seconds.

Collimator types

A multi-stage collimation system (15,16) is installed in the LHC in order to safely and purposely clean this inevitable beam losses. It consists of 100 collimators that are strategically located around the ring in order to ensure an unobstructed operation of the SC magnets. Figure 2-4 shows, on the left, a picture of an assembled collimator jaw comprised of an absorber block made of graphite (CFC) the cooling pipes filled with water and the tapering. Two facing jaws inside a vacuum tank with a gap in between form the assembly of a collimator (Figure 2-4 right). The majority of the beam particles are able to move freely between the collimator jaws with only a small fraction (usually larger than 5 sigmas assuming a Gaussian populated beam) of the halo particles being intercepted by the absorber blocks.

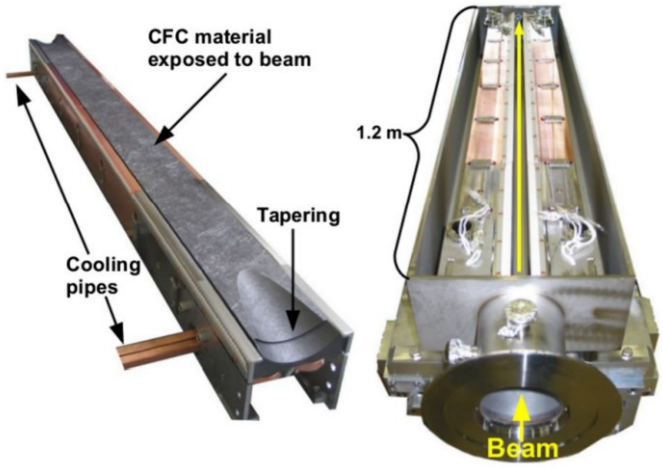

Figure 2-4: Individual collimator jaw (left) and collimator assembly (right) with two jaws inside a collimator tank. An opening that the beam passes through exists between the two jaws (17).

The collimation system also doubles as a passive protection system against accidental scenarios. Being the limiting aperture of the machine, collimators are the first devices to intercept particles with large amplitudes and therefore protect against high energy losses on other machine elements. Accidental high-power deposition in the collimator jaws can cause anything from temporary or permanent jaw deformation to the destruction of the collimator. These cases, however, are very unlikely and are not studied in detail in the context of this thesis.

Figure 2-5 illustrates the multi-stage design of the collimation system which is based upon the principle of high energy particle scattering to larger amplitudes after their first interaction at the primary collimators (Target Collimator Primary, TCP). Most of the halo protons will eventually inelastically interact in the primary collimator and develop further hadronic and electromagnetic showers inside and outside of the collimator. Nevertheless, a significant percentage of particles survive and will get a kick in the phase space pushing them to a larger physical aperture. The ones that do not a get a large enough kick to be lost in the beam aperture are intercepted by the secondary graphite collimators (Target Collimator Secondary Graphite, TCSG). The hierarchy principle dictates that the relative aperture between the TCP and TCSG is

such that halo particles will never intercept the secondary collimators without first interacting with the primary.

Further downstream, localised active absorbers (Target Collimator Long Absorber, TCLA) are installed that are placed in close proximity to the superconducting magnets and mainly protect against the hadronic and electromagnetic showers generated upstream. The TCLAs, together with the tertiary collimators mentioned below, are also the last line of defence against the small fraction of highly energetic protons that can escape both the primary and secondary.

Lastly, a tiny percentage of particles with just the right magnetic rigidity and phase space amplitude can manage to escape all three different kinds of collimators. These particles will either be able to circulate around the machine or be lost in the high betatron and dispersive regions (i.e. DS) of the machine. During the LHC physics operation with squeezed beams, the superconducting triplet magnets introduce extreme betatron values (18) while focusing the beams at the IPs. To guard these magnets against losses, tertiary collimators (Target Collimator Tertiary, TCT) are placed upstream of the triplet magnets in the same insertion region.

There are other types of collimators as well such as the TCLI (Target Collimator Long Injection Protection) but in this study we will focus on the main ones mentioned above which are located in the betatron cleaning insertions IR7.

The performance of the collimation system is quantified by the collimation efficiency, representing the fraction of halo particles extracted by the collimators over the total population that is lost from the beam due to its interaction with the collimators. For example, a perfect collimation system would have a 100% cleaning efficiency, fully protecting the SC magnets from beam losses.

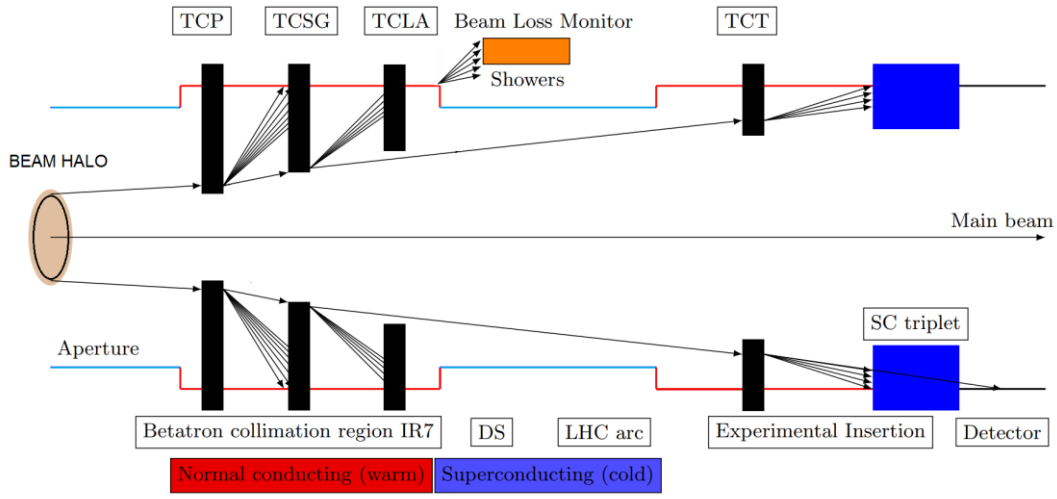

Figure 2-5: Schematic representation of the LHC collimation system (19,20).

Collimator settings

The collimator jaw positions can be individually adjusted but so far, they are adjusted according to the collimator family they belong (e.g. TCP, TCSG, TCLA etc.). The distance between the two jaws is, by convention, described as the half gap in units of the normalized RMS beam size σ. These settings vary each year and a summary for the three main families in IR7 is presented in Table 2-1.

The geometric emittance is reduced when the beam energy increases due to adiabatic damping. This is taken into account by assigning constant collimator settings according to the normalised emittance. The physical half-gap in mm units changes synchronously during the ramp of the beam following the reducing physical beam size.

The settings, while they are adjusted given the operational experience from each year, should follow certain principles. For example, the settings must make sure that the collimation hierarchy is assured even when orbit drifts appear in the machine (21) in order to minimise the risk of damaging the machine hardware. Furthermore, the collimator jaws induce impedance that is able to distort the individual particle tune, therefore restricting the collimator design and material choices.

Table 2-1: Run 2 collimator settings at top energy protons for each collimator family in IR7 (22-24). All settings are expressed in units of σ for the nominal β-function (25) and an emittance of ϵ_n=3.5 μm.

Year	*TCP*	*TCSG*	*TCLA*
2015	5.5	8	14
2016	5.5	7.5	11
2017	5-5.5	6.5-7	10-10.5
2018	5	6.5	10

2.3 Simulation tools and method

In this section a general overview of the software used for the study of the radiation impact of collimation losses is presented. A more detailed look specific to each study is given as introduction in each chapter.

2.3.1 Software tools

The simulations tools described in this chapter have played a vital role in optimizing the LHC performance in first two physics runs. Many aspects of their development have been driven by the needs of the LHC but are now widely used in many different applications outside the fundamental research. A short description of the key features of the main tools that were used in the duration of the thesis is given in this section.

A short description of the capabilities of the main scientific software used in this study is presented in this chapter. The study required a combination of analytical beam tracking and Monte-Carlo based software.

MAD-X

MAD X (Methodical Accelerator Design) [MAD] (26,27) is a tool developed with the aim to play the protagonist role in the world in the field of particle accelerator design and simulation. It stands as the main tool used at CERN and beyond for the simulation of beam dynamics and the computation of beam optics in particle accelerators. The

accelerator components and their strengths (i.e. magnetic field) are provided as input by the user. The code offers a matching function with the ability adjust specific accelerator related variables in order to fulfil certain desirable constrains. It includes a special function with the ability to produce the necessary beam optics required as further input for SixTrack.

Sixtrack

For studies dedicated to beam cleaning with a collimation system the use of the SixTrack is employed (28). It is capable of tracking particles transported through a lattice, element by element calculating their new six-dimensional phase space coordinates. The code is also able to handle basic collimator absorber blocks utilising embedded scattering model (i.e. COLLTRACK/K2 (29,30)) routines. Combined with a detail aperture description of the accelerator the code is capable of producing particle lossmaps starting from the interaction of the beam halo with the primary collimators. These capabilities make Sixtrack a powerful tool to study the effectiveness of the collimation settings for various different optics settings taking into account multi-turn effects such as the betatron motion of the particles in an accelerator.

FLUKA

FLUKA (FLuktuierende KAskade) (31,32), is a general purpose Monte Carlo code widely used for energy deposition and radiation damage calculations (e.g. machine protection, design of dumps and absorbers, radiation to electronics, activation, collimation etc.). In the context of the thesis it is the main tool employed to study the physical processes of beam particles interacting with matter.

In particular the code is able to handle the all of the main processes involved in the interaction of high energy particles in the LHC (i.e. protons and ions). It is able to compute the initial interactions (e.g. the ionisation, coulomb scattering, nuclear elastic and inelastic interactions) with the matter (i.e. collimators). Furthermore, is has the ability to track the hadronic and electromagnetic cascades following the initial inelastic interactions of the primary beam particles.

Lastly, the immense capabilities of FLuka's grAphical user InteRface (FLAIR) (33) was extensively utilised in all aspects of the studies: input preparation, geometry error debugging, 3d geometry plots, scoring maps overlaid in the geometry etc.

Sixtrack-FLUKA coupling

The Sixtrack-FLUKA active coupling (34,35) code expands on the Sixtrack capabilities by adding the ability to track both protons and heavy ions (36). It allows for tracking of the particles in an accelerator and their interaction with the collimators utilising the specialised particle interaction models of FLUKA. In the case of ions, secondary ion fragments with the right magnetic rigidity to be further tracked in the accelerator are also tracked. In addition, instead of rectangular blocks, the collimators can be described in detail using the more powerful geometrical description capabilities of FLUKA.

LineBuilder and the FLUKA Element DataBase

LineBuilder (LB) (37) is a tool developed at CERN that is used for the creation of sophisticated FLUKA geometries of accelerator beam lines. Each machine element (e.g. magnets, collimators, beam loss monitors, etc.) is modelled separately in detail and is placed in a specially arranged directory called the FLUKA Element DataBase (FEDB) (37). The code receives as input the machine optics as generated from MAD-X, the correspondence between the optical elements and their geometrical descriptions in FLUKA that are stored in the FEDB and specific directives from the user. It is extremely customisable and is able to create a final working FLUKA input including all required information e.g. (magnetic field cards, scoring detectors, collimator settings, out of beam elements such as beam loss monitors, etc.).

The FLUKA geometry models located in the FEDB that were utilised in the context of this theses are the culmination of years of work by the EN-STI-BMI (former EN-STI-EET) section at CERN. The majority of the models were edited, validated for errors and further developed while new models (such as the collimator supports, new collimator jaw designs, etc) were modelled from scratch.

The usage of these tools was vital for the handling of all aspects of the FLUKA simulations, extremely facilitating the studying of different collimation cases. It ensured the full synchronisation of the final FLUKA input file with the various machine optics taking into consideration the beam characteristics (e.g. beam energy, particle type, collimation settings, etc.). Apart from the magnetic field strength calculations for both dipoles and quadrupoles the code was responsible for the precise placement of the elements in the FLUKA reference system.

2.3.2 Physical quantities

The three main physical quantities that this study focusses are the prompt radiation related quantities, energy deposition, dose and DPA. A small description of the physical quantities under study is given with an emphasis in the simulation chain adopted that utilised all of the above mentioned tools.

Energy deposition

In the context of a given beam loss rate the energy deposition is provided in the form of power density with units of W/cm^3. The majority of the energy deposition comes from the process of ionisation. Charged particles traversing inside matter lose energy through Coulomb interactions with the atomic electrons of the medium. If this energy is high enough the electrons are ejected, ionising the material. The process continues until all energy is converted to kinetic energy of the electrons also known as energy deposition. The magnitude and effect of this quantity depends on the loss locations. For example, in the SC coils the power density is in the order of mW/cm^3 while in the collimators in the order of kW/cm^3. This is due to the different effects that the elements are sensitive to, like temperature increase of a few degrees over a few seconds, to thermal shock inducing temperature increasing events respectively.

Dose

Dose is derivative of energy deposition and is expressed in Gy. This quantity is directly measured as dose rate in Gy/s by the BLMs installed in the LHC and is calculated in this study as a form of simulation benchmarking. Furthermore, many studies have shown a direct link between the cumulative long term dose to machine components

and their operational lifetime. Specifically, different parts become prone to failures in various levels of dose ranging between kGy and MGy. In this study we will focus in the dose cumulated into the coil insulations that are made out of organic materials such as plastics. These materials tend to age at the molecular level. This process is sped up in the presence of a radiation environment becoming brittle and forming cracks that eventually can lead to short circuits in the coils. As a form of additional benchmarking of the long term losses the dose measured by dedicated passive dosimeters is calculated as well.

Displacement Per Atom

The displacement damage induced by particles in a material is proportional to the non-ionising energy loss along particle tracks and depends on the particle type, the particle energy and the damage threshold of the material. In a mixed radiation environment like the LHC betatron collimation region, a large variety of particles produced in hadronic and electromagnetic showers can contribute to the dislocation of atoms in collimators. The induced damage is typically quantified by Displacements per Atom (DPA), which provides a universal measure for assessing point defects by different particles and processes.

DPA represents the defects, that develop in crystalline lattices (e.g. graphite) when neutral or charged particles and ions pass through them. Depending on the topology of the damage they can be categorised in 1 dimensional point defects (i.e. interstitials and vacancies), 2 dimensional line defects (i.e. dislocation lines) and 3 dimensional planar defects (i.e. dislocation loops) or volume defects (i.e. voids, bubbles, etc.). The cumulative effect of these can cause the material properties degradation or destruction.

2.3.3 Simulation chain

All of the physical quantities described are simulated using FLUKA. However, in order to properly describe the source term for the Monte Carlo studies the use of Sixtrack-FLUKA coupling is employed. The multi-turn tracking of the particles takes into consideration the effect that the beam optics have in the description of the initial interaction of the beam particles with the collimators.

The standard simulation chain involves a two-step method: The first step is always the creation of the particle impact distribution in the collimators using the Sixtrack-FLUKA coupling. For the second step, this distribution is then loaded in the FLUKA geometrical description of the relevant part of the machine (e.g. the IR7) and the relevant quantities are scored.

However, sometimes the levels of the relevant quantities (e.g. energy deposition in the SC coils) are orders of magnitude lower than the ones close to the source. This fact makes it computationally impossible to calculate unless advanced biasing techniques are utilised. In these cases, a third step is introduced to the chain. The second step is replaced by a computationally inexpensive FLUKA simulation that focuses in diverting computing power to the relevant processes and creating a secondary particle source term. For example, in the case of the SC magnets, only the nuclear elastic and elastic interactions are processed and a loss map in the aperture of the cold magnets is created. This FLUKA created loss map is then used as a source term for the now third step, the detailed FLUKA simulation similarly to the standard second step in order to extract the relevant physical quantities.

More detail information of the technical and physical challenges that the studies had to overcome are described as an introduction to the case by case scenario in the following chapters.

Chapter 3 Simulation benchmark for betatron collimation losses

This chapter presents the results of comparing the BLM signals using the tools and simulation method described in Chapter 2 against the collimation quench tests of 2015. It demonstrates the accuracy and performance of the simulation chain and offers insight into the nature of the collimation losses.

3.1 Introduction

The LHC betatron collimation system demonstrated an excellent performance in Run1 and Run 2. Particles leaking from the collimation insertion to the neighbouring dispersion suppressor nevertheless pose a risk for the future LHC performance as these particles might induce magnet quenches. To quantify this risk, controlled beam loss experiments were carried out at different beam energies in Run 1 and 2. In these tests, the loss rate of beam particles in the betatron cleaning insertion was deliberately enhanced by crossing third-order resonances or by exciting the beam with the transverse damper. While the beam energy was lower in the earlier quench tests in Run 1 (3.5 and 4 TeV) (38,39), higher energy tests close to the design energy could be carried out after LS1 using 6.5 TeV protons (40) and 6.37 Z TeV Pb ions (41).

The main goal of the simulation of the collimation quench tests of 2015 was the estimation of the peak power density that was induced in the superconducting coils that may have led to a superconducting magnet quench (42). However, there is no direct way of measuring the aforementioned quantity. Therefore, the only way of indirectly testing the accuracy of the simulation results inside the superconducting

magnet was by simultaneously simulating the dose that was measured by the beam loss monitors during the test and then compare it with the experimental values.

The study of this controlled collimation loss experiment is the first significant application of the tools that were developed for the simulation of beam losses in Point 7 and paves the way for a better understanding of the collimation losses. The collimation quench tests offered characteristics that made them excellent benchmark cases, such as a measurable particle loss rate, one specific beam loss type (i.e. horizontal collimator losses) and a high enough loss rate in order to acquire signals above noise level in the dispersion suppressor BLMs (43,44).

While the main focus of the quench test simulations was to determine the power density in superconducting magnets, the tests also provided excellent conditions for benchmarking the energy deposition in the collimation insertion itself. Taking advantage of the detailed description in FLUKA of both the warm section and cold sections (bottoms of Figure 3-7 and Figure 3-9 respectively), it became possible to simulate the entirety of the BLMs located in Point 7.

3.2 Collimation quench tests 2015

The LHC superconducting magnet's operating temperature is 1.9 K allowing for the superconducting (SC) properties to function. When highly energetic protons impact on the vacuum pipe inside the magnets, the induced showers can deposit enough energy in the magnet coils such that the temperature increase leads to a loss of the superconducting state, which is generally referred to as a magnet quench. In case of collimation losses, particles can leak from collimators to the dispersion suppressor (DS) next to the IR7 betatron cleaning area, where SC magnets are located. Such losses are continuously present throughout regular operation. Consequently, the maximum intensity that can be achieved in the LHC can be limited by collimation system performance.

The tests were part of the machine development campaign (MDs) at the end of the 2015 run and were organised and carried out by a collaboration of different people from the operation, collimation, machine protection and beam machine interaction teams. The relevant CERN notes with details of the tests are referenced in the following sections which provide some background information for the experimental situations simulated in each case.

3.2.1 Proton collimation quench test

The target of the proton collimation quench test was to achieve the HL-LHC design loss rate to the collimation system of 1000 kW proton losses and examine the behaviour of the SC magnets. The adopted strategy was to induce high losses while the collimation system was in place and observe whether any IR7 DS SC magnets would quench due to the leakage from the collimators. Slow losses of the order of 500 kW to 1 MW over few seconds were created by exciting the beam with the LHC Transverse Damper (ADT) (45).

During previous tests no magnet quenches were observed for values of up to 1 MW (40). However, these past tests were performed with lower beam energies of 3.5 TeV and 4 TeV and a corresponding lower magnet current. For a 6.5 TeV beam, higher magnetic currents are required and as a result, magnets have a lower margin with respect to quenches.

Figure 3-1, shows the proton intensity measured by the Beam Current Transformer (BCT) during the test (left) and the equivalent power loss from the beam (right) by converting the proton loss rate. Despite numerous technical issues in the adjustment of the BLM threshold settings to allow for the target losses, the 2015 quench test achieved peak losses of 585 kW by exciting Beam 2 in the horizontal plane with the ADT. There was an increasing excitation over 5 seconds, with the slope decreasing in the last second before the dump. An early dump was triggered by a BLM, and thus, no beam induced quench was recorded.

Along with the 2015 quench test in red for 6.5 TeV proton energy, the previous tests are also shown for comparison. Due to the quench margin of the SC magnets being much lower for 6.5 TeV combined with the lack of magnet quench in all cases, it is only possible to determine a lower power limit that the magnets can withstand before quenching for each energy.

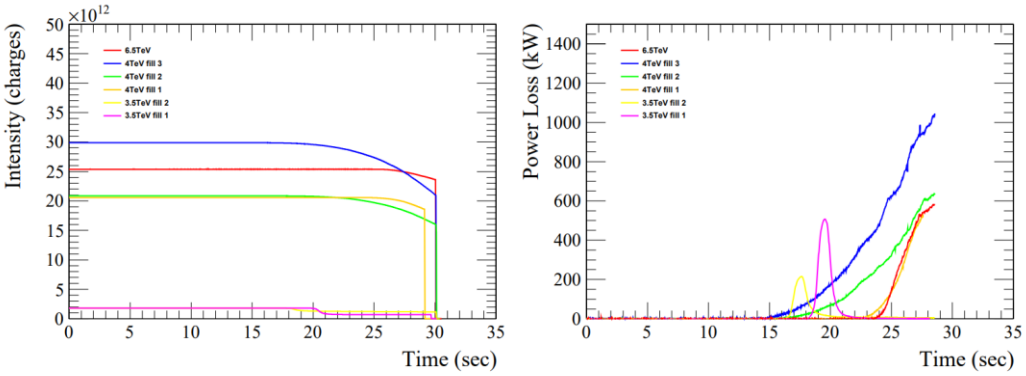

Figure 3-1: Left: Beam intensity during the proton quench tests in 2011-2015. Right: Power loss calculated from the BCT for the same years (40).

The BCT measurements, both the peak value of 585 kW as well as the cumulative number of protons lost during the test (QT_{p}) are substantial for our study;

$$QT_{\mathrm{p}} = 1.7655 \text{ x } 10^{12} \text{ p} \tag{3.1}$$

This number will be vital for the normalisation of the simulation results shown later in the chapter.

The other important measurements acquired during the quench test are the BLM signals levels during the test. Figure 3-2 shows the BLM signals measured at the time of the 585 kW peak power loss rate. Beam 2 primary collimators are located at 20200 m on the plot with the Beam 2 direction being from right to left. Each BLM is assigned a different colour according to the equipment it protects; blue for the BLMs located on SC magnets; red for the ones located on normal conducting magnets and other room-temperature equipment (except collimators); and black for the BLMs at the collimators. The distinction between Beam 1 (B1) and Beam 2 (B2) collimators

implies that the respective BLMs are in closer proximity to their corresponding beam. However, this distinction is mainly a functional assignment since, in reality, all BLMs are susceptible to showers originating from either beam and are useful in the study of the losses.

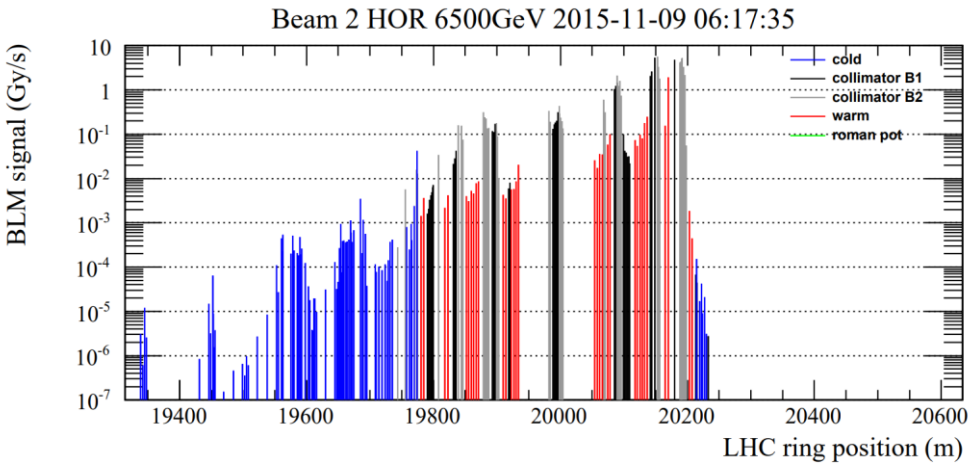

Figure 3-2: BLM signals measured at the moment of peak power loss of 585 kW during the 2015 proton quench test (40).

Lastly, the fact that there was a lack of quench during the test provides a lower limit of losses that the collimation system can handle with the specific loss pattern induced by the specific beam, optics and collimator settings. To be able to extrapolate to HL-LHC operating conditions, there is a need to evaluate another quantity, directly associated with the quench mechanism, that can be compared among different settings. That quantity is the power deposition density in the SC coils. Unfortunately, this is not a measurable quantity and can only be evaluated through simulations. This chapter will focus mainly on the simulation of the BLM signals and the comparison with the experimental data. Lastly, the results will be utilised as reference for the simulation of the power deposition in the SC coils that will be presented in Chapter 6.

3.2.2 Ion collimation quench test of 2015

In Chapter 3.2.1, it was explained that the primary goal of the quench test is to evaluate the quench limits of the SC magnets. In the case of the ion quench test, the secondary

purpose of assessing the collimation system efficiency, this time with ions, is much more important. The LHC heavy-ion run during 2015 with $^{208}Pb^{82+}$ ions surpassed the design value of the total stored beam energy of 3.81 MJ (1) reaching around 9.51 MJ. A further increase, up to 18.0 MJ is expected with the upcoming upgrade of the injector chain of the LHC (46).

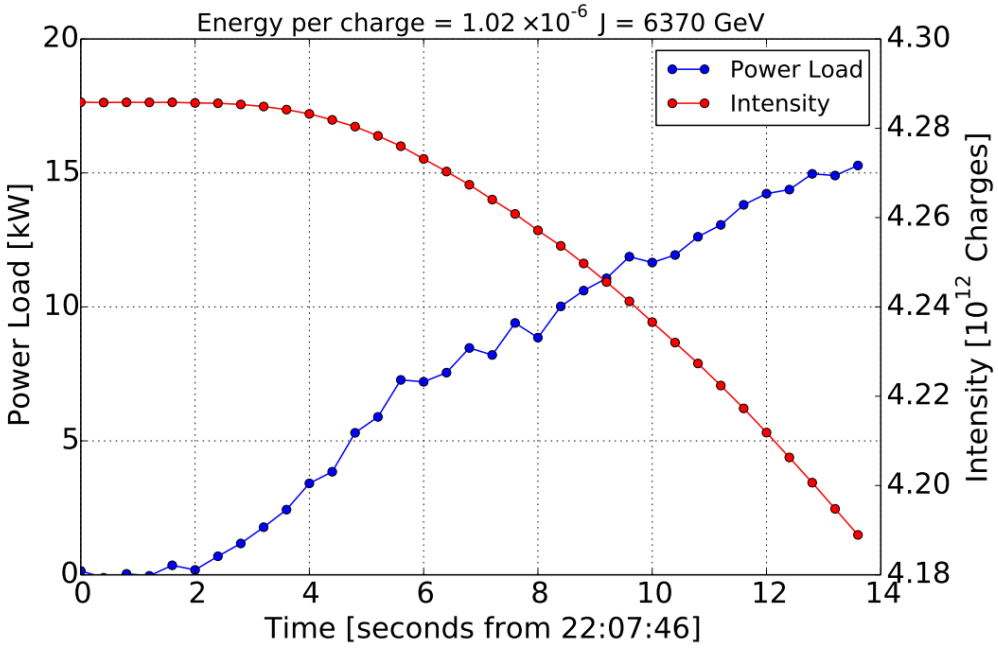

Figure 3-3: Intensity and power loss calculated from the BCT during the quench test (41).

The collimation system is designed for the optimal cleaning of protons, and thus its efficiency is much worse for ion cleaning. Since the same principle of unavoidable beam losses during the operational cycle still applies for ions, a given collimation cleaning efficiency implies an upper boundary for the maximum possible total stored beam energy which can be sustained during beam lifetime dips. The knowledge of the quench limit in terms of power deposition in the SC coils in combination with a good understanding of the efficiency allows for the evaluation of the intensity limitation and provides essential input for possible upgrade scenarios.

Similar to the proton quench test, the relevant measurable quantities are the number of ions lost and the BLM signals, in addition to which, if any, magnets are quenched.

Figure 3-3 shows the beam intensity evolution and the equivalent power loss for the Pb ion quench test in 2015, which was carried out with a beam energy of 6.37 Z TeV (using Beam 2 as for the proton quench test). The power lost on the collimation system was steadily rising over 12 seconds, reaching a maximum of 15 kW steady over 1.5 seconds. At that point, module B of the SC dipoles in cell 9 left of point 7 quenched, triggering a beam dump. One can immediately see that there is almost a factor of 40 worse collimator cleaning efficiency for ions compared to protons, where with a power of 585 kW there was still no quench.

On the same plot, the BCT charge count is shown, that while for protons automatically translates to number of protons, for ions it does not since there are 82 charges per $^{208}Pb^{82+}$ ion. The total number of ions lost during the fill was;

$$QT_{\mathrm{Pb}} = 1.1829 \times 10^{9}\ {}^{208}Pb^{82+} \tag{3.2}$$

Figure 3-4 shows the BLM signal pattern measured at the time of peak power loss rate of 15 kW. Beam 2 primary collimators are, as in the proton case, located at 20200 m position at the plot with the Beam 2 direction being from right to left. The same general notes apply as for Figure 3-2.

A noticeable exception to the pattern is the location of the maximum BLM signal, which is not at the primary collimators, but at secondary collimators downstream. This does not mean that the impact hierarchy is not respected but is due to the fragmentation of the heavy ions which transfer a lot of their energy into downstream collimators and producing higher BLM signals.

To get a better insight on what the BLM signals actually translate to when it comes to critical energy deposition values, one will have to go through the simulation procedure described in Chapter 2. This section will focus on the benchmarking of that simulation chain against the BLMs, both for ions and protons while the simulated values for the SC magnet coils are presented in Chapter 6.

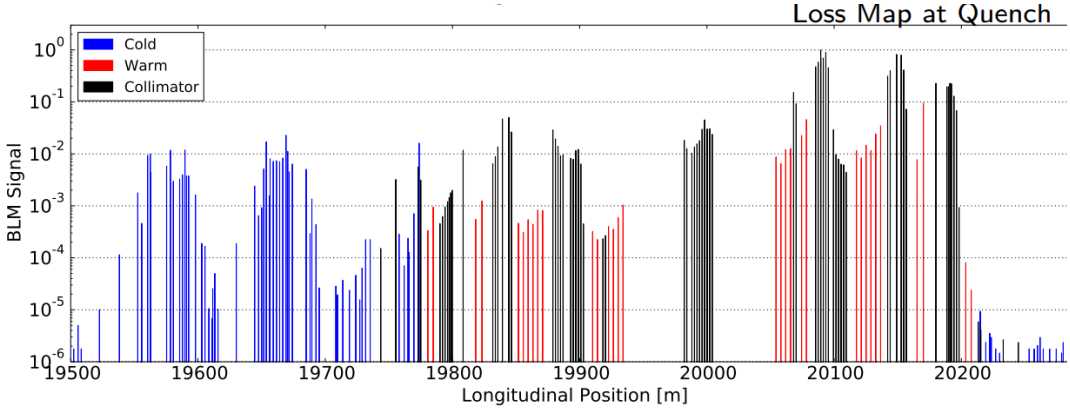

Figure 3-4: BLM signals measured at the moment of maximum power loss of 15 kW during the 2015 lead ion quench test. The signals are normalized with respect to the maximum signal (41)

3.3 Benchmark against the proton collimation quench test

Having established the experimental parameters of the tests and the experimental measurements required as input for the normalisation of the simulation results, this chapter aims in benchmarking the simulation chain that was described in Chapter 2. A more detail description of the simulation chain will be presented along with the significant challenges and uncertainties of each step. Finally, it will present the results of the benchmark against the BLM signals acquired during the collimation quench tests.

3.3.1 SixTrack-FLUKA coupling tracking simulations for protons

The first step of the simulation chain is the setup of the tracking simulations. These are performed with the use of the SixTrack-FLUKA coupling in order to track the protons around the LHC. Their impact positions in the collimators are referred to as “touches” to avoid confusion with the older method that scored the location of the proton inelastic interactions in the collimators. In this way is it possible to take into account multiple passages of protons through the collimators in the shower simulation. Interactions other than deep inelastic ones, can for example contribute to the energy

deposition or radiation damage in the collimators which wasn't taken into account in the older simulation method.

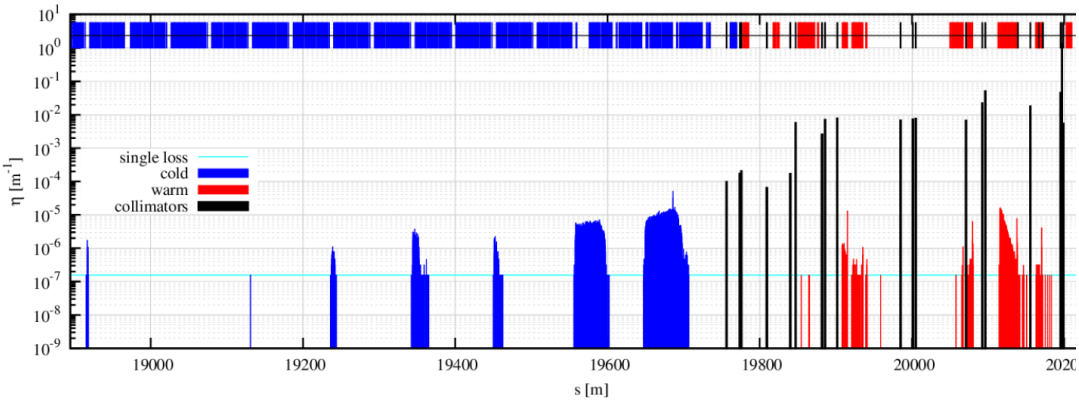

Figure 3-5: Tracking simulation proton loss map showing the location of protons impacting the beam pipe aperture or being lost in the collimators

When a proton undergoes an inelastic interaction that would either not create any secondary protons, or the ones that are created are below 30% of the original energy (e.g. 6.5 TeV), they are considered "lost" and are no longer tracked around the accelerator. The rest of the created secondaries are not followed at this stage, but the code can continue to track the high energy protons that due to their reduced energy and/or their phase space kick after an impact with the collimators are eventually lost in the aperture.

However, these losses are not directly used in the shower simulations since only the impacts on the collimators will be passed to the second more detailed step. Figure 3-5 shows a typical loss map created by the tracking simulations with the position of proton losses in IR7 for the case of the collimation quench test (47). However, this provides only qualitative information of loss locations and in order to be benchmarked a full particle shower simulation is required to compare the results against BLM measurements.

As described in Chapter 2, the tracking simulations require a set of external input parameters to describe the details of the simulations. These are the optics and lattice information, a collimator database containing their attributes (e.g. name, material,

length, aperture, orientation) and the initialisation parameters such as the number of protons and turns to run, their energy and initial distribution etc. While most of the settings are well known experimentally for the LHC, the initial distribution of halo particles impacting the collimators can, at the moment, not be measured directly.

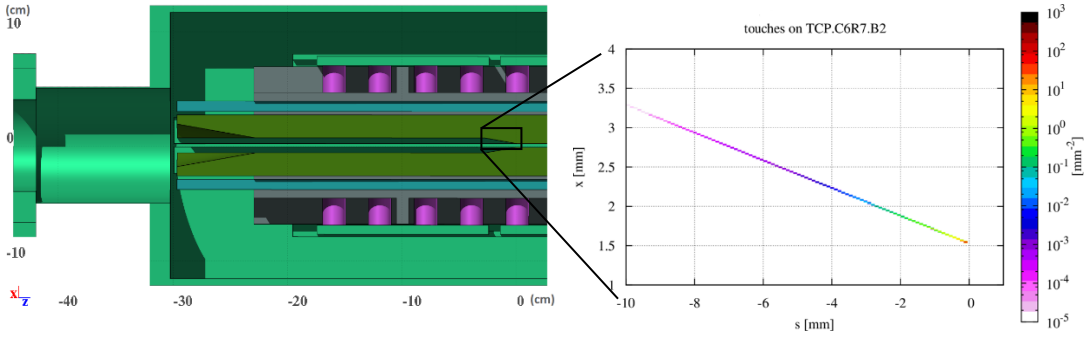

Figure 3-6: Primary horizontal collimator (TCP.C) FLUKA geometry (left) and proton impact positions "touches" (right). (s=z)

While it is expected that they approximately follow a Gaussian distribution in the non-cleaning plane, the impact parameter (which is the distance between collimator edge and impact location) depends on the halo diffusion and is estimated to be in the order of a few hundred nanometres (https://lhc-collimation-project.web.cern.ch/lhc-collimation-project/files/Chapter18b.pdf). Moreover, the position of impact in the primary collimator is assumed to be the front edge (longitudinally) of the primary collimators with an equal proton load on each jaw. Figure 3-6 shows a cross-section of the primary collimator jaws illustrating that the proton impact positions are heavily concentrated at the tip of the jaws. These assumptions present the most significant source of uncertainties at this stage of simulations, and it will be shown in the rest of this chapter that they mostly affect the number of losses in the DS but have a small effect on the warm section losses apart from the area close to the impact point (the primary collimators).

Table 3-1: Tracking simulation settings for the 2015 proton quench test, ideal machine.

IR7 collimator settings	**Optics**	**Initial distribution sampling**
TCP/TCSG/TCLA	Beam 2 injection optics	Beam sampling at IP1 in 6D
Half-gap (σ) 5.5/8.0/14	6.5 TeV	Horizontal plane: constant over [5.50σ:5.54σ]; Vertical plane: Gaussian distribution; Longitudinal plane: Gaussian distribution within 2σ
sigma at horizontal TCP in x: σ_{tcp} = 275,69 μm	no squeeze; bumps for parallel separation on	

Table 3-1 shows the parameters used for the tracking simulations of the 2015 proton quench test. The same collimation settings were used for the 2015 normal operational period, which means that the results of the simulations could be used to compare against the normal operation, since optics changes at the interaction points do not affect the loss pattern in Point 7. To save computational time, the horizontal plane was sampled uniformly over 0.04 σ from the primary collimator edge, which is of the order of 10 μm. This requires fewer turns for the protons to get lost around the machine than if particle coordinates would be sampled from the entire beam distribution.

Lastly, SixTrack-FLUKA coupling takes advantage of the detailed description of the collimator jaws and tank and utilises the same models that are later used by the dedicated FLUKA simulations. With the tracking simulations completed and all the relevant proton impact information (momentum, direction, impact position, impacted collimator) stored in a file, the last information passed to the next step is the ratio between impacting and lost protons. This ratio depends on the tracking simulation settings and it roughly reflects on the average amount of impacts a proton needs to be considered lost. For example, the smaller the impact parameter is, the higher this ratio usually becomes due to the protons traversing a much shorter path inside the collimator and therefore requiring a lot more turns/impacts for a deep inelastic effect to take place. For an impact parameter of 10 μm for protons this ratio is close to 1.5.

3.3.2 FLUKA simulations for protons

There are many challenges that setting up a simulation of such scale present. For example, to which detail the geometrical model should be described in the Monte-Carlo code. If the quantity under study is the power deposition in the collimator jaws, then there would be no need for the modelling of any surrounding components since the jaws are directly impacted by the particles lost from the beam. However, in the case of the benchmark against BLMs, apart from a detailed beam loss monitor description, practically all material that is located between the beam impact point and the gas region of the BLMs will significantly affect the signal registered. Unfortunately, it is either impossible or extremely man-hour consuming to describe every little detail of the actual elements located inside the LHC (i.e. cables, screws, covers, etc.).

Therefore, the more considerable uncertainty in the simulations is the accurate description of the IR7 geometry. This includes the geometrical dimensions, the material definition and the relative position of the most essential elements in the IR7, including, but not limited to, the magnets (normal and superconducting), the collimators (jaws, tanks and supports), the beam pipes, the tunnel and the BLMs. In addition, detailed and accurate magnetic field descriptions inside and outside the beam pipe are crucial for a realistic representation of both the beam trajectory and of the secondary particles since some of their energy will eventually be deposited in the BLMs.

Lastly, as it was seen in Chapter 2, due to statistical limitations, the simulations of the 700 m long geometry of IR7 were handled differently for the warm and cold sections. The following paragraphs will go through the setup of each section mentioning the major challenges and analyse the results of the benchmark against BLM measurements taken from the collimation quench tests.

Long straight section (warm section)

In this section, the proton simulation setup is presented along with the various challenges and compromises that were necessary for this second step of the simulation

chain. Then the BLM signals comparison between the simulations and measurements is shown and analysed. The remarks made here apply, for the most part, also to the ion studies.

Simulation setup

Usually, the lower the Monte-Carlo simulation thresholds one sets, the more accurate the simulation results will be in terms of physical processes. This, of course, depends on the needs of the simulations. While increasing the thresholds will definitely not improve the accuracy, it is often the case that doing so will not worsen it either since the extra accuracy is not necessary when the residual range of the transported particles is lower than what is required for the specific studies. In addition, it is often the case that the models that approximately handle the interactions bellow thresholds are sufficient. On the other hand, the lower the thresholds, the more CPU expensive your simulation becomes, and the user is often required to find golden ratio between the simulation accuracy requirements and the simulation speed.

For the case of simulating the dose deposited in the nitrogen gas of the BLMs of the LHC, it was seen, mainly through trial and error, that the best thresholds to be used for the warm section was 1 MeV for all particles other than electrons and photons which were set to 0.1 MeV. The reasoning behind these settings is that the range of the particles bellow those energy thresholds is shorter than the thickness of the metal casing of the BLMs surrounding the active nitrogen region. Therefore, these settings provided accurate enough results requiring a manageable, on average 10 min per primary proton for the secondary showers to be fully simulated after an inelastic interaction.

A dedicated scoring estimator in FLUKA (special USRBIN) was used to record energy deposition in all regions and lattices including the active nitrogen gas region of the BLMs that were defined as a single region to facilitate the post-processing of the deposited energy. The binary format of the scoring was used in order to take advantage of the FLUKA integrated tools, which are capable of summing up different run files to acquire better statistics. Specialised post-processing routines were used to extract the information from the usrbins after they were converted to ASCII format.

BLM signal comparison

For the needs of the benchmark, it was decided to utilise the least noisy longer running sum (RS12) that covered the total duration of the quench test when extracting the experimental BLM signals. Running Sums (RS) (48) are fixed time intervals where BLM data are stored and range between 40 μs and a few minutes. The final values are reported in Gy, reflecting the total dose that was recorded during the experiment contrary to the usual dose rate that BLMs record. In this way, the measurement uncertainty was minimised by avoiding instantaneous dips in the proton loss rate, especially for the BLMs with low signal levels. The respective background signals measured at a time right before the quench test, where no beam was present in the machine, was subtracted to evaluate only the signal that originates from the beam losses.

On the simulation side, the energy deposition values inside the active gas region of each BLM were scored and after dividing by the gas mass (density*volume), they are converted to dose per primary proton impacting the collimators. To reach the final values of total dose during the quench test, we multiply by the ratio impacts/lost protons and by the total number of protons lost, as was measured by the BCT (Equation (3.1).

Figure 3-7 (top) shows the comparison of the simulated values from FLUKA against the corresponding experimental ones. Each point in the graph represents one BLM illustrated with a yellow colour in the respective FLUKA geometry in the bottom part of the same figure. In the geometry plot, the major machine components at key locations are depicted for ease of comparison against the BLM signals plot. The statistical error of the simulations fluctuates between the BLMs according to the magnitude of the signal recorded. Even though optimized settings were used as far as the physics thresholds are concerned, the total simulation time was four weeks on a cluster with 80 CPU cores to achieve lower than 20% statistical error in the BLMs with signals of 10^{-2} Gy and below. The results for BLMs with signals of the order of 5 Gy and above have a statistical error of less than 1%. These errors are acceptable

within the other simulation uncertainties and improving this would require a considerable time investment with no apparent gains.

The results show a remarkable reproduction of the experimental signals spanning over five orders of magnitude in over 100 beam loss monitors. The differences between experimental and simulated points remain well within a factor of 2, with only a few notable exceptions. For example, the BLMs located between 100 m and 150 m from the IP are generally overestimated. These discrepancies, along with the others, can be likely attributed to the uncertainties and simplifications of the geometry characterisation in FLUKA. Overall, the pattern reproduction is extremely satisfactory given the complexity of the simulation setup and the length of the simulated geometry. In particular, no systematic disagreement between simulation and measurements is observed in the insertion region.

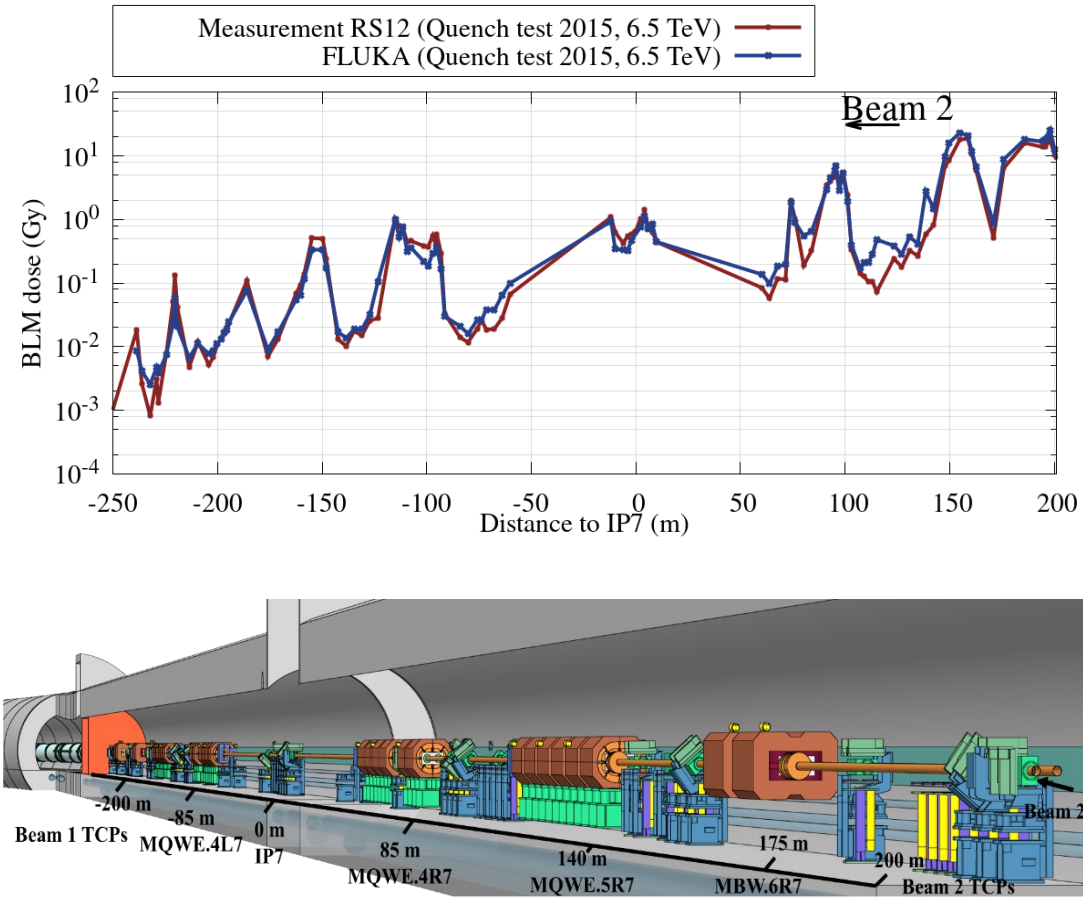

Figure 3-7: (Top) LSS measurements vs simulations of BLM signals during the 2015 proton quench test. (Bottom) Equivalent FLUKA geometry of the IR7 LSS of the LHC.

Some noticeable attributes of the pattern are that localised peaks are found at BLMs assigned to collimators of the same beam. While this makes perfect sense, since proton impacts on collimators are the primary source of beam-induced radiation, it is worth observing that while a general downward trend in the amplitude of the BLM signal is observed, it is not linear. While not applicable in this case were only beam 2 is studied, this effect will play a role when examining the crosstalk effect in a regular operational scenario when both beams are active in Chapter 4.

Dispersion Suppressor (cold section)

As mentioned in the previous section, the statistical error of BLM signals at the end of the insertion region, which is more than 400 m from the impacted Beam 2 primary

collimators, were of the order of 20%. The BLMs located even further downstream in the cold section are of the order of 10^{-3} Gy and less, meaning that acquiring enough statistics in the cold section to get an error of below 5% would require years of CPU processing power. To overcome this, the advanced two-step simulation method described in Chapter 2 was adopted.

Simulation setup

In a nutshell, the information of the particles that were exiting the radiation shielding wall, located right before the continuous cryostat hosting the superconducting magnets in the IR7 DS (roughly at -250 m) (Figure 3-7 and Figure 3-8), were stored in a file. Then these particles were oversampled and used as a source for a second dedicated simulation of just the cold section. The principle of this approach is that a statistically meaningful proton distribution of impacts inside the superconducting magnets was acquired through the first simulation step using high production and transport thresholds.

In this way, by oversampling, it is possible to explore the Monte-Carlo possibilities of a high energy proton interaction without the need of "wasting" most of the CPU time far away from the point of interest. For this method to work, the assumption was made that most of the energy deposited in the superconducting magnets originated from high energy proton losses. This idea was supported by the proton loss maps created by tracking simulations shown in Section 3.2.1, since the proton loss distribution exhibits the same gross features as the measured BLM patterns.

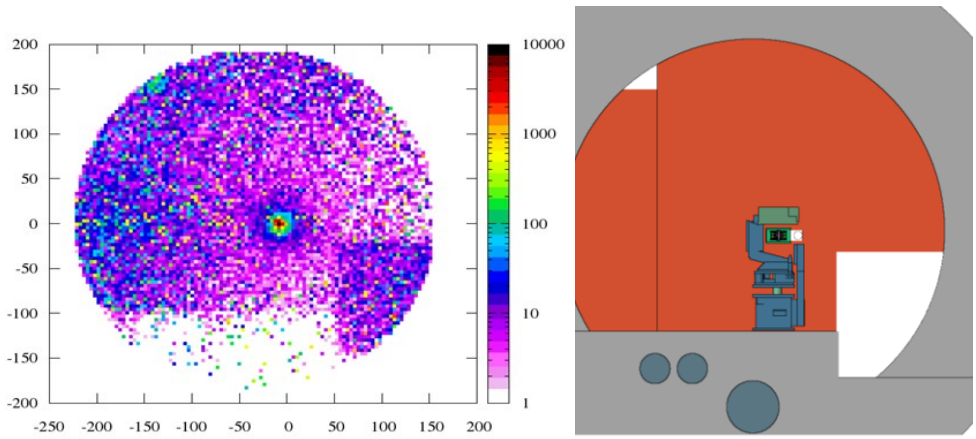

Figure 3-8: Geometry rendering of the last TCLA of beam 2 before the radiation shielding separating the warm and cold sections (right)
Energy density map of the particles escaping the radiation shield (a.u) (left)

BLM signal comparison

Figure 3-9 shows the experimental and simulated BLM signals at super-conducting magnets next to the betatron cleaning insertion. The BLM pattern is overall remarkably well followed in the simulations with many instances of very small discrepancies. It is noticeable, however, that the BLM signals at the high dispersion cells (cell 9 between -350 m and -300 m, cell 11 between -450 m and -400 m) are underestimated by roughly a factor of 3. The systematic discrepancy hints that the simulation chain seems to underestimate the leakage of the high energy protons to the DS.

The simulations presented so far considered only the contribution of protons lost on the aperture of DS magnets. However, since the BLMs are located outside of the superconducting magnets, it could be that the signal that is “missing” actually originates from upstream showers travelling outside of the magnets. To rule out this theory, the cold section simulations were rerun using specialised scoring routines in order to estimate the shower-induced signal contributions, which add on top of the contribution from the high energy protons that were lost inside the magnet aperture.

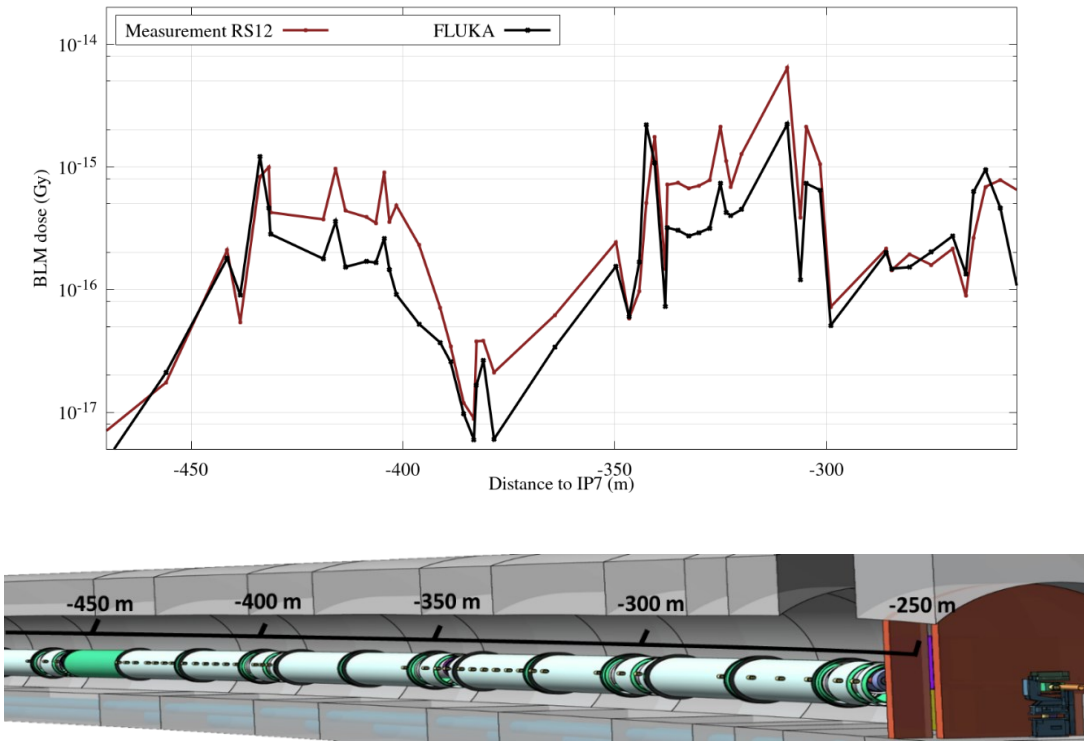

Figure 3-9: (Top) DS measurements vs simulations of BLM signals during the 2015 proton quench test. (Bottom) Equivalent FLUKA geometry of the IR7 long straight section of the LHC.

Loss contribution disentangling

In Figure 3-10 the BLM signals are disentangled between the portion that originates from secondary particles arriving at the DS from outside the beam pipe (upstream showers) and the one from protons that impact directly inside the beam pipe of the SC magnets. One can see that upstream secondary particles mainly contribute to the signal measured at the entrance of the DS (-300 m) while the same applies in the lower signal areas, such as between -400 m and -350 m, and downstream of -450 m. The signal at the entrance originates from secondary pions, kaons and muons while further downstream only the muons survive and contribute to the signal measured.

Other benchmark studies for different kinds of loss scenarios (49-51) that utilise the same dipole magnet FLUKA geometry show a better than 10-30% agreement between measurements and simulations. This indicates that the observed systematic offset in the DS is likely not because of possible mismatches between the SC magnet model

geometry and the real magnet. Moreover, the correct reproduction of the overall BLM pattern does not suggest local geometry model inaccuracies such as the position of the BLMs. Therefore, the above analysis provides strong evidence that the simulation chain is underestimating the number of protons that are lost inside the SC magnets or in other words, the cleaning inefficiency. Apart from possible uncertainties in the assumed impact distribution, described in 3.3.1, the rest of the simulation settings are those of a perfect machine.

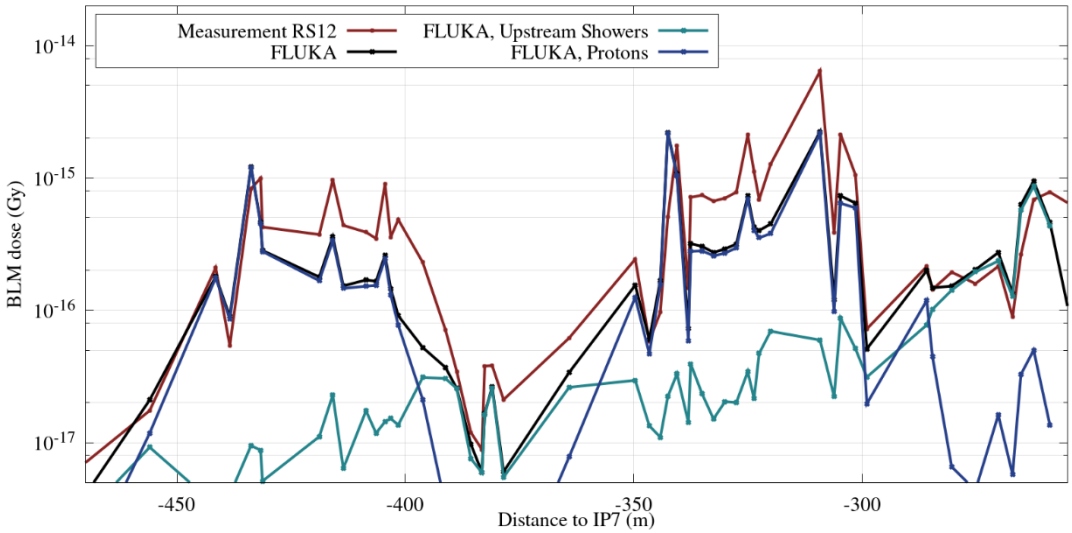

Figure 3-10: Measurements vs simulations of BLM signals in the DS during the 2015 proton quench test. The FLUKA patterns disentangle the contribution of high energy protons lost inside the SC magnet aperture and the contribution of upstream showers originating from outside the beam pipe.

3.4 Imperfection studies

Past studies (16,52) have already highlighted the detrimental effect that machine imperfections can have on the cleaning efficiency of the machine. These may include, beam centre errors due to orbit shifts, beam aperture imperfections, collimator gap errors due to optics errors, collimator misalignments etc. While all of these can play a significant role, the fact that the BLM pattern is so well reproduced for both DS loss clusters in cell 9 and cell 11, suggests that the reason behind this underestimation

should equally affect both loss locations. Furthermore, the BLM signal underestimation in close proximity to the primary collimator hints that the perfect beam impact conditions used for the simulations may be unrealistic.

For this reason, the misalignment of the primary collimators was considered for further studies. A collimator misalignment may either refer to the discrepancy between the angle that the collimator jaws have relative to the ideal beam orbit or the case where one jaw is closer to the beam than the other. In the ideal machine, this angle is zero and the jaws are equidistant to the beam centre.

3.4.1 Tracking studies

The reference ideal machine was reiterated in renewed tracking studies with the initial beam distribution sampled directly at the primary collimator front face (to facilitate the simulation setup) and with a smaller impact parameter of the order of 1 um and a pencil 4D beam distribution. The new results of the ideal machine tracking simulations suggested an increase in cold losses between 40% and 50% (53). Further reduction of the impact parameter did not induce a further increase in the cold losses.

The misalignment tests using the same settings as the above renewed reference case introduced an angle θ between the collimator jaws and the ideal beam orbit breaking their collinearity. Figure 3-11 shows the initial scenarios of misalignment that were considered where each case imposed different implications to the beam impact scenario. At first glance, it is apparent that the introduction of an angle would have the effect of lowering the “active” length that particles traverse through the collimator, and therefore have smaller chances of interacting. While this is true, there is no apparent reason that this effect would decrease the cleaning inefficiency on its own since the only downside of this is that it would take more turns for the particles to have an inelastic nuclear collision in the primary collimators.

The collimator surface roughness (in the order of 10 μm) could affect the actual impact points of the protons. One could assume that due to radiation impact the roughness could be reduced in time but this has not been confirmed. Nevertheless, in

the larger angular misalignments that are studied bellow the impact of collimator roughness would be minimized.

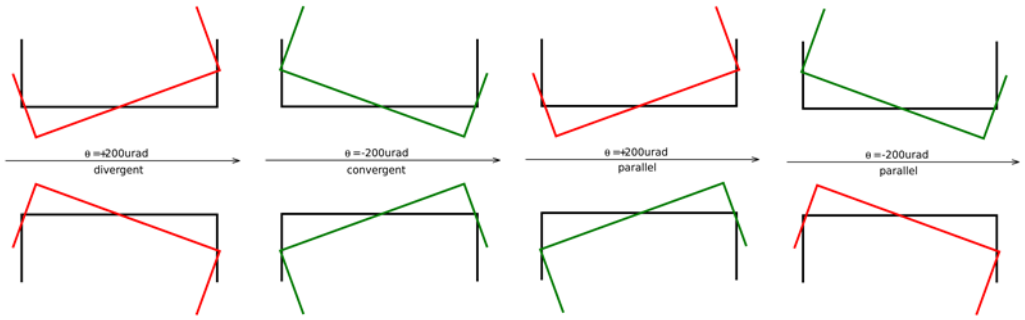

Figure 3-11: Different misalignment scenarios with |θ|=200 μrad (53)

The beta function of the machine at the position of the primary horizontal collimator, seen in Figure 3-12 (top), imply that the impacting particles have focusing angles. This fact makes the distribution even more sensitive to the imperfections. Additionally, the introduction of an angle introduces a shrinkage of the intended gap between the collimator jaws. In the case of 200 μrad this translates to a half-gap difference Δg=60 μm for the given primary collimator length of 60 cm as seen in Figure 3-12 (bottom). These two effects combined, introduce different impact scenarios for each case.

Figure 3-13 shows the first impacts on the primary horizontal collimator for the two jaws in each of the scenarios considered in Figure 3-11. The gap difference is there in all cases, which introduces an additional difference between the primary and secondary collimators imposing unintentional relaxed collimator settings leading to lower cleaning efficiency. Furthermore, in the cases of parallel jaws due to the particle converging angles, the upstream sigma is lower than the downstream one making the front face of the collimator jaws the bottleneck. This causes the beam to be primarily cleaned by only the front tip of the jaw that is closer to beam in the upstream side (e.g. the red jaw in the parallel cases of Figure 3-11 bottom).

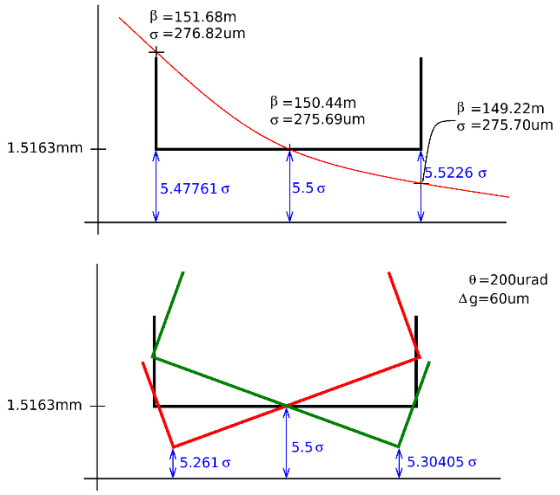

Figure 3-12: Beta function and sigma at the TCP (top).
Sigma values with θ=200 µrad and incurred gap difference Δg (Bottom) (53)

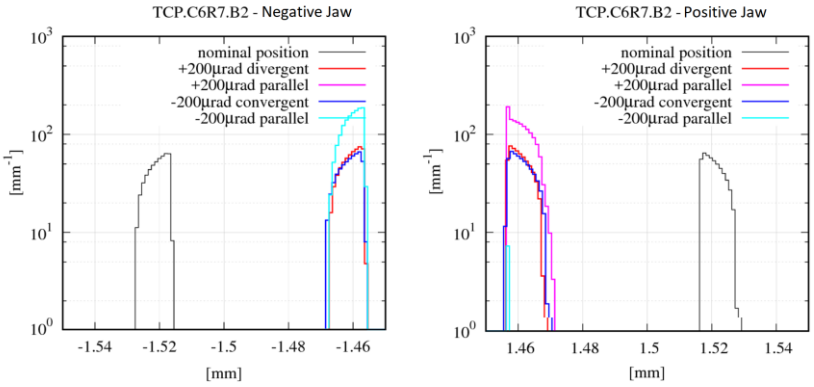

Figure 3-13: Transverse impact parameter distribution on the primary horizontal collimator (TCP.C) for each misalignment scenario considered in Figure 3-11. Only first impacts are shown, while multi-turn impacts are neglected (53).

Tracking simulations are, in general, much less CPU demanding than the full FLUKA simulations. For this reason, the above-mentioned cases were run in tracking simulations in order to identify the worst-case scenario in terms of cleaning efficiency. The results indicated that the worst cleaning efficiency scenarios were the ones with the -200 µrad parallel jaws and the +200 µrad diverging jaws. In reality, the relative position of each jaw compared to the other is mechanically well known in the order of tens of micrometre accuracy (given the a 5 µm positioning resolution of the jaws (14)).

For this reason, the jaws are parallel with high precision making the parallel scenario a much more plausible scenario. Furthermore, given the focusing angles of the impacting beam (see beta function at Figure 3-12) the optimal collimator alignment should in principle be convergent jaws matching the beta function and not parallel as it is assumed.

As mentioned, another case of imperfection could be the off-centre alignment of the collimator jaws were one jaw is closer to the beam than the other which would push one jaw closer to the beam core without reducing the collimator gap.

Assuming a 60 μm offset with a θ= 200 μrad is not exactly identical to a θ= 400 μrad for all cases. However, in the parallel jaws scenario, due to the first impacts being focused only on one jaw, the main difference stems from the higher probability of secondary proton scattering in the primary collimator. Driven by study time restrictions, to virtually combine the two cases and offer a worst-case scenario, it was decided that the case of +400 μrad parallel jaws scenario would be fully further studied with the FLUKA simulation model.

3.4.2 FLUKA simulations with TCP misalignment

Due to the high CPU time requirements of the FLUKA simulations, only a representative case was fully simulated in order to establish whether such a scenario is realistically plausible by comparing to BLM measurements. Even though the overall BLM agreement is already quite satisfactory in the warm section, the LSS was also studied to check for additional unexpected changes in the loss pattern that could give further insight into the hypothesis that collimator jaws are tilted with respect to the beam.

Due to the small impact parameter used in the present study, the ratio between multi-turn impacts on the primary collimator and inelastic interactions was of the order of 2000, which made the use of the impact positions as source for the FLUKA simulations, impractical. To overcome this, the positions of the first inelastic interaction in each turn were used as input for the FLUKA simulations.

Figure 3-14 shows the comparison of the experimental BLM signals and the simulated ones of the ideal machine (as presented in 0) against the simulated case of the 400 μrad jaw tilt. The figure shows BLMs in the straight section only.

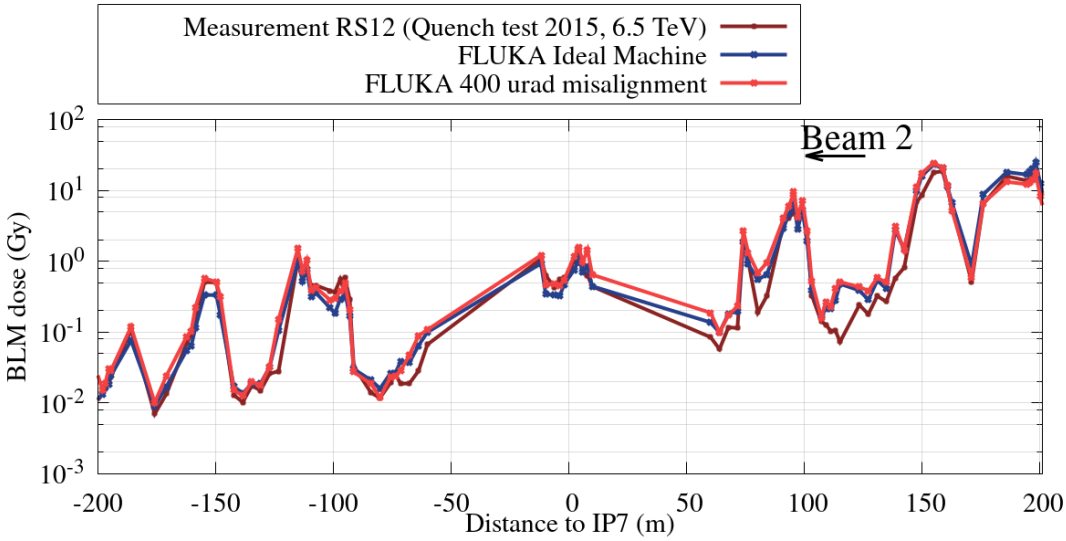

Figure 3-14: Measurements vs simulations of BLM signals in the LSS during the 2015 proton quench test comparing the ideal collimator settings vs a 400 μrad parallel jaw tilt of the primary collimator jaws.

The results show that the BLM signals are not dramatically different between the two simulated cases. Moreover, a systematic pattern difference can be observed close to the primary collimator (200 m), affecting the agreement vs the experimental data. These results enforce the thesis that such an imperfection would not be noticeable in the BLM signals in the LSS apart from the BLM signals close the primary collimator.

As was seen in section 0, the BLM measurements at the entrance of the DS are well described by the shower leakage from the straight section even for the case without imperfections. . Having already observed a similar agreement throughout the warm section between the two simulation scenarios, it is assumed that there is no reason for this agreement to be significantly changed with the introduction of the collimator tilt. Therefore, to save computing time, only the proton losses in the cold section were simulated for the imperfection case.

To facilitate the comparison between the reference case and the case with imperfections for the cold section, Figure 3-15 is an enhanced case of Figure 3-10 presenting, in addition, the imperfection case of the BLM signals generated by showers originating from high energy protons impacting inside the super conducting magnet aperture.

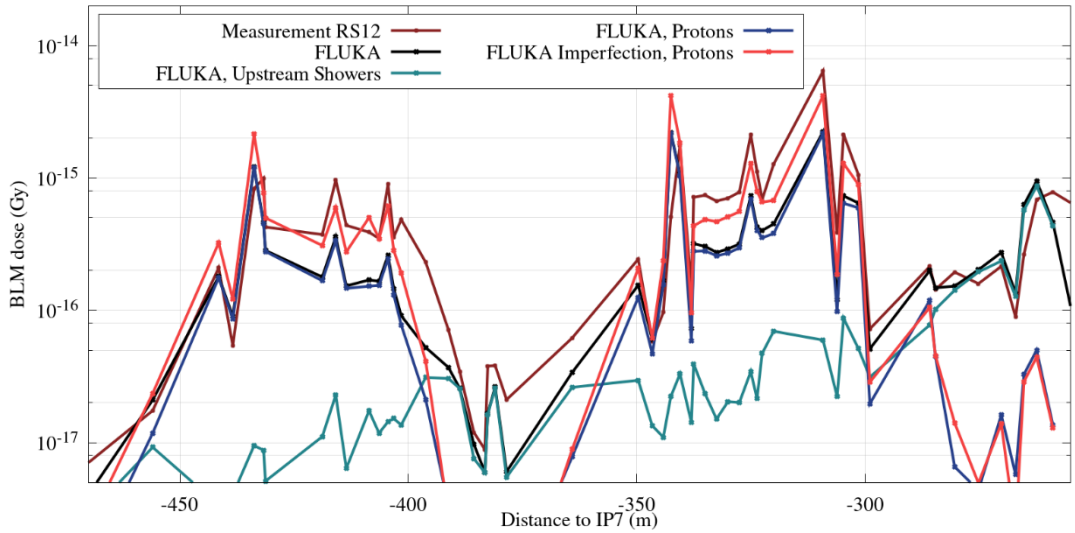

Figure 3-15: Measurements vs simulations of BLM signals in the DS during the 2015 proton quench test. Simulation results of protons lost inside the SC magnets for misaligned (400 µrad tilt, red curve) and ideally aligned primary collimator jaws (blue curve). For the latter case, the figure also displays the contributions of upstream showers originating from outside the beam pipe (green curve) as well as their cumulative effect (black curve).

The results show a significant improvement in the overall agreement of the cell 9 and 11 regions without a substantial change of the overall pattern. The one-to-one comparison of the reference "FLUKA, Protons" curve (ideal collimator alignment) vs the 400 µrad parallel jaws misalignment "FUKA Imperfection, Protons" curve shows that while an underestimation of the experimental signals is still present, this has been reduced to less than 50% compared to the factor of 3 for the case with ideally aligned jaws. The underestimation of measured signals in cell 10 (-400 m to -350 m) is due to the missing contribution of upstream showers originating from outside the beam pipe.

Overall, this study strongly supports the assumption that imperfections are very likely present in the LHC machine. Given the sensitivity of the cold losses to these imperfections, the overall capabilities of the simulation chain have proven to be remarkably robust. While discrepancies are still there, the study has sufficiently characterised and quantified the predictive ability of the simulations for determining other quantities such as the peak power deposition in the SC coils presented in Chapter 6.

The results have already initiated more detailed alignment studies in the LHC with the goal of reducing the effect of imperfections and thus improving the overall performance of the collimation system.

3.5 Ion benchmark against BLMs

In this section, the studies of the simulation chain benchmark against the BLM signals of the 2015 Pb ion quench test are presented. Both the tracking and Monte-Carlo tools had to be heavily reworked to become capable of handling different ion species since also lower mass fragments with a similar magnetic rigidity as the beam particles can travel longer distances inside the accelerator. The simulation chain remains practically the same as with protons, but specific challenges are further explained in this section. Lastly, the setup and results of the benchmark using lead ions are presented in detail.

3.5.1 SixTrack-FLUKA coupling tracking simulations for ions

Similar to protons, tracking simulations are performed with lead ions using the hiSixTrack-FLUKA coupling tool (19) to score their impact positions on the collimators. This modified version of the SixTrack-FLUKA coupling takes into account the fragmentation of heavy ions and can handle all secondary fragments that are generated after a heavy ion collision with the collimator. The same reasoning, as with protons, applies to ions for exploring the multi-turn effects, while it has extra importance for ions due to secondary fragments with the right magnetic rigidity surviving a single pass but eventually getting lost after some turns.

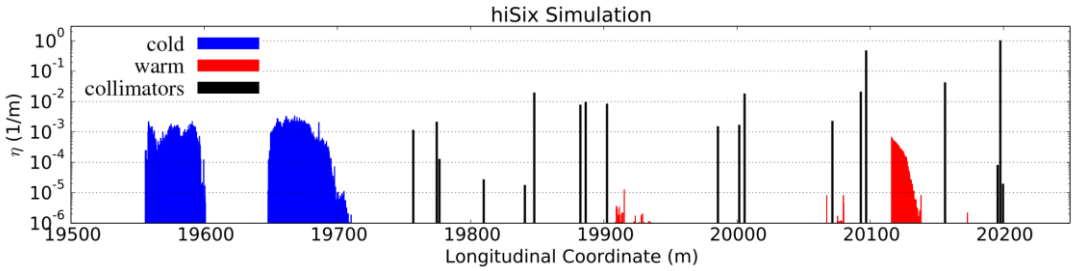

Figure 3-16: Tracking simulation energy loss map for the 2015 lead ion quench test (41).

When an ion undergoes an interaction all secondaries above a certain threshold of magnetic rigidity are tracked until they either impact on the aperture. The particles then are considered lost and a loss map of the total energy lost per meter of the machine is created by the tracking simulations. Figure 3-16 shows the loss map created by the tracking simulations in IR7 for the case of the 2015 lead ion collimation quench test. Nevertheless, as for the protons, the full particle shower information is required to expand on this qualitative information and compare against the experimental BLM signals.

The same collimation settings as for protons were used during the ion quench test as seen in Table 3-1. Furthermore, the same simulation settings were also used for consistency as seen in the same table apart from the maximum initial impact parameter, where 3 μm were used. Another minor difference is the particle energy and therefore the magnetic field settings which were set for 6.37 Z TeV instead of 6.5 TeV. This difference is a bit unorthodox since the collimator settings were used for the proton 6.5 TeV case, but it was exceptionally done during the quench test and therefore it was also adopted in the simulations. The consequence is that the results may not be strictly used for loss estimations of the nominal operational scenario of the previous years like in the proton case (see Chapter 4), but since the ion runs contribute only to a very small percentage of the total operation, this is a minor drawback.

Similarly, to protons, the final output of the tracking simulations is a file containing the information of the first impacts per turn of the particles arriving at the primary horizontal collimator. The difference is that in the case of ions, the impacting particles are, apart from the original lead ions, also the secondary ion fragments that had just

the right magnetic rigidity and phase space coordinates to survive beyond a single turn and re-impact the primary collimator. Nevertheless, even though their energy per charge is close to the beam rigidity, these other families of particles account for less than 1 per mil of the total energy of the impacting particles, while the dominating contribution is due to lead ions.

3.5.2 FLUKA simulations for ions

The FLUKA input used for the second stage of ion simulations took advantage of the geometrical model of the IR7 cleaning insertion and the scoring that was used for protons. The same uncertainties and difficulties inherently apply to both situations. In this section, the additional requirements and simulation setup specific to the heavy ion run are described. All settings that are not explicitly mentioned in the ion setup section should be considered the same as was described for the proton case. Lastly, the warm and cold section BLM signal comparison against the 2015 ion quench test experimental data is presented and analysed.

Simulation setup for ions

To begin with, an extra effort was required to extend the source routine capabilities to import all families of particles, as opposed to just protons that was previously used. Moreover, the physics settings had to include special cards to enable relevant physics processes of heavy ions, such as electromagnetic dissociation, coalescence, pair production as well as nuclear fragmentation and evaporation. Consequently, the RQMD and DPMJET-III (54-56) physics model implementations in FLUKA had to be utilised for the above to take effect.

These additional physical processes, along with the roughly 80 times more energy per 6.37 Z TeV $^{208}Pb^{82+}$ ion, require a significantly higher CPU time to be simulated. Considering the weeks needed for the proton quench test to be fully simulated, the time requirements are prohibitive. Furthermore, in the case of ions, a large percentage of the CPU time is “wasted” in the same interactions close to the source, i.e. the collimators.

To acquire meaningful statistics a few hundred meters downstream from the impact point in a reasonable time frame, two biasing techniques were utilised. The Russian roulette with a 20% reduction factor and the leading particle biasing variance reduction techniques were enabled in order to reduce the secondary particle generation and allow for the more energetic ones to survive respectively (57). In this way, processing power is diverted downstream by partially omitting the simulation of highly repetitive physical processes.

BLM comparison for the 2015 ion quench test

The scoring setup of the simulations for ions is identical to the proton case and therefore the same considerations concerning the scoring of energy deposition apply, as described in section 3.3.2. The BLM comparison is presented for both the LSS and the DS and results are analysed in the following.

Long straight section (warm section)

The energy deposition per impacting particle in the active gas region of each BLM is scored and converted to dose by dividing by the gas mass. The final values of total dose during the quench test are calculated by multiplying with the impacts/lost lead ion ratio (around 1.2) and by the total number of lost ions as was calculated by the measured charges from the BCT (formula (3.2)).

The comparison of the simulated values from FLUKA against the experimental ones for the 2015 ion quench test is shown in Figure 3-17 (top), with the equivalent FLUKA geometry model shown in the bottom. The signals from different BLMs (in yellow) are represented by different points in the graph. The key machine components are mentioned for comparison against the BLM signals plot. The total simulation time was two weeks on a cluster with 80 CPUs to achieve a statistical error better than 20% for BLMs with signals below 10^{-2} Gy. For BLMs with signals above 0.1 Gy, the statistical error is less than 1%. These statistics are acceptable within the simulation uncertainties.

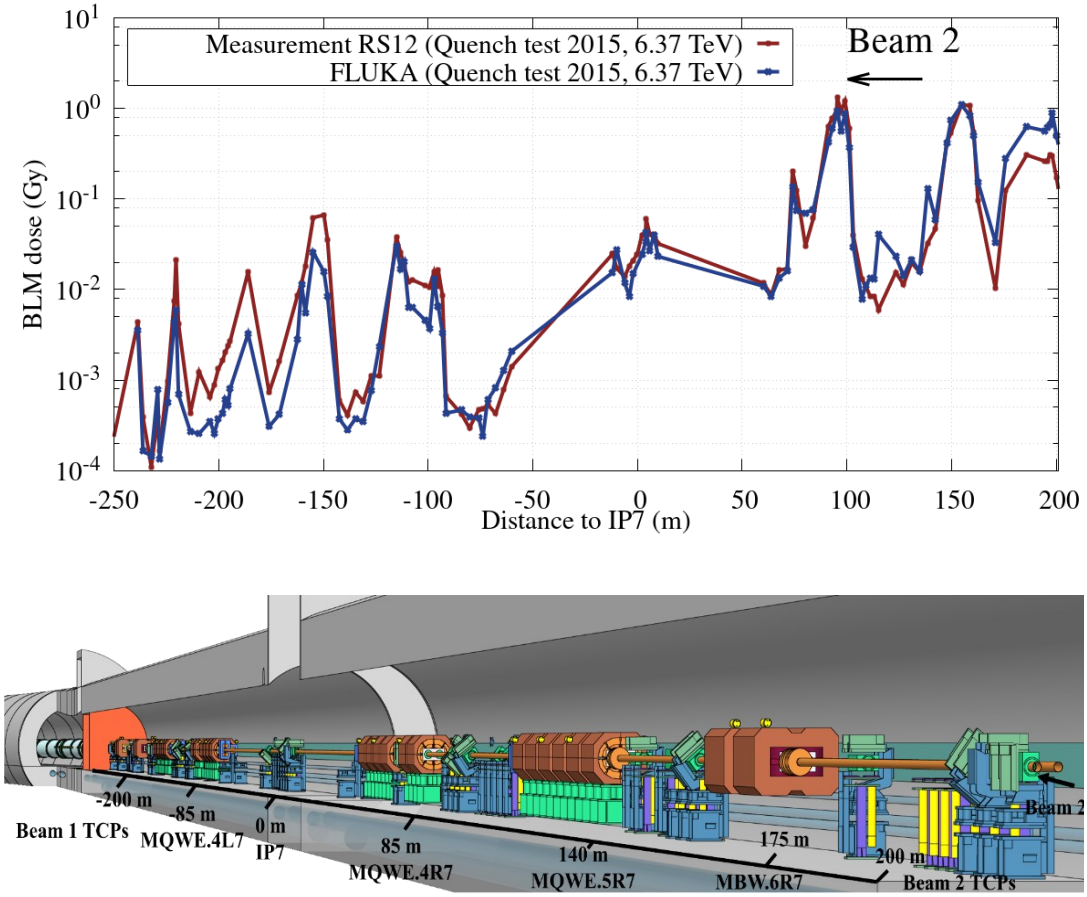

Figure 3-17: (Top) Measurements vs simulations of BLM signals in the LSS during the 2015 $^{208}Pb^{82+}$ ions quench test. (Bottom) Equivalent FLUKA geometry of the IR7 LSS of the LHC.

The overall agreement between the two graphs is very encouraging in terms of benchmarking the tools, showing that the simulation chain works just as well for ions. While discrepancies are more pronounced than the proton case, this first-ever collimation loss benchmark with ions highlights the predictive ability of the tools.

The discrepancies that were observed in the proton benchmark are clearly also visible in this case, such as the BLMs located between 100 m and 150 m that are generally overestimated. However, these discrepancies are attributed to the uncertainties and simplifications of the geometry characterisation in FLUKA. Overall, the pattern reproduction is satisfactory given the magnitude and complexity of the new tools.

A notable feature of the pattern is the enlarged overestimation of the BLM signals close to the beam 2 primary collimators compared to the protons. One explanation for this could be that the effect of a possible misalignment for ions might be much greater than that for protons. For example, it was shown in Figure 3-14 that with the introduction of angular misalignment in the proton simulations, the signals close to the TCPs were significantly lowered. Moreover, the systematic underestimation of measurements downstream of -100 m could be caused by the same imperfection.

Dispersion Suppressor (cold section)

The two-step resampling method that was used for protons was extended to include all ions (fragments included) that had the right magnetic rigidity and phase space kick in the primary collimator to eventually impact inside the DS SC magnets. However, the DS simulation for ions had to rely exclusively on the particles arriving in the cold section inside the beam pipe.

Due to the use of biasing techniques, the information of upstream showers arriving at the DS from outside the beam pipe was technically too complex to include. Furthermore, given the proton analysis shown in Figure 3-10, it was safe to assume that at least for the BLMs covering the major loss clusters the contribution would be minimal.

The DS benchmark of the lead ion quench test of 2015 is shown in Figure 3-18. Some of the experimental BLM signals are missing due to their signal being too close to the background noise levels during the test. The simulated response at the same locations are the ones with the worst statistical convergence with a statistical error of up to 40%.

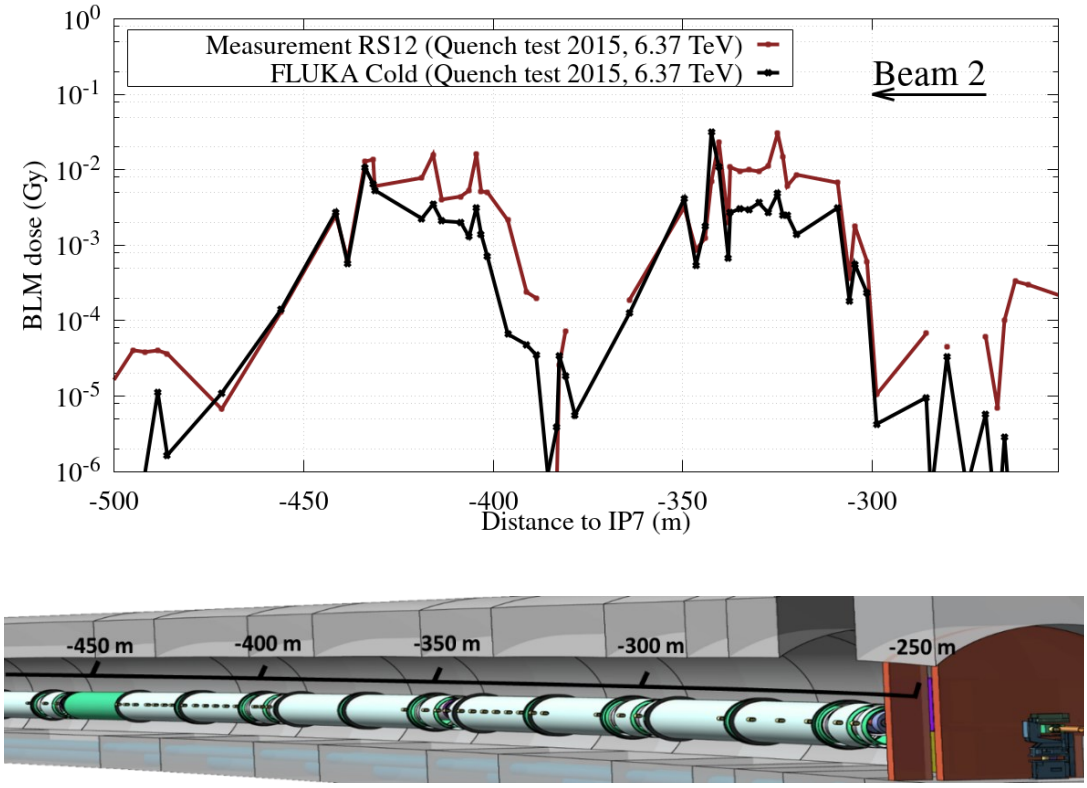

Figure 3-18: (Top) Measurements vs simulations of BLM signals in the DS during the 2015 $^{208}Pb^{82+}$ ions quench test. (Bottom) Equivalent FLUKA geometry of the IR7 long straight section of the LHC.

Once again, the pattern is generally very well followed especially considering the simulations do not include the upstream showers that, as was seen in section 3.3.2, highly contribute in the low signal areas at the upstream end of the DS (z>-300 m) and in cell 10 between -400 m and -370 m. The discrepancy at the dispersive areas (between -350 m and -300 m / between -450 m and -400 m) are underestimated by a factor of 4-5 which is considerably worse than for the proton benchmark. Nevertheless, the well-followed pattern, even in these underestimated areas combined with the proton benchmark results suggests that the cause of this discrepancy is probably due to the underestimation of ion fragments leaking to the DS. As for protons, this could be related to the assumed halo loss distribution and to imperfections.

Complementary tracking studies on a smaller impact parameter (19) suggest a further increase in losses at the cold section with a submicron impact parameter. Considering these findings, it is worthwhile to further explore imperfections for the case of ions, the effect of which seems to be much more pronounced.

3.6 Conclusion

The benchmarks against the beam loss monitor measurements offered unprecedented feedback on the overall accuracy of the simulation chain for betatron collimation losses. While qualitative comparisons between tracking simulations and BLM loss maps allow for an indirect way of validating the tracking simulation results, they offered no insight in quantifying the number of losses compared to reality. This study offered the first one to one translation of particle losses to BLM signals considering the full physical geometry and the particle shower development. In the case of protons, the benchmark results highlighted the immense capabilities of the different simulation tools with a remarkable reproduction of the BLM pattern and an excellent quantitative agreement in the LSS.

In the DS, a factor of 3 underestimation of the experimental signals was found, notwithstanding the overall pattern was well followed. Furthermore, the study provided an intuitive understanding and quantification of the effect of misalignment imperfections and sparked new studies into mitigating their effects. In the first-ever BLM simulation benchmark for ion collimation losses, the same principles were applied, and while the results showed a compared to the protons, they were still very satisfactory and offered a baseline for further simulation improvements.

Chapter 4 Run 2 betatron cleaning loss analysis and HL predictions

This chapter presents the analysis of the Run 2 experimental BLM and BCT data in the scope of evaluating betatron proton losses and extrapolating for the HL-LHC era.

4.1 Introduction

To make predictions related to the impact of long-term radiation damage to the equipment involved in the betatron collimation area, the total proton losses that are expected within the HL-LHC lifetime need to be evaluated. To this end, a method to estimate the number of proton losses induced by their interaction with the betatron collimators during Run 2 was developed.

To be able to draw conclusions from the Run 2 experience, it was necessary to evaluate the current collimation losses and create a link to a measurable and predictable quantity. Using the BLM signals from the operational years 2015-2018 and scaling them to the simulated ones, based on the benchmarked simulated BLM signals per proton lost shown in Chapter 3, an estimate of the betatron losses for each year is presented. Moreover, differentiating according to the different beam modes (e.g. injection physics, prepare ramp, collision physics etc.) it was possible to disentangle the losses for injection and top energy. Lastly, by looking at a subset of the BLM signals in Point 7 where losses from one beam dominate over the losses of the other beam, it was feasible to disentangle Beam 1 and Beam 2 losses.

A summary table of the estimated proton losses for Beam 1 and Beam 2 for injection and top energy protons for the years 2015 – 2018 is presented. These losses are then

scaled to the HL-LHC using an empirical correlation with the time integrated proton intensity measured during the different beam modes.

4.2 Method for determining proton losses in the betatron cleaning insertion

The LHC machine data concerning BLM signals are available through the CERN accelerator Logging Service that is either easily accessed using the Timber application or, for a more refined and detailed query, by utilising a custom modified version of the PyTimber script that is available in GitHub (58).

4.2.1 Experimental data split into beam modes

The study presented in this chapter is based on previous work by O. Stein, K. Bilko et al. (59), who extracted cumulative dose signals recorded by the BLMs for each year, as well as the percentage that each beam mode contributes to the total. A data sample for the year 2015 is shown in Table 4-1. The data includes the BLM identifier name according to LHC code naming followed by an underscore and the code name of the element that the BLM is attached to. The total cumulative dose is presented in Gy next to the distances of the BLMs with respect to interaction points 1 and 7 (IP1 and IP7 respectively). Then, the percentages that the different beam modes contribute to the total are shown in their respective columns.

For this study, we focused on the major contributing beam modes (60). The “INJECTION PHYSICS” and “PREPARE RAMP” modes are summed up since in both cases protons have an energy equal to 450 GeV. The “FLAT TOP”, “SQUEEZE”, “ADJUST” and “STABLE BEAMS” modes are grouped together to study the contribution of top energy protons, equal to 6.5 TeV for Run 2. The “RAMP” mode corresponds to the losses during the energy ramp and therefore is not assigned to any of the two categories, since protons at different energies give rise to different BLM signals. This makes it difficult to quantify the losses in this beam mode.

However, since the BLM dose during the energy ramp amounts only to a small fraction of the total BLM dose only (less than 5% in the vast majority of BLMs) the contribution of losses in the ramp is expected to be small compared to the beam modes at injection and top energy..

Table 4-1 – Sample of the cumulative BLM signals according to beam modes for the year 2015

BLM identifier name	Total dose (Gy)	Distance from IP1 (m)	Distance from IP7 (m)	INJECTION PHYSICS BEAM	PREPARE RAMP	RAMP	FLAT TOP	SQUEEZE	ADJUST	STABLE BEAMS
BLMTI.06R7.B1E10_TCLA.B6R7.B1	7615	20180	185,89	24,40%	1,47%	6,74%	1,55%	4,77%	11,95%	49,07%
BLMEI.06R7.B2I10_TCHSS.6R7.B2	6662	20188,67	194,47	33,36%	1,96%	6,12%	1,35%	3,87%	10,38%	42,91%
BLMEI.06R7.B2I10_TCHSH.6R7.B2	6697	20189,87	195,67	35,06%	2,04%	5,92%	1,31%	3,68%	10,11%	41,82%
BLMEI.06R7.B2I10_TCHSV.6R7.B2	7676	20191,07	196,87	36,59%	2,10%	5,70%	1,27%	3,43%	9,84%	41,00%
BLMEI.06R7.B2I10_TCP.A6R7.B2	7531	20192,27	198,07	37,51%	2,11%	5,44%	1,24%	3,23%	9,70%	40,69%
BLMTI.06R7.B2I10_TCP.B6R7.B2	4466	20194,27	200,07	42,96%	2,29%	4,95%	1,14%	2,65%	8,78%	37,15%
BLMTI.06R7.B2I10_TCP.C6R7.B2	3471	20196,27	202,07	60,20%	3,15%	4,64%	1,04%	1,43%	5,98%	23,45%
BLMTI.06R7.B2I10_TCP.D6R7.B2	1122	20198,27	204,07	79,28%	4,48%	4,12%	0,65%	0,76%	2,34%	8,25%

In Figure 4-1, an indicative plot of the subset of BLM signals concerning the study of Point 7 is shown for the year 2015. The two lines concerning injection and top energy form, as expected, two different patterns of losses due to their different energy, where the shower developed by the 6.5 TeV protons extends much further than the 450 GeV ones. Close to the primary collimators at -200 m and 200 m for Beam 1 and Beam 2 respectively, the contributions from the two energy levels to the total dose are comparable, while further downstream from the two sources, the contribution of top energy protons dominate. Due to the smaller energy per proton, one should expect a higher number lost at injection in order to account for the same amount of cumulative dose at the primary collimators.

The comparable signals, observed at some BLMs between injection and top energy protons, indicate that beam losses at injection energy can yield a non-negligible contribution to radiation effects in primary collimators. Prior to this analysis, it was assumed that due to the much lower injection energy, radiation impact on elements would be dominated by top energy protons. The BLM signals however suggest that this holds only for elements located further downstream of the primary collimators.

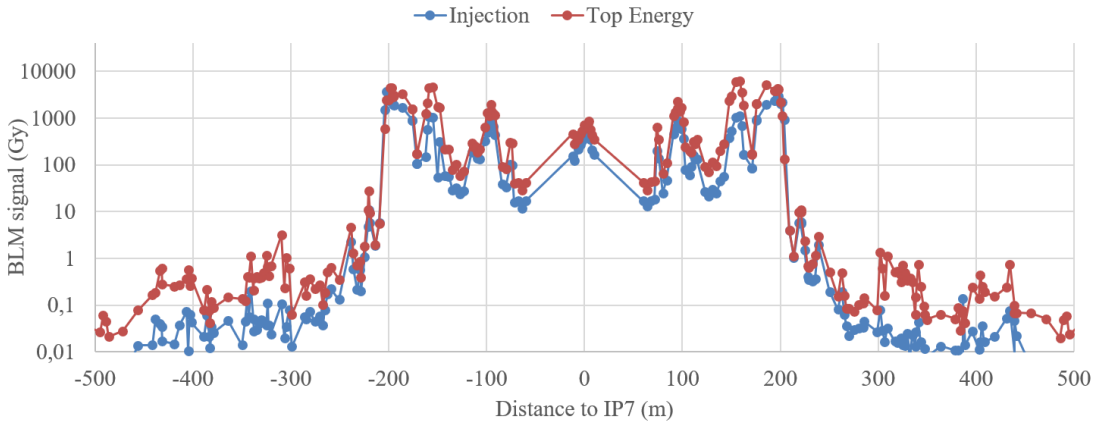

Figure 4-1: 2015 cumulative BLM signals for injection (450 GeV) and top energy (6.5 TeV).

4.2.2 Data analysis process

The data analysis procedure is split into two main sections which are introduced in this chapter.

- The pre-processing of the data. Specifically, selecting a specific subset of BLMs suitable for studying the warm and cold sections as well as each beam separately.
- The processing of the data to evaluate the number of protons lost in each case.

Data pre-processing

The data concerning the BLMs in the warm and cold sections of IP7 for the years 2015-2018 are split based on their distance to the primary collimators of each beam and analysed according to the classification of top and injection energies. Out of roughly 230 BLMs located within 1 km in IP7, specific subsets of the BLMs were grouped in order to disentangle the losses according to Beam 1 and Beam 2.

For each beam, the BLMs located within a distance of 140 m with respect to the primary collimators (e.g. in the region from 60 to 200 m for Beam 2) are taken into consideration when studying warm section losses. This choice was made to minimise the effect of crosstalk between the two beams since BLMs are natively incapable of separating the recorded dose depending on its source. Although BLMs are positioned

closest to the element that they are designed to protect, such shower crosstalk is inevitable.

The BLMs located in close proximity to the primary collimators are dominated by showers from the respective beams regardless of whether they are assigned to the other beam or not. On the other hand, the BLMs of some active absorbers record primarily the dose originating from losses on the other beam. This can be observed in Figure 3-7, where only beam 2 showers are present. In that case, the signal levels observed in the Beam 1 primary collimators at -200 m is orders of magnitude lower than the symmetrical ones at beam 2 primary collimators at 200 m. This phenomenon allows for the opportunity to disentangle the losses between the two beams by studying a subset of BLMs that are single beam dominated.

The cold section BLMs will not be considered at the stage of evaluating the Beam losses due to a couple of factors. First, the level of BLM signals in the DS is heavily dependent on the collimator settings, the effect of which has only qualitatively been studied, and can be significantly affected by machine imperfections (see 3.4). Secondly, the signal levels are very low and therefore susceptible to record, apart from collimation, also other kinds of losses such as beam-gas interactions accumulated over the years.

Data processing for proton loss evaluation

After the data are pre-processed and split according to beam and energy for the warm section, they were analysed using Octave (61). The concept of the data analysis is to find the number of protons lost every year by finding the best match between simulated and measured BLM signals. that, when the BLM data are normalised to, the resulting dose/proton lost will match the simulated ones. One could argue that the opposite should be done, i.e. to scale the simulated values with the number of proton losses to reach the measured ones. The former was chosen to facilitate the graphical comparison of the years with large numerical differences in the losses.

Mathematically this was done through a custom routine that, starting from a given estimated number of proton losses, evaluated a cost function for each BLM using

equation (4.1). The cost function is a quantity often used in machine learning that represents the measure of agreement/disagreement of the model to the experimental data. In cases where the result in the parenthesis was lower than 1, it was inverted to keep the cost for each BLM comparable to each other no matter if the model is overestimating or underestimating the experimental value. Scanning over different number of proton losses, the one with the lower cost was considered to be the more representative.

$$cost = \sum_{\#BLMs} \left(\frac{\frac{Cumulative\ BLM\ singal}{Estimated\ \#\ of\ protons\ lost}}{Simulated\ BLM\ signal\ per\ proton\ lost} \right) - \#BLMs \quad (4.1)$$

Specifically, and uniquely, for top energy beam 2 where measurement data from a controlled beam loss experiment are available, the cost function was evaluated by multiplying the target simulated BLM signals per proton lost by the mismatch ratio from the benchmark. For example, if for one BLM the ratio between the simulated value and the benchmarked value was a factor of 2, then the simulated value mentioned in equation (4.1) was increased by a factor of 2 to better take into consideration the mismatch between simulations and data. This technique was not available for the rest of the cases due to the lack of experimental data, but due to the already good agreement between data and simulations, the results are still valid but with a more considerable margin of error.

4.3 Evaluation of annual betatron losses in LHC Run 2

In this section, the results of the beam loss analysis are presented, showcasing the final scaled BLM patterns in the warm section and the cost function plots. Furthermore, qualitative conclusions on the accuracy of the estimated losses of the method are drawn.

4.3.1 Top energy losses (6.5 TeV)

The study of top energy losses is of the highest importance since the BLM maps show that they have the most significant impact in both the normal and superconducting magnets.

Beam 2 6.5 TeV losses for 2015-2018

Starting from the more robust case of Beam 2 top energy (6.5 TeV) where the benchmark was thoroughly presented in 3.3, the result of the cost function is illustrated in Figure 4-2. Years from 2015-2018 are presented in the same plot with the losses mentioned in the legend, representing the value that produces the lowest cost. The plot's inverse peak sharpness and value can be interpreted as an accuracy measure, with a sharper, closer to zero, peak representing a better match of the data to the simulations and therefore a smaller error. Since the simulation results for Beam 2 are from the year of 2015 with the collimation setting of the same year, it is expected that this will produce the smallest cost value of all the years as well as the sharpest peak.

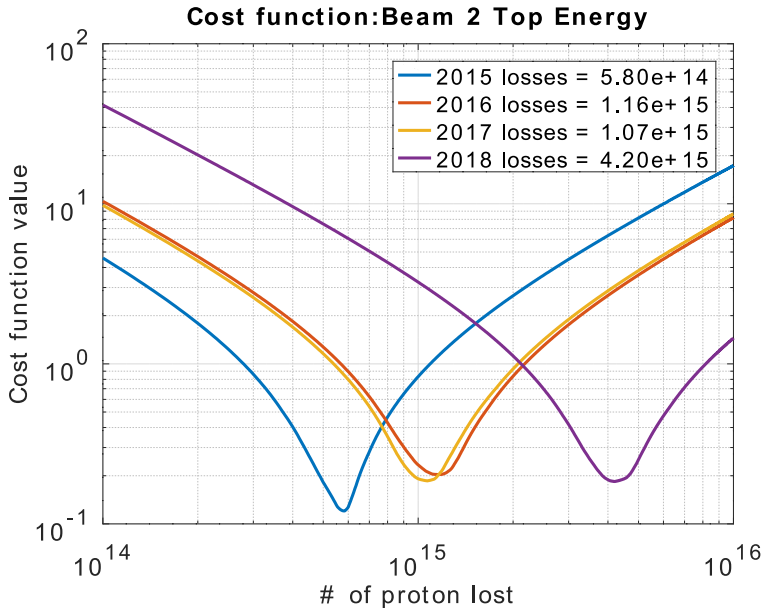

Figure 4-2: Cost function plot, evaluating losses for top energy (6.5 TeV) protons in Beam 2. The losses mentioned in the legend are the ones that bear the minimum fitting cost for each year.

Using the calculated number of protons, the BLM pattern on the right side of the IR7 warm section is plotted for each year in Figure 4-3. One can immediately notice a consistent agreement between the different years, as well as an excellent agreement with the simulation data, as expected from the quench test agreement. The discrepancies between the simulated plot and the data remain similar to the ones of the quench test, as designed by the cost function calculation mentioned above. Furthermore, it is evident that even though the collimator settings between the years are changing significantly (Table 2-1), due to the high amount of losses, the loss pattern seems to be relatively unaffected. This, of course, applies only to the warm section and does not hold for the cold section where the leakage of the diffractive protons highly depends on the collimator and optic settings.

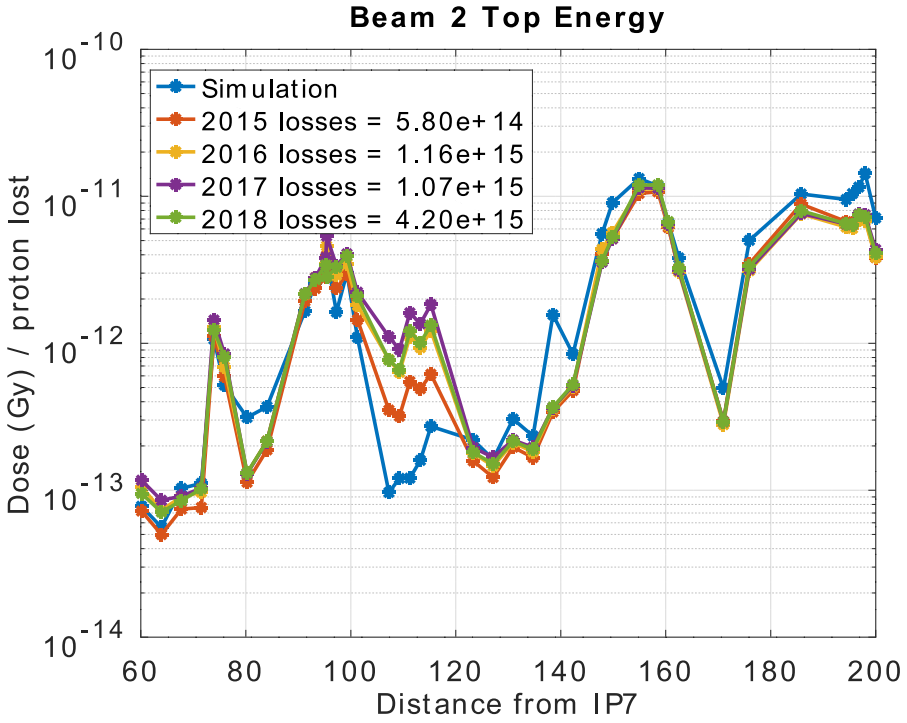

Figure 4-3: Comparison of simulated and measured BLM patterns (2015-2018) for Beam 2 proton losses at top energy (6.5 TeV). The measurements were divided by the number of protons lost in each year, determined in the previous figure.

A major exception to the agreement can be observed in the BLMs located between 100 m and 120 m from the IP7 where the experimental pattern deviates from the one measured in the quench test. This can easily be explained by the existence of the

secondary collimators in the crosstalk Beam 1. Besides, in the benchmark Figure 3-7, it can be seen that the signal levels at the mirrored -120 m to -100 m are almost an order of magnitude higher. For this reason, when calculating the cost function, the BLMs located in this region are neglected due to crosstalk contribution.

Beam 1 6.5 TeV losses for 2015-2018

With the procedure already established for beam 2, but with benchmarked data only available for beam 2, it was decided to use the simulation results from beam 2 and taking advantage of the symmetry between the two beams (and the respective BLM positions) to reverse the results and utilise them for Beam 1.

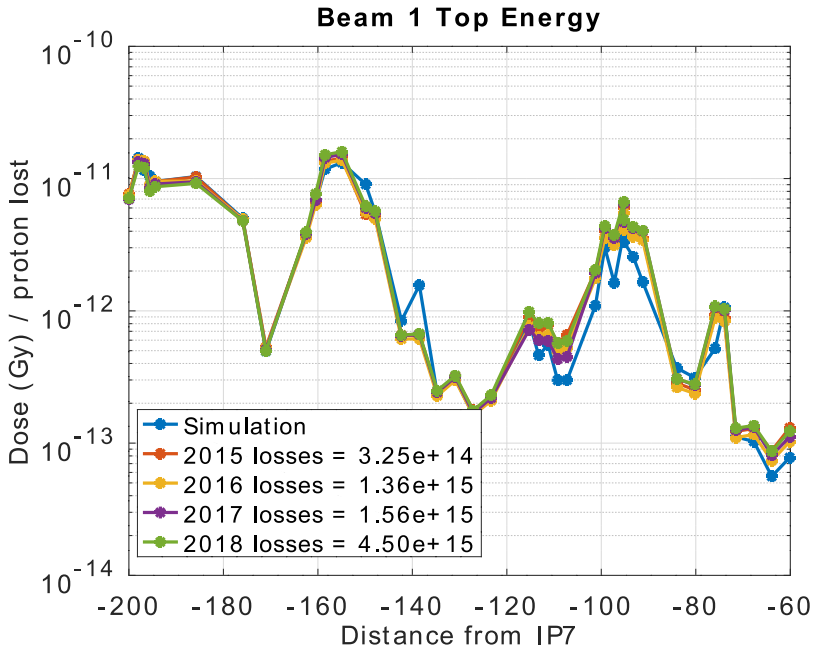

Figure 4-4: Comparison of simulated and measured BLM patterns (2015-2018) for Beam 1 proton losses at top energy (6.5 TeV). The simulated pattern includes the crosstalk from beam 2 for the BLMs between -120m to -100m. The measurements were divided by the number of protons lost in each year, determined in the Figure 4-5.

Therefore, in Figure 4-4, where the beam loss estimation is shown, the simulation line is not the product of a separate simulation study of beam 1 but the simulation study of beam 2 mirroring the location of the BLMs. Moreover, in order to further support the

argument made in the previous section, the simulated signals between -120 m and -100 m have both the crosstalk and direct signal incorporated in them. In other words, the dose per proton lost for these BLMs is the addition of the dose from both beams.

The agreement of the different year patterns and the simulation one seems to be even better than that of beam 2, even though no benchmark/experimental data were available. This is also reflected in the cost function assessment in Figure 4-5, where both the cost and the sharpness of the inverse peak is better than for the equivalent beam 2 function. This observation hints that beam 1, contrary to beam 2, seems to better follow the predictions (simulations) for a perfect machine, which suggests that Beam 1 is less affected by imperfections.

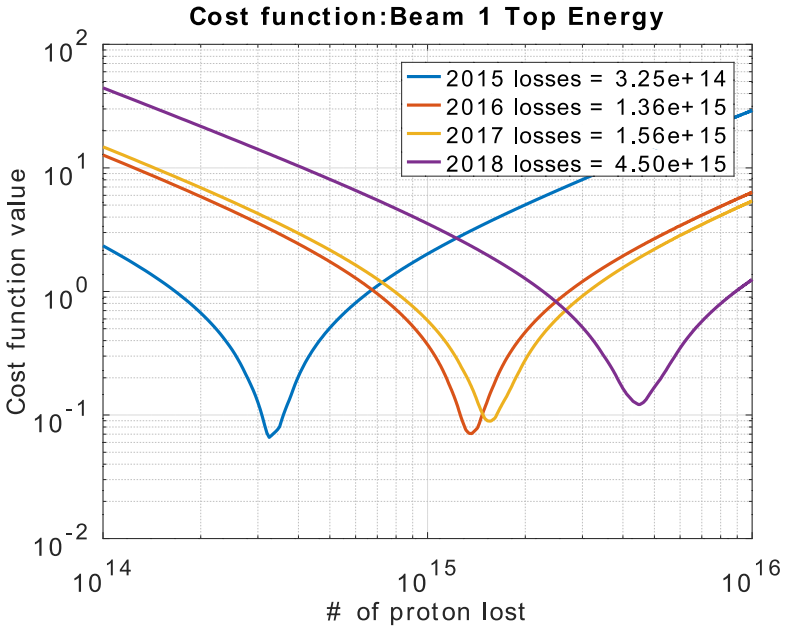

Figure 4-5: Cost function plot, evaluating losses of top energy (6.5 TeV) protons from Beam 1. The losses mentioned in the legend are the ones that bear the minimum fitting cost for each year.

Through these results, the thesis that beam 2 suffers from a possible misalignment of primary collimators is further supported.

4.3.2 Injection energy losses (450 GeV)

The vast majority of studies in the past focused on the impact of top energy (3.5 TeV, 4 TeV, 6.5 TeV and 7 TeV) protons in the LHC with 450 GeV not being studied as their effect would be diminished due to the energy difference. It was observed through the BLM measurements, disentangled by the beam mode (Table 4-1), that the dose to some regions of the IR7 was equally high to the one originating from top energy protons. For this reason, this section presents the study of the losses at injection energy, using the same methodology as described in Section 4.2.

Similar to top energy, the simulations for injection energy were carried out for beam 2 for 2015 collimation settings. Even though there are no benchmarks for injection energy, the simulations models and simulation chain are similar and hence the uncertainty is expected to be comparable to top energy. Consequently, the results are compared one to one and the fitting requested is absolute and does not take into account discrepancy factors that would otherwise be available, if a benchmark case was as well.

Beam 2 Injection proton losses for 2015-2018

Figure 4-6 shows the spatial BLM pattern for beam 2 at 450 GeV, with the cost function evaluation shown in Figure 4-7. Qualitatively it can be seen that the pattern looks different than the one for top energy protons, which can be explained by the different energy. We can see that the signals drop around an order of magnitude the further away we get from the source (beam 2 collimators at 200 m).

The pattern is consistent between the years, with a slight exception of 2016 losses on BLMs located between 150-160 meters. The simulated pattern also agrees remarkably well with the experimental data with the noticeable exceptions being the one BLM at 138 m and the underestimation in the BLMs between 100 and 120 meters. The reasoning behind these discrepancies is the same as those for the top energy. The single BLM discrepancy is attributed to a possible geometrical description error in the simulation model, and the multiple underestimated discrepancies, to the crosstalk shower coming from beam 1.

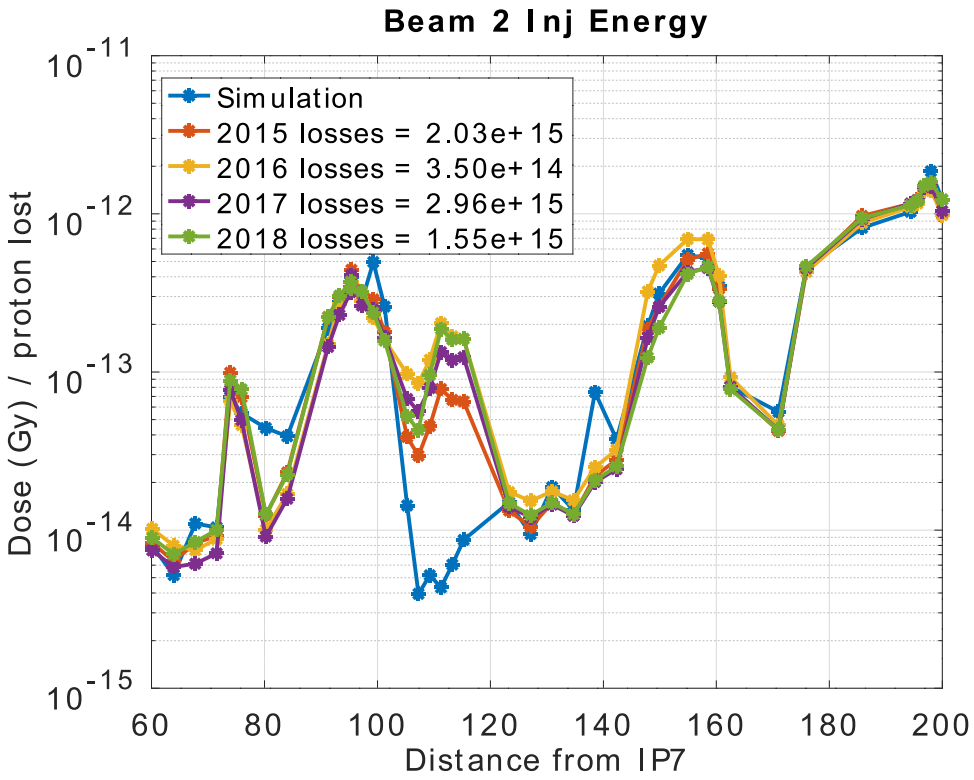

Figure 4-6: Comparison of simulated and measured BLM patterns (2015-2018) for Beam 2 proton losses at injection energy (450 GeV). The measurements were divided by the number of protons lost in each year, determined in Figure 4-7.

The cost function of the different years appears to be similarly performing and providing a very accurate match to the simulations. The year 2016 poses as a slight exception where the ratios of BLM signals between the primary collimators (200 m) and the quadrupole magnets (140-160 meters) change with respect to the simulation, increasing the possible error bar in the estimation.

Not surprisingly, since the experimental BLM data already suggested this, the injection proton losses are on par or higher in absolute numbers than the ones in top energy. This was expected because the per proton lost dose recorded by the BLMs is an order of magnitude lower at injection compared to the top energy precisely due to the difference in energy. Therefore, as can be seen in Figure 4-1, since the signals recorded were similar, at least in the primary collimators, one would expect a higher amount of absolute proton losses in order to reach similar cumulative doses.

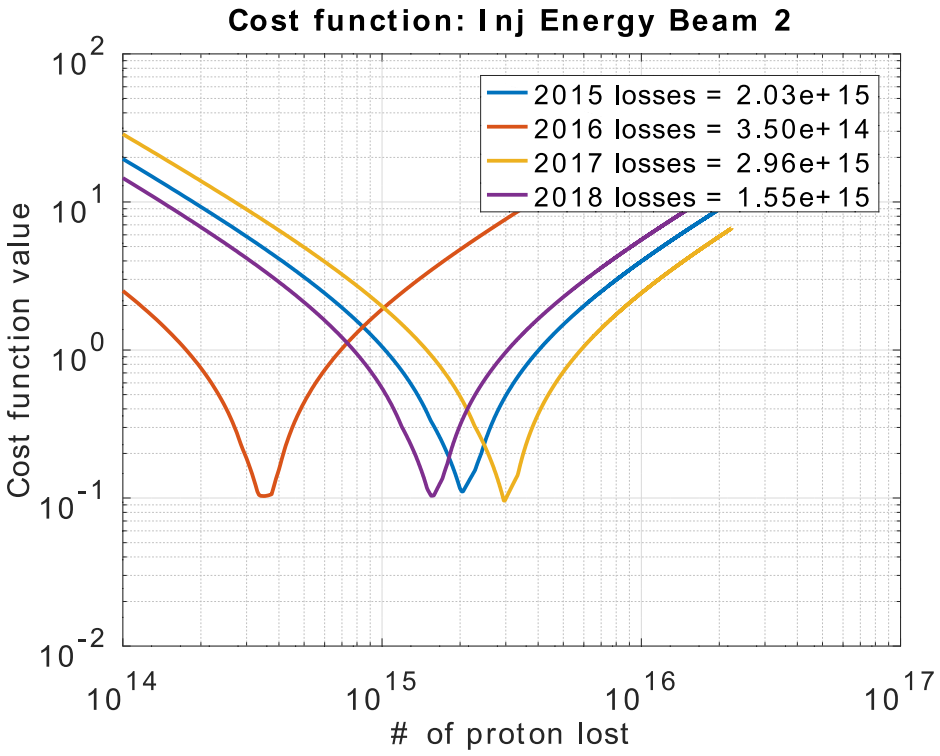

Figure 4-7: Cost function plot, evaluating losses for injection energy (450 GeV) protons in Beam 2. The losses mentioned in the legend are the ones that bear the minimum fitting cost for each year.

Beam 1 Injection proton losses for 2015-2018

As for the top energy, beam 1 was studied by mirroring the simulation results of beam 2, taking advantage of the symmetry between the two beams with respect to the IP7. The same qualitative remarks can be made for the loss evaluation maps for beam 1 injection energy shown in Figure 4-9, as for beam 2. At around -150 m there seems to be an anomaly in the data for 1 BLM in 2015 which likely originated from either a logging error or a BLM error that was fixed in the later years. Furthermore, the underestimation due to crosstalk persists, as expected, in the BLMs between -120 m and -100 m.

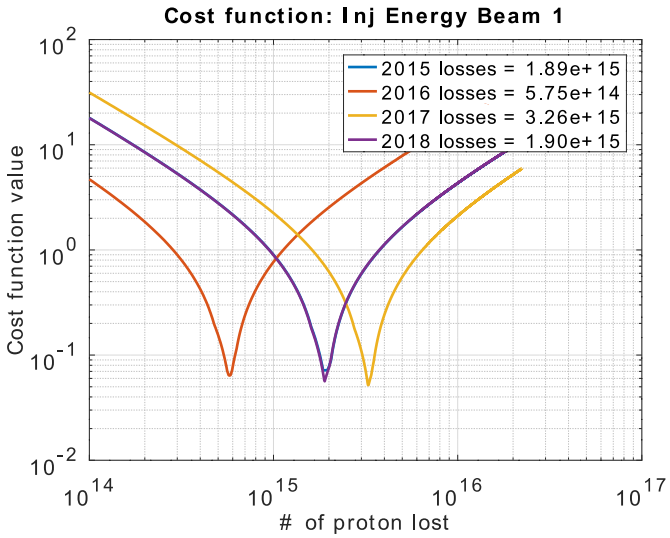

Figure 4-8: Cost function plot, evaluating losses for injection energy (450 GeV) protons in Beam 1. The losses mentioned in the legend are the ones that bear the minimum fitting cost for each year.

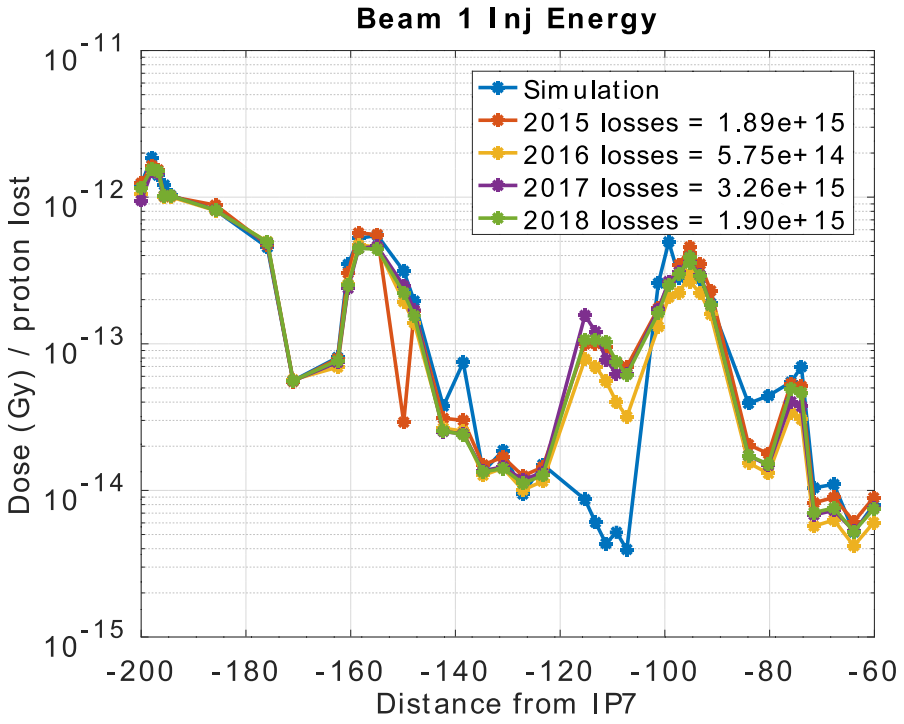

Figure 4-9: Comparison of simulated and measured BLM patterns (2015-2018) for Beam 1 proton losses at injection energy (450 GeV). The measurements were divided by the number of protons lost in each year, determined in Figure 4-8.

The BLM pattern appears to be more consistent between the different years as well as the simulations, a fact that is, in addition, reflected on the cost function evaluation graph shown in Figure 4-8. The fitting cost is less than 0.1 for all years, with the lines for the years 2015 and 2018 overlapping each other, being almost identical, and therefore hard to distinguish.

4.4 Benchmarking annual loss values against passive dosimeter measurements

In 2015, passive dosimeter holders were installed in the LHC, in order to systematically measure the ambient dose next to the critical elements of the machine. Radio Photo Luminescence (RPL) (62) dosimeters were placed inside the holders at the beginning of each year's run and at the same time, the RPL installed in the previous year were extracted for reading out the dose values. RPLs are small cylindrical shaped dosimeters (0.6 cm in length and 0.1 cm in diameter) that rely on the formation of stable colour centres in irradiated silver-activated aluminophosphate glass for measuring dose.

To provide an additional benchmark for the annual proton losses determined in the previous section, the expected dose in air was simulated, at the locations of the passive dosimeters that are installed right of IP7. Figure 4-10 shows a photograph of an RPL holder located at the separation dipole MBW (Magnet Bending Warm) return coil (top) and the equivalent FLUKA geometry (bottom). The RPLs were placed either at the front face, with respect to the respective beam direction, of the most impacted warm magnets, such as the warm dipoles and quadrupoles, or they were attached at some BLMs for experimental cross-validation.

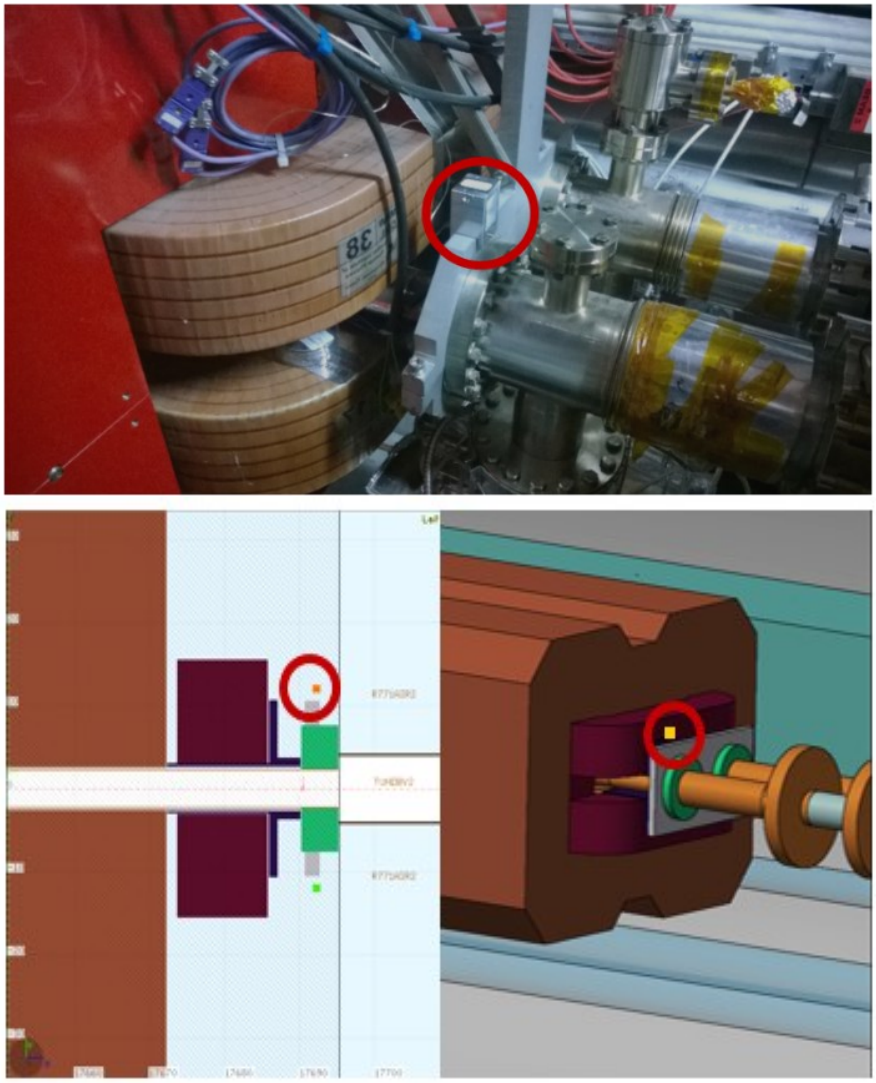

Figure 4-10: Picture of the return coil of a separation dipole (MBW) in IR7 with the RPL holder (encircled) (top), and the equivalent FLUKA geometry with the dose measured in one cubic centimetre in air (bottom).

Since RPLs are passive, the dose recorded is the cumulative dose from all sources of radiation in the respective year. Consequently, one cannot disentangle the contribution of beam losses according to beam energy or particle type (i.e. protons or Ions) as it is done with BLMs. To benchmark the simulations against the RPL measurements, the simulated prompt dose from 450 GeV and 6.5 TeV proton beams, is scaled according to the respective calculated proton losses (Section 4.3).

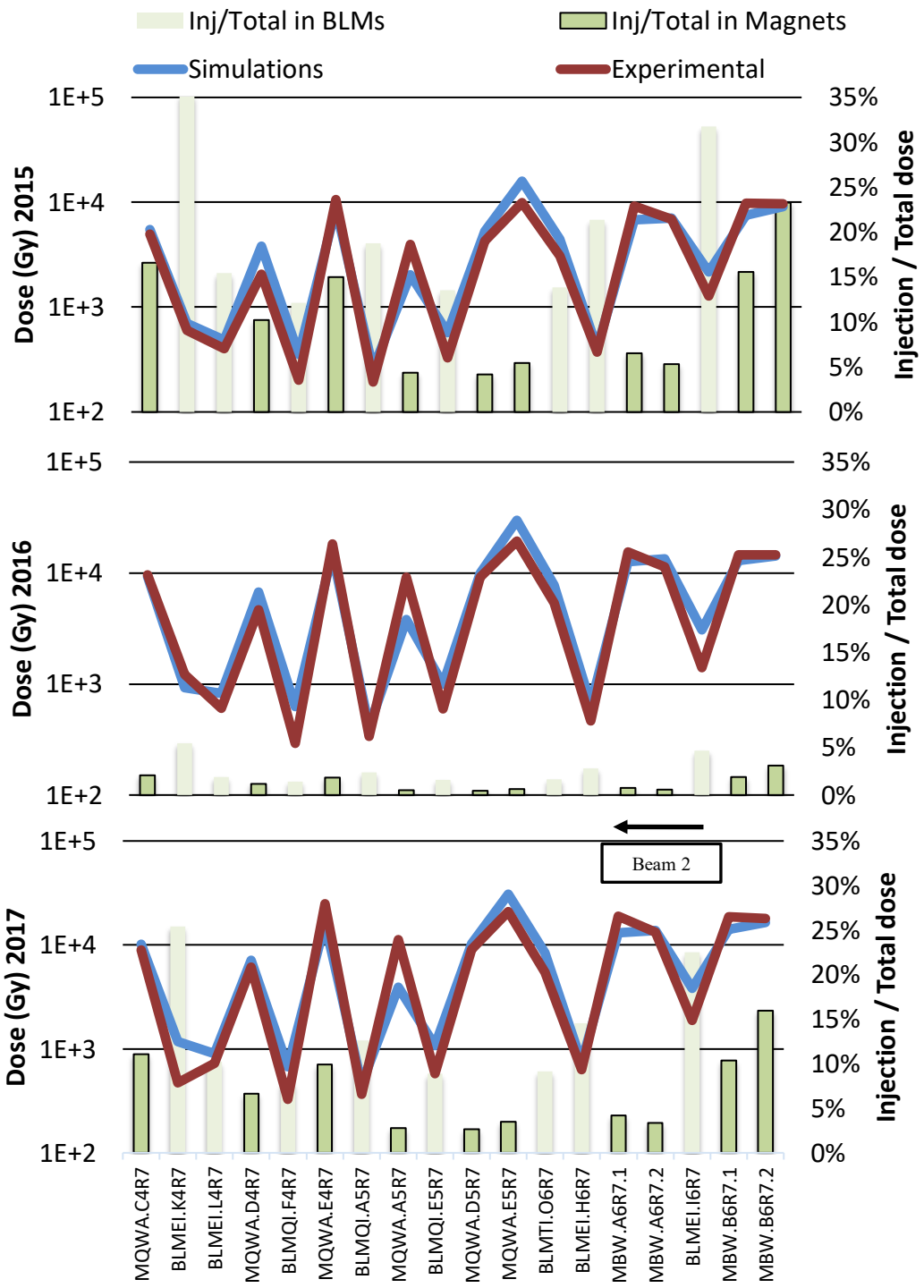

Figure 4-11: Comparison of RPL measurements and FLUKA simulated dose in air for the years 2015-2017 (left axis). Line thickness represents a 15% statistical and experimental error. Bar graph shows the % contributed from injection losses to total dose from simulations (right axis).

The total simulated annual dose for each of the dosimeters is divided by 0.95, to account for the average 5% contribution to losses while the beam is ramping in energy (Table 4-1), and then compared for each year. Furthermore, the majority of the dosimeters are placed at locations that are usually shielded from beam 1 showers; therefore, the crosstalk dose is considered negligible.

Figure 4-11 contains the measured and simulated dose for the 18 RPLs attached to accelerator elements, right of IP7, for the years 2015, 2016 and 2017 with the line thickness representing a 15% error in both simulations and measurements. The latter was measured by placing 3 passive dosimeters in the same holders in various locations. A general agreement within a factor of 2 is observed with signals spanning over 3 orders of magnitude with no systematic discrepancies observed. An excellent agreement is found for the RPL installed on the MBW return coils. On the other hand, looking at the location of the warm quadrupoles (MQW), a consistent overestimation of the dose in the RPL located in MQWA.E5R7 and an underestimation of the dose in MQWA.A5R7 is present in all years. These could be explained by geometrical discrepancies between reality and model as can be seen with the BLMs in the previous chapter.

When looking at the different contributions from injection and top energy protons (see bar graph in the figure), it can be seen that injection losses do not contribute significantly to long term dose in the warm magnets. In the year 2016, the dose from injection energy protons accounts only for a few percent. It is noteworthy that, even for years with high injection losses (2015 and 2017) the dose originating from injection protons accounts for less than 10% in most magnets with a maximum of 25% in the first MBW. However, that contribution is expected to be far less in the sensitive parts of the magnets that are shielded by tungsten masks, which are much more effective at injection energy levels (see Chapter 6).

Given the complexity of the simulation and the demanding accuracy required for the specific calculations (due to the small size of the RPLs), the agreement is generally very satisfactory. The benchmark provides extra confidence, in addition to BLM comparison, in the estimations of the long-term proton losses and provides additional feedback on the effect of injection losses in the sensitive accelerator equipment.

4.5 Loss scaling methods

This section introduces the old and new loss scaling techniques available for predicting collimation proton losses. The rational and performance of the two scaling methods based on the Run 2 operational period of the LHC is presented.

Losses overview and luminosity scaling

Table 4-2 summarizes the top energy proton losses in the different years for the two beams. As was already expected from the BLM signal levels, the years 2016 and 2017 are very similar in the number of losses while the losses were lower in the initial commissioning year (2015) and were higher in 2018 due to more aggressive operational settings. Furthermore, while in 2015 beam 1 losses were lower than beam 2, this was reversed for 2016 and 2017 while in 2018 the losses seem to be at the same level with beam 1 losses remaining a bit higher. The absolute number of protons lost in each year does not provide too much information unless they are considered in parallel with other measurable quantities to provide a reference point for the operational performance of the accelerator.

Table 4-2 also shows the achieved integrated luminosity in ATLAS and CMS for each year while the luminosity recorded by the other two experiments is omitted due to being significantly lower the two mentioned. It has been long assumed (63) that collimation losses were driven by luminosity due to elastic interactions of protons populating the beam halo and eventually being lost in the collimation system. Older scaling studies (63) assume that 1.15 10^{16} protons should be lost per 30 fb^{-1} (per beam) which would scale up to roughly 10^{18} protons lost for the target 3000 fb^{-1} for the HL-LHC (4).

Table 4-2: Loss evaluation overview for Top Energy protons (6.5 TeV) and integrated luminosity for ATLAS and CMS

	2015	**2016**	**2017**	**2018**
Beam 2 ($x10^{14}$)	5.8	12	11	42
Beam 1 ($x10^{14}$)	3.3	14	16	45
ATLAS (fb^{-1})	4.21	38.5	50.5	65.2
CMS (fb^{-1})	4.22	41.0	50.2	66.8

Table 4-3 shows the scaling factors that would occur if one normalises the estimated proton losses for each beam and each year with the respective integrated luminosity shown in Table 4-2. The estimated cumulative HL-LHC proton losses for the target 3000 fb^{-1} is also shown in the same table. One can immediately see that the expected number of total losses are about an order of magnitude lower than what was predicted in the past (1.15 10^{18}), and for each year and each beam, the numbers range between $0.6x10^{16}$ and $4.1x10^{17}$.

The large variation of the scaling factors led to the conclusion that other mechanisms than elastic collisions in the IPs are dominating the population of the beam halo and therefore the loss of particles in the collimation system. However, these driving mechanisms can be of different nature (e.g. electron clouds, small orbit drifts during the optics cycle) and it is hard to quantify their contribution to the total effect of the beam instabilities and halo re-population. Furthermore, as can be seen in the next chapter, luminosity scaling does not provide any insight into injection energy losses where collisions are not present.

Table 4-3: Top energy (6.5 TeV) losses scaling according to the average integrated luminosity of ATLAS and CMS

		2015	2016	2017	2018
Scaling factor (# protons / fb^{-1})	**Beam 2** ($x10^{13}$)	14	2.9	2.1	6.4
	Beam 1 ($x10^{13}$)	7.8	3.4	3.1	6.8
HL-LHC losses estimated for 3000 fb^{-1}	**Beam 2** ($x10^{17}$)	4.1	0.9	0.6	1.9
	Beam 1 ($x10^{17}$)	2.3	1.0	0.9	2.0

An overview of the injection energy proton losses in the different years for the two beams is presented in Table 4-4. The number of losses is comparable to the equivalent top energy losses with only the year 2018 showing a clear overhead of top energy losses compared to injection. Proton losses on the two beams are approximately equal, with beam 1 having slightly more. The year 2016 stands out as an exception, both because beam 1 has more losses than beam 2 but also due to the absolute number of losses being 5 to 10 times lower than the other years.

Table 4-4: Loss evaluation overview for injection energy protons (450 GeV) and integrated luminosity for ATLAS and CMS

	2015	2016	2017	2018
Beam 2 ($x10^{14}$)	20	3.5	30	16
Beam 1 ($x10^{14}$)	19	5.8	33	19
ATLAS (fb^{-1})	4.21	38.5	50.5	65.2
CMS (fb^{-1})	4.22	41.0	50.2	66.8

Even though it is evident that injection losses have no connection to integrated luminosity since collisions only happen at top energy, Table 4-4 also shows the achieved integrated luminosity in ATLAS and CMS for each year. At first glance,

this is especially noticeable for the years 2015 and 2018 where injection losses are at the same level, but the achieved luminosity is over an order of magnitude different.

For consistency reasons Table 4-5 shows the scaling factors that occur by normalising the estimated proton losses for each beam and each year with the respective integrated luminosity shown in Table 4-4. The estimated cumulative HL-LHC injection proton losses for the target 3000 fb^{-1} is also shown in the same table. It quickly becomes apparent that such scaling holds no grounds and is widely unpredictable between the years.

Table 4-5: Injection energy (450 GeV) losses scaling according to the average integrated luminosity of ATLAS and CMS

		2015	**2016**	**2017**	**2018**
Scaling factor (# protons / fb^{-1})	**Beam 2** ($x10^{13}$)	48	0.9	5.9	2.3
	Beam 1 ($x10^{13}$)	45	1.4	6.5	2.9
HL-LHC losses estimated for 3000 fb^{-1}	**Beam 2** ($x10^{17}$)	14	0.3	1.8	0.7
	Beam 1 ($x10^{17}$)	13	0.4	2.0	0.9

It can easily be seen that the relation between injection energy proton losses and integrated luminosity is, at best, weak and not helpful. In its place, there is a need of another scalable quantity that could provide more solid and repeatable results for both injection energy losses as well as top energy ones. The next chapter will try to introduce such a quantity based on the time-integrated intensity of protons circulating the machine.

New scaling quantity (time-integrated intensity)

As was presented in this chapter, the loss scaling with integrated luminosity is marginally useful for top energy protons and provides no insight for injection proton losses. Consequently, the need for a new measurable and scalable quantity arose. Since losses in the collimation system may be induced by different mechanisms, leading to beam diffusion, an empirical scaling approach is adopted based on the beam intensity. This scaling approach was first adopted within the CERN R2E project to make

predictions for the lifetime of equipment electronics. Using measurements from the LHC Beam Current Transformers (BCT), it is possible to determine how many protons are circulating the machine at all times by integrating the curve of the proton intensity over the circulation time as seen in Figure 4-12. The data are extracted analogously, as explained in Section 4.2.1, separating the information of each beam's intensity according to the beam mode. Consequently, it is possible to disentangle the integrated intensity for injection and top energy, offering better insight to both energies but especially for injection.

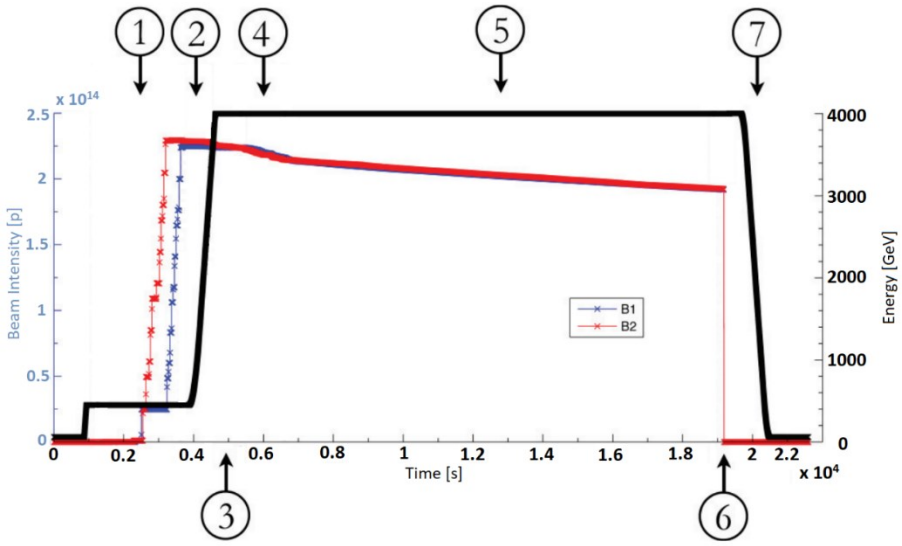

Figure 4-12: The LHC machine cycle, illustrated by the beam energy and beam intensities. There are seven stages: 1) injection; 2) ramp; 3) flat top; 4) squeeze; 5) stable beams; 6) beam dump; 7) ramp down (64).

The integrated intensity, measured in proton seconds (ps), for the years 2015-2018 for injection (450 GeV) protons are presented in Table 4-6. Contrary to the integrated luminosity shown in the previous section, the integrated intensity values are not very different from each other. This shows that the total time with beams circulating at injection energy from each year does not follow the luminosity that has been achieved. Furthermore, it is noteworthy that the two beams have almost identical integrated intensity values for each year with less than ten percent difference between them. In

the same table, new scaling factors are presented by dividing the number of injection protons lost, estimated in Section 4.3.2, by the measured integrated intensity.

Table 4-6: **450 GeV (injection) collimation loss** estimates, integrated intensity measurements and scaling factors for Beam 1 and Beam 2 in the years 2015 – 2018.

Year		2015	2016	2017	2018
Beam 1	Estimated # of protons lost	19×10^{14}	5.8×10^{14}	33×10^{14}	19×10^{14}
	Integrated intensity (ps)	8.54×10^{19}	7.09×10^{19}	14.5×10^{19}	10.6×10^{19}
	Scaling factor (#p lost / ps)	**22×10^{-6}**	**8.1×10^{-6}**	**22×10^{-6}**	**18×10^{-6}**
Beam 2	Estimated # of protons lost	20×10^{14}	3.5×10^{14}	30×10^{14}	16×10^{14}
	Integrated intensity (ps)	9.14×10^{19}	7.09×10^{19}	14.1×10^{19}	10.2×10^{19}
	Scaling factor (#p lost / ps)	**22×10^{-6}**	**4.9×10^{-6}**	**21×10^{-6}**	**15×10^{-6}**

It can be seen that the performance of the two beams does not significantly differ from each other. The scaling factors in the years 2015, 2017 and 2018 are very consistent with each other fluctuating only by a few ten percent showcasing the reproducibility of such a scaling method. On the other hand, the year 2016 appears to be an exception where the same integrated intensity implies almost a factor of 4 fewer losses for beam 2. One reason could be that in 2016, there was much less time spent in the so-called scrubbing period (65) which is a major source of injection energy proton losses. The full reasoning behind this discrepancy, however, is not entirely clear at this stage and deserves further future investigation.

Table 4-7: **6.5 TeV collimation loss** estimates, integrated intensity measurements and scaling factors for Beam 1 and Beam 2 in the years 2015 – 2018

Year		2015	2016	2017	2018
Beam 1	Estimated # of protons lost	3.3×10^{14}	14×10^{14}	16×10^{14}	45×10^{14}
	Integrated intensity (ps)	2.54×10^{20}	11.7×10^{20}	10.3×10^{20}	13.3×10^{20}
	Scaling factor (#p lost / ps)	**1.3×10^{-6}**	**1.2×10^{-6}**	**1.5×10^{-6}**	**3.4×10^{-6}**
Beam 2	Estimated # of protons lost	5.8×10^{14}	12×10^{14}	11×10^{14}	42×10^{14}
	Integrated intensity (ps)	2.50×10^{20}	12.0×10^{20}	10.7×10^{20}	13.8×10^{20}
	Scaling factor (#p lost / ps)	**2.3×10^{-6}**	**1.0×10^{-6}**	**1.0×10^{-6}**	**3.0×10^{-6}**

Table 4-7 contains the equivalent top energy proton results for the Run 2 years of operation. Once again, the integrated intensity values are similar for the two beams. The absolute values for all years are about an order of magnitude larger than the ones for injection. This might seem as counter-intuitive from the beam population point of view since top energy beams are less populated than injection ones due to proton losses that occur before and during the ramp. However, these losses are small compared to the total population of the beam. Furthermore, the beam spends a lot more time at top energy than injection as can be seen by a typical LHC cycle in Figure 4-12.

The integrated intensity scaling factors for top energy protons, presented in the same table, show an agreement within a factor of 2 between the two beams and the years 2015, 2016 and 2017. Beam 1 is exceptionally well represented by this method for these years and the normalized beam 2 losses decrease from 2015, where they were higher than beam 1, and remain the same for 2016 and 2017 a few ten percent lower than beam 1.

The operational year 2018 has a noticeable deviation compared to the previous years. The normalized losses are again similar between the two beams but about a factor of 2-3 higher than in previous years. This discrepancy was thoroughly studied by the R2E group at CERN (66) and it was shown that the operation of the machine in 2018 included a quasi-continuous crossing angle and β* levelling which resulted in increased beam losses mainly due to electron cloud build-up. The conclusion was that this beam operation strategy produced more luminosity and is, therefore, used as a reference for predicting beam losses in the HL-LHC era.

4.6 Conclusion

The previous sections established, based on the Run 2 experience, that collimation proton losses correlate much better with the time-integrated beam intensity than with the integrated luminosity. New predictions of betatron losses in HL-LHC, by using the new scaling factors derived in the previous section are presented as a summary in this chapter. Furthermore the estimates of the integrated intensity for the HL-LHC era based on the design specifications (67) are shown. Several assumptions based on the current experience in operating the LHC are taken into consideration.

Predictions of betatron collimation losses for the HL-LHC era

To begin with, for the proton physics years of 2016-2018, which are considered the first full years of exploitation of the LHC at almost the design energy, the average operational time was 150 days per year (68). The HL-LHC operational target is 160 days per year (69), available for p-p luminosity production. Assuming a 75% fault-free operation and 2 fills of 7 hours stable beams per day (5 hours turnaround) provides us with 1680 hours of circulating top energy beams per year of HL-LHC operation.

With a design value for the initial bunch intensity at top energy of 2.2×10^{11} protons and an assumed dump intensity of 0.8×10^{11} (to keep instantaneous luminosity at acceptable levels (67)) an average of 1.5×10^{11} ((2.2 + 0.8)/2) protons per bunch circulating the machine is considered. Using 2736 bunches, it is considered that $\sim 4.1 \times 10^{14}$ protons are, on average, circulating in the machine. This number assumes a

linear loss of intensity from all sources over the circulating time and, as seen in the previous section, losses at injection are considered negligible in the context of integrated intensity calculations. Lastly, expecting 12 years of HL-LHC operation, a time-integrated integrated intensity of ~$3x10^{22}$ ps is predicted per beam at 7 TeV for the full HL-LHC lifetime.

The usual time spent per fill, starting from the first injection until the ramp is around 25 minutes (Figure 4-12). About 10 minutes of those are spent filling up the LHC and therefore a linear increase to the $2.2x10^{11}$ protons is assumed, which is then kept stable for the remaining 15 minutes. Assuming the same number of fills, availability days etc. per year as for top energy this would mean that per year ~$2.4x10^{20}$ ps of integrated injection energy protons are expected. Comparing that to the ~$2.5x10^{21}$ ps of the top energy there is a presumed difference of around a factor of 10, which is actually very close to the average difference observed by the 2015-2018 data presented in section 4.5. Predictions made for injection energy could increase in the case of testing and scrubbing periods etc.

Table 4-8 summarises the results of the study presented in this chapter by presenting the final estimated number of proton losses for the full 12 year lifetime of the HL-LHC era. The calculations utilised the scaling factors from section 4.3 that yielded the most losses per integrated intensity, therefore representing the worst-case scenario in Run 2. In addition, a conservative safety factor of 3 is added to account for uncertainties in the whole procedure of estimating the proton losses, measuring the integrated intensity and assumptions on its HL-LHC final value. In addition, it cannot be excluded that the higher bunch intensity in HL-LHC leads to intrinsically higher losses.

The scaling factors can be intuitively used to calculate the loss rate given a certain number of protons circulating the machine. You can multiply with a given beam population at any point and easily calculate the number of proton losses you expect in the collimation system. For example, if you have $2x10^{11}$ top energy protons circulating the machine you can expect to have roughly $2x10^{6}$ lost protons/s in the collimation system by multiplying with the 10^{-5} scaling factor at top energy.

Table 4-8: Estimated # of betatron proton losses for the full HL-LHC (12 years) lifetime. The most conservative scaling factors from section 4.3 were used. A safety factor of 3 is applied on top of the scaling factors.

	Conservative scaling factor (#p lost / ps)	HL-LHC integrated Intensity (ps)	HL-LHC estimated # of protons lost (12 years)
Injection Energy	$3 \times 22 \times 10^{-6}$	3×10^{21}	Np_{450GeV} = **2×10^{17}**
Top energy	$3 \times 3.4 \times 10^{-6}$	3×10^{22}	Np_{7TeV} = **3×10^{17}**

The final numbers, Np_{450GeV} = **2×10^{17}** and Np_{7TeV} = **3×10^{17}** provide the basis for all the calculations presented in the next chapters involving long term damage studies and stand as the reference points for any future calculations/design studies.

Chapter 5 Radiation impact on collimators

In this chapter, the simulation results of short term (instantaneous < 1s) and long term (over several years, the expected HL-LHC lifetime) impact of radiation on the collimation system are presented. Before that, an introduction to the relevant radiation quantities and their possible effects is presented followed by the quantification of power deposition and radiation damage for current and HL-LHC collimator designs.

5.1 Introduction

Apart from the collimation system efficiency, the overall collimation system design also needs to account for radiation-related effects in collimator materials; these concern the collimator material robustness in case of high energy beam impacts and the collimation material degradation under several years of radiation exposure. The former poses a concern against high beam losses in a short period (short beam lifetime), typically lasting up to a few seconds before they are detected by the beam loss monitors which eventually trigger the beam dump. The latter is studied in the context of long-term irradiation and its effects on the degradation of the material properties such as electrical resistivity and thermomechanical properties.

Short term effects

In regular beam loss scenarios due to lifetime drops, the power deposition absorbed by the collimator jaws can be high enough to cause material deformation. The most severe cases can lead to either fragment ejection or plastic deformation, where the integrity and effectiveness of the collimator are jeopardised requiring them to be replaced. Nevertheless, even in cases were only elastic deformation can take place, the shape of the collimator could change in such a way that it produces a temporary arc

over the length of the jaw. This arc can cause a section of the collimator to be misaligned with the beam and eventually break the collimator hierarchy by intercepting part of the beam in an undesirable or unexpected way.

Long term effects

Long term irradiation of the accelerator equipment is of constant concern in the LHC. The collimators, in particular, being the elements closest to the beam, may experience property changes due to the degradation of material characteristics and radiation-induced ageing. For non-organic compounds of crystalline structure such as the materials used for collimators, the Displacements Per Atom (DPA) is used as a universal reference quantity to evaluate long term radiation damage. For example, a value of 0.1 DPA corresponds to an average 10% of the material nuclei being displaced from its lattice. The benefit of using DPA is that it provides a measure for microscopic defects in a way were the source of the radiation damage is irrelevant. This has the benefit of being able to compare the effects of radiation damage from different sources, for example, comparing the DPA originating from high energy protons in the LHC with that from low energy heavy ions used in irradiation campaigns. The downside is that DPA cannot be measured directly. Hence, one must rely on Monte Carlo simulations to evaluate and compare DPA for different cases.

Several irradiation campaigns have been carried out in the context of the HL-LHC project and other material science programs, such as EuCARD (70), EuCARD-2 (71) and ARIES (72), to test the effects of radiation on materials designed for high energy particle collimators. For example, at GSI Helmholtzzentrum (Germany), various material samples were irradiated using heavy and light ions reaching high levels of DPA in a small time frame. Several aspects were studied during the post-irradiation examination (73) such as changes in sample thermo-mechanical properties and electrical resistivity. For example, it was found that for values of the order 10^{-4} DPA in a molybdenum graphite composites the resistivity increased by up to a factor of 3 compared to non-irradiated samples.

Based on the estimated collimation losses derived in Chapter 3, this chapter will present the long term evaluation of DPA in absorber materials used in in the current

and future design of the LHC collimators. Making predictions of the expected cumulative DPA for the HL-LHC lifetime in the most exposed primary and secondary collimators, this study analyses the main physical processes contributing to the DPA and quantifies the spatial extent of the damage area. The results presented in this chapter are essential for establishing a relationship between the irradiation campaigns and the actual radiation environment in the LHC. This allows one to estimate the material degradation expected in future HL-LHC operation.

5.2 Energy deposition sharing in IR7

While collimators are the most exposed elements to the primary beam, a significant fraction of the impacting energy escapes in form of secondary particle showers and is eventually absorbed by the surrounding elements. An evaluation of the different energy sharing between important machine components is presented in this chapter, in an effort to identify machine hotspots and weak points as well as to quantify the beam impact on the different collimators. The settings and simulation setup of the 2015 proton quench test, as described in 3.2, were reused to evaluate the energy sharing for 6.5 TeV protons, which remains mostly unchanged when moving to 7 TeV.

Table 5-1 reports the percentage of the beam energy deposited in different machine components, air and the surrounding tunnel as seen in Figure 3-7. In total, the collimator jaws absorb only about 10% of the beam's energy. A large part is absorbed, by design, by the passive absorbers (TCAPs) placed as a radiation shield in front of most impacted sensitive equipment. For example, in the separation dipoles MBW.B6 and MBW.A6 where 4.7% and 3.6% of the energy is absorbed, and the first two warm quadrupoles (MQW.E and .D) of cell 5 and 4, which absorb 5.3% and 2.5% respectively.

As expected, the majority of the energy (33%) is deposited in the tunnel wall while the beam pipe, excluding the aperture inside the magnets, absorbs 9%, mainly due to its proximity to particle showers. Noteworthy, is also the 0.9% deposited in the surrounding air that contributes in the production of ozone molecules (74), which in

turn, unless properly studied and ventilated, greatly increase corrosion in the machine equipment. Lastly, only 93.5% of the beam energy is relevant to this study since the remainder either escapes the system in the form of neutrinos or is converted to mass.

Table 5-1: Sharing of beam energy deposition in IR7. Missing energy has been converted to mass or carried away by neutrinos.

Impacted element	**Beam energy deposition (%)**	**Impacted element**	**Beam energy deposition (%)**
Collimator jaws	9.4	MQWA.E4	2
Passive absorbers (TCAPs)	13	MQWA.D4	0.5
Collimator tanks/holders	5	Air	0.9
Beam pipe	9	Cold section	0.1
MBW.B6	4.7	Tunnel wall	33
MBW.A6	3.6	Other IR7 elements	6.4
MQWA.E5	3.8	**Total**	**93.5**
MQWA.D5	1.5	*Missing energy*	*6.5*

Figure 5-1 shows the energy deposition sharing between the collimators of the impacted beam 2 of IR7. The primary skew (TCP.B6R7) collimator and the immediate secondary after (TCSG.A6R7), are the most loaded ones in terms of energy deposition with 3% of the total beam energy being deposited on each. The impacted horizontal collimator (TCP.C), with 0.6%, plays the role of scattering the beam rather than absorbing it.

This plot gives a sense of the load sharing for the collimators in order to identify the weak spots. Different collimation settings could only slightly change this picture, as seen in the cumulative BLM dose comparison between the years 2015-2018 (Chapter 3). Consequently, the sharing is expected to follow with minimal changes with the collimation settings, as long as the hierarchy remains the same.

The above sharing concerns the total energy deposition, but one should not automatically assume there is a linear correlation with point-like quantities such as power density or DPA. Nevertheless, it is still expected that the highest peak DPA values occur in the most loaded collimators. Therefore, the rest of the studies in Chapter 5 will focus on these three collimators: TCP.C7, TCP.B7, TCSG.A6, the latter being the most upstream secondary collimator. Furthermore, even though most studies are done using Beam 2, by taking advantage of the symmetry between the two beams one can safely draw the same conclusions for beam 1.

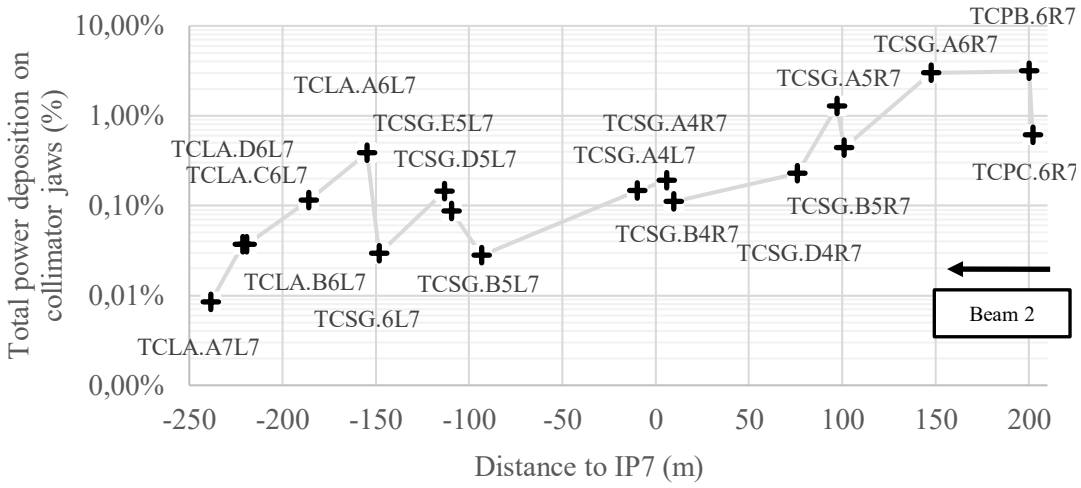

Figure 5-1: Energy sharing between IR7 beam 2 collimators during a horizontal loss scenario of beam 2, 6.5 TeV protons, with the 2015 collimation quench test settings.

The results presented above were obtained by assuming that the TCP and TCSG absorber blocks are made of CfC (AC150GPH). The energy deposition sharing will however change for the new MoGR collimators planned for HL-LHC. In this case, the load per collimator is expected to increase by roughly a factor of 3 for the specified collimator families. This conclusion is based on simulations considering the first three collimators only. The rest of IR7 was not included in this study due to the large computational time needed to simulate the entire insertion region as was described in 3.3.

5.3 Short term radiation impact on collimators

Throughout the duration of the thesis dissertation, numerous energy deposition maps were created for each type of collimator (primary, secondary and tertiary) deemed to be at risk or more exposed for a given scenario. These included either accidental scenarios or regular operation and, in both cases, the heat increase through the beam machine interactions was of interest. Figure 5-2 shows an example of the FLUKA model of the tertiary collimator (left). On the right of the same figure , the 3D absorbed dose map is shown overlaid on the geometry.

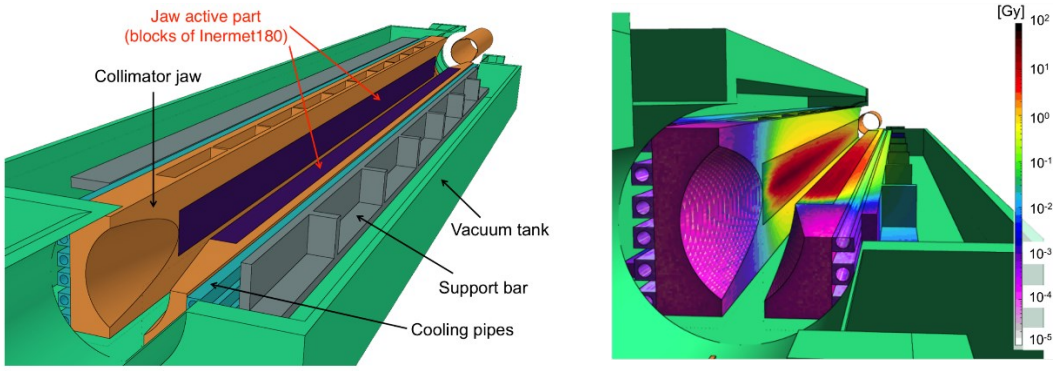

Figure 5-2: Tertiary collimator FLUKA model (left) and superimposed with an absorbed dose map (right) for an asynchronous beam dump scenario (75).

The various initial conditions of the impacted beam (accidental scenario, experimental studies, normal operation etc.) were defined and studied in collaboration with the CERN Accelerators & Beam Physics (ABP) and the Mechanical & Materials Engineering (MME) groups. The goal of the collaboration was to study the thermo-mechanical effects of the collimator jaws under the impact of high energy particle beams.

The generated maps are a prerequisite to the necessary thermomechanical studies that converted the energy deposition to a temperature increase map, on a given time frame, and study the deformation or the damage of the impacted jaws due to the generation of thermal stresses. A variety of outcomes may occur depending on distribution and time frame of the deposited energy for each case. For example, large amounts of very

concentrated losses (in the order of kW/cm^{-3}) will induce dynamic responses due to the restriction of thermal expansion by the material inertia. These, so called, thermal shocks, usually happen on the sub-second time scale and depending on the impact conditions and material properties (melting point, brittleness etc.) may lead to permanent damage of the collimators. At CERN, these scenarios are tackled by utilising advanced numerical tools, such as the wave propagation codes or hydrocodes. These are finite element analysis tools, e.g. AUTODYN (73), capable of handling cases where the physical properties of the materials undergo extensive changes.

These simulations were carried out by the MME group and some results are referenced here to provide context for the energy deposition studies that were performed during this thesis. While this procedure required the study of different collimator materials, designs and beam impact scenarios, the thesis will present the simulation chain capabilities with energy deposition levels for the present machine layout and the latest most updated specifications for the HL-LHC upgrade.

5.3.1 Study of the primary collimators

The current primary collimator design (TCP) described in Chapter 2 employs an effective jaw length of 60 cm made of CfC. This section will present the first ever study of the primary collimator under a realistic impact scenario of regular operation using both tracking and Monte Carlo simulations. The same technique of exchanging information between the two codes (Sixtrack and FLUKA), as explained in Chapter 2 and Chapter 3, as well as the same tracking and collimation settings as in 3.2.1 were used, with the exception of the proton energy which was increased to 7 TeV. Furthermore, nominal LHC beam intensities and a beam lifetime (BLT) of 0.2h were considered for these studies, corresponding to a proton loss rate of 4.5 x 10^{11} p/s. This translates roughly into 500 kW of power loss designed to be handled by the collimation system (16,76).

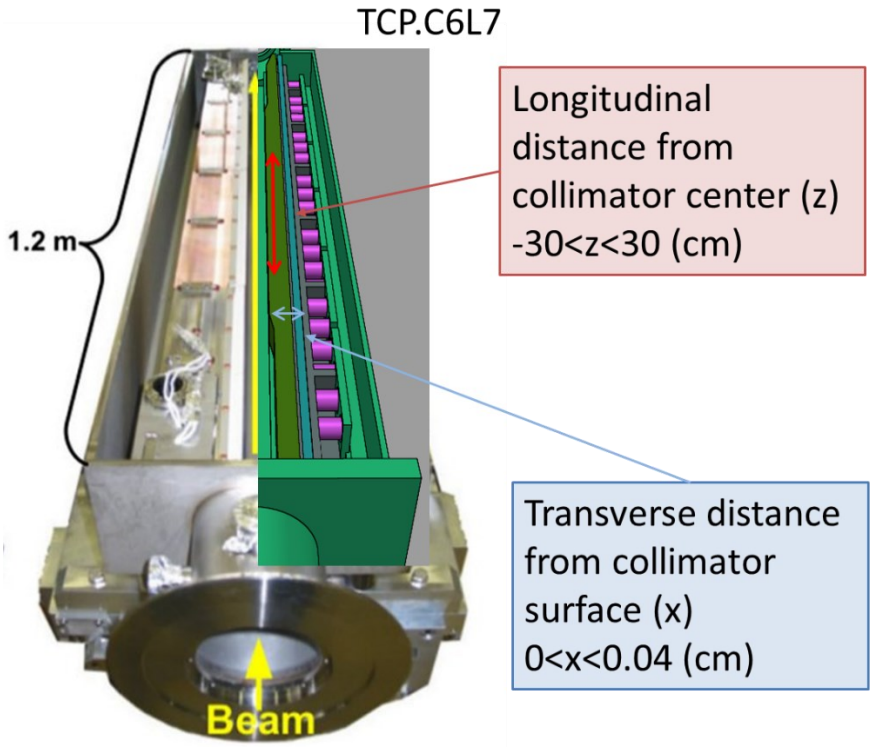

Figure 5-3: Photograph and FLUKA model of the primary collimator assembly (jaws and tank) with the relevant dimensional quantities illustrated.

The accurate extraction of the peak power density over the collimator longitudinal distance length requires a very small binning in the transversal plane (the X × Y × Z (Figure 5-3) bin size is 5×5×1000 μm^3). This comes as a result of the small initial impact parameter for betatron halo losses on the TCPs. Note that the first impacts, referring to protons that impact for the first time with the collimator, have an impact parameter of 5 μm. However, the overall distribution of proton impacts in the face of the collimator has a larger impact parameter due to the additional impacts of protons that have circulated the machine after the first impact.

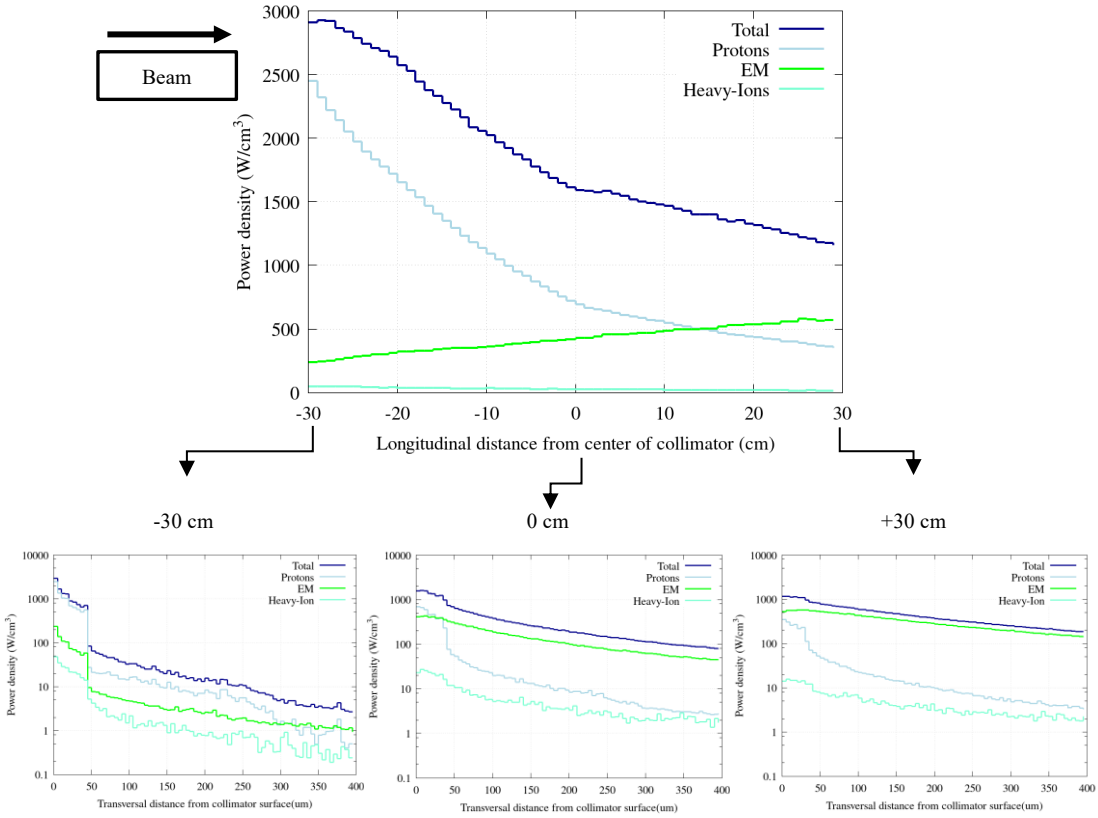

Figure 5-4: (Top) Peak power density over the length of the TCP.C6 for 7 TeV protons under a total power load of 500 kW, corresponding to 0.2h beam lifetime (BLT).
(Bottom) Transversal peak power density profiles in the cleaning plane at selected longitudinal locations.

Figure 5-4 (top) shows the peak power density profile over the 60 cm of active CfC material for the primary horizontal collimator under a horizontal loss scenario. By using specialised scoring routines, the power density due to individual particle types is shown in the same graph to provide further insight on the origin and type of losses. Transversal peak power density profiles are also shown in the bottom of the same figure for the beginning, the middle and the end of the collimator length with respect to the beam direction.

One can see that the peak power density in the upstream part of the jaw is dominated by the ionizing energy loss of the primary protons, reaching a maximum total of almost 3 kW/cm^3. However, transversally (in the cleaning plane) this power density is very

localised around the impact points of the fully energetic protons and drops rapidly deeper than 50 μm from the surface.

In the centre of the collimator (z=0) the transversal profile shows signs of equilibrium between the energy density originating from the surviving highly energetic protons and the secondary products of inelastic interactions which initiate electromagnetic and hadronic showers. It is apparent that the hadronic and electromagnetic showers spread the deposited energy a lot further transversely in the collimator material due to the scattering of the electrons and photons.

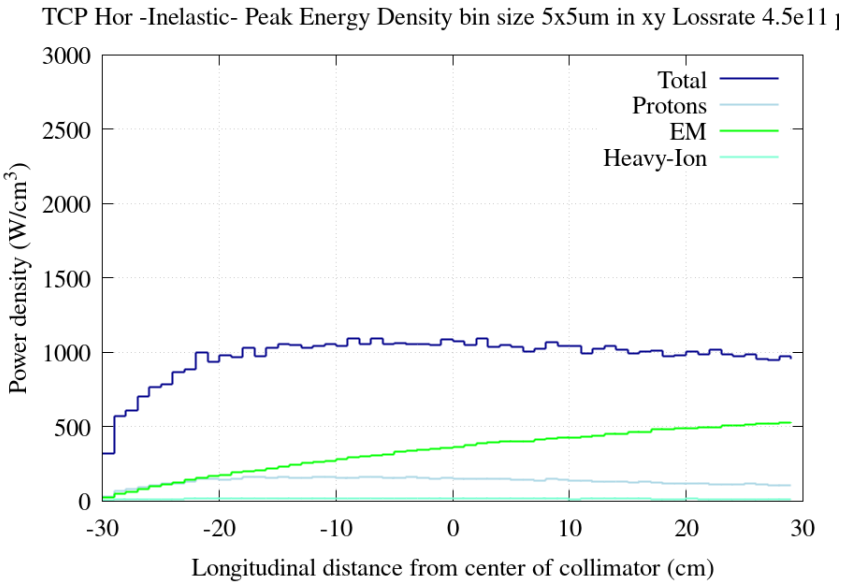

Figure 5-5: Peak power density over the length of the TCP.C6 induced by the inelastic interaction products of 7 TeV protons under a total power load of 500 kW corresponding to 0.2h BLT

At the downstream end of the collimator, the peak value of 1 kW/cm^3 is only a factor of 2-5 higher than the energy density accumulated further from the collimator surface due to the EM showers.

Preliminary studies utilising only the inelastic interaction locations as a source for the FLUKA simulations were utilised in order to disentangle the contribution of the inelastic interaction products from the contribution of primary protons. Figure 5-5 is the equivalent plot to Figure 5-4 but the energy deposition originates only from the inelastic interaction products of the original fully energetic protons. In this plot, the

additional contribution missing in order to reach the total comes from the pion build up that eventually decays into electromagnetic showers. The EM curve is almost identical to the one shown in the Figure 5-4 since EM showers are mostly coupled to the hadronic showers through the pion decay.

The maximum values of 3 kW/cm^3 are not significantly higher than previous estimations of around 2 kW/cm^3 (Chapter 18 of (1)). The main difference is that in the older studies, non-realistic parallel proton impacts in the collimator jaws were considered without the use of the more advanced impact distribution that takes into account multi-turn effects using tracking codes. These new results with a very pronounced energy density inducing high temperature gradients, could lead to thermal stresses that were not previously considered. New thermo-mechanical studies may be needed, however due to the small size of the bins and the large size of the collimator, this is not a trivial task. Moreover, the small size of the impacted area could mean a fast heat dissipation, which can reduce the peak temperature.

HL-LHC considerations

For the upcoming HL-LHC upgrade, an exchange of the AC150GPH CfC active jaw blocks of the primary collimators with blocks made out of Molybdenum Graphite (MoGR) is considered. To this end, peak power deposition studies were made with different materials for both the primary horizontal (TCP.C) as well as the primary skew (TCP.B) collimators. Important to note here is that the comparison between the two materials is done using the LHC maximum loss rate. In the HL-LHC era the maximum loss rate for the same 0.2 hours beam lifetime would be nearly double due to the higher beam population. Figure 5-6 shows the peak power density profile in the TCP.C in both materials, showing a peak increase of a factor of 2 using the 5x5 μm^2 binning. In order to provide a more intuitive comparison of the gradient of the energy deposition, the peak power density profile over a larger cross-sectional binning of 400x400 μm^2 is also shown on the same graph for the primary collimator in the two materials.

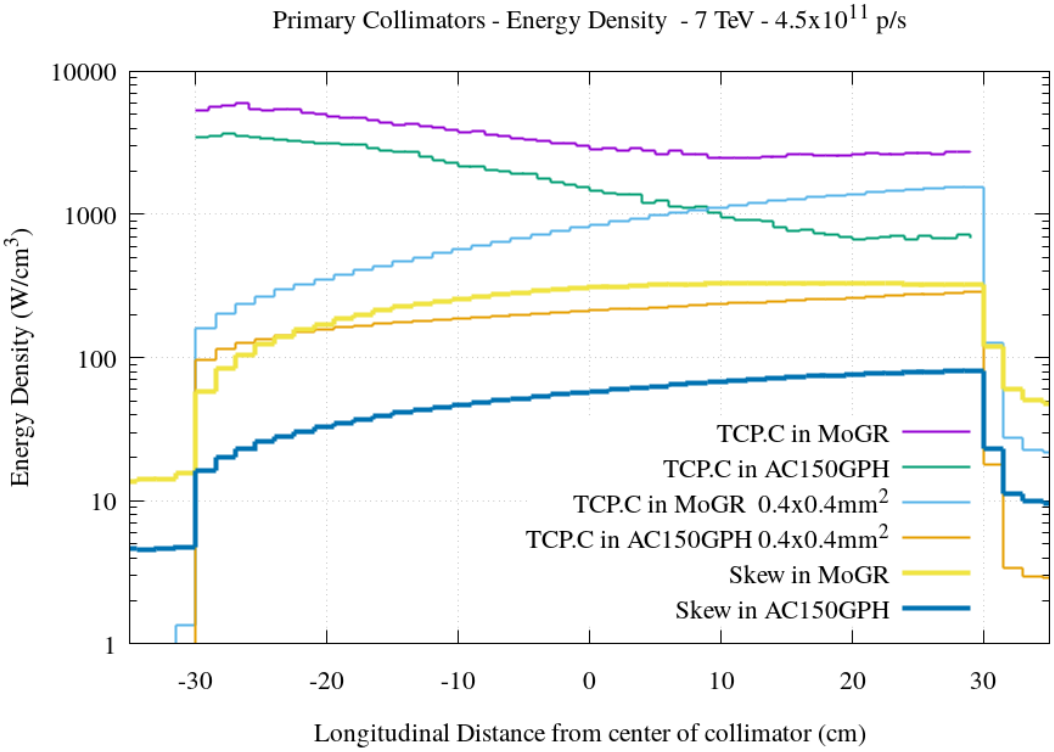

Figure 5-6: Longitudinal peak power density distribution over the primary collimator length for 7 TeV protons under a total power load of 500 kW corresponding to 0.2h BLT.

When comparing the two graphs with the different bin sizes, it becomes easily apparent that close to the impact point the total energy deposition is not significant but very dense at the impact point. However, at the far end of the collimator (+30 cm) the averaged out plot (400x400 μm^2 binning) being within a factor of 2 lower than the peak (5x5 μm^2 binning) shows that the energy gradient is diminishing along z. Moreover, the MoGR case has now over a factor of 5 higher than the graphite case.

Doubling as a summary plot, the peak power density profile for the skew primary collimator is also shown in Figure 5-6. While the total power deposited on the whole jaw is significantly higher than in the horizontal one (Figure 5-1) the peak power density profile is significantly lower than in the primary, even when the larger bin size is considered. The large bin size was used for the skew collimator without a need for a smaller one due to the mostly low gradient power density map in the skew collimator. Primary proton impacts on the skew collimator itself are minimal compared to the

deposition from upstream showers escaping from the horizontal collimator and impacting here. As a result, the main contributors to the skew collimator's energy deposition budget are the EM showers.

5.3.2 Study of the most impacted secondary collimator

Robustness studies of the most impacted secondary collimator, the TCSG.A6, as it is shown in Figure 5-1, have been carried out through a joint effort from multiple CERN teams. Similar to the primary collimator case, tracking simulations preceded the energy deposition ones that were used as input for the finite element analysis studies. While in the primary collimator case the collimator gaps made little difference to the end result, in this case, the retraction between primary and secondary directly affects the load on the secondary collimator.

As it was seen in Chapter 3, different settings do not have a dramatic effect (more than an order of magnitude), but rather differences within a factor of 2-3 are expected. Nevertheless, both the LHC settings of 2 sigma retraction between the primary and the secondary, as well as the HL-LHC case of 1 and 2 sigma retraction for CfC and MoGR blocks, respectively, were studied. Furthermore, the upcoming replacement of the TCSP jaws with TCSPM (Figure 5-7), that changes the tapering design to further reduce impedance, were also studied to establish that both jaws satisfy the operational specifications. In the case of secondary collimators, the bending of the collimator due to the thermal load has the added drawback of breaking the collimation hierarchy. For this reason, it is important to study, first of all, whether the stresses are high enough to induce plastic deformation or permanent damage to the collimator and if not, whether the elastic deformation would cause a hierarchy disruption. This secondary effect is highly undesirable since it may lead to primary fully energetic protons directly impacting the secondary collimator, greatly reducing the collimation efficiency and risking the protection of SC magnets.

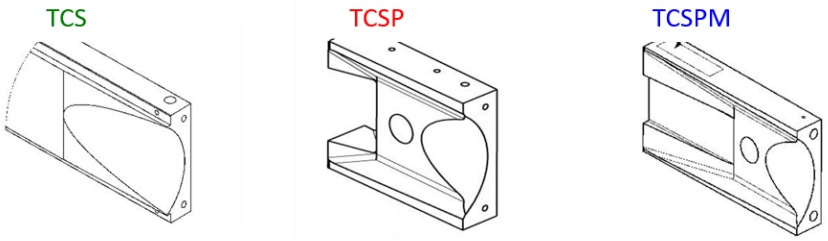

Figure 5-7: Different secondary collimator jaw tapering designs considered for the HL-LHC (77).

Taking advantage of the symmetry between the two beams, only Beam 1 was studied. Moreover, only the collimator jaws, tanks and the dogleg warm magnets were modelled in the FLUKA setup in order to save CPU time. In addition, the energy deposition in the secondary collimators seems to be minimally affected by the material on the primary. The binning of the energy deposition scoring was chosen in such a way that the created 3D energy deposition maps could be later used as input for the ANSYS calculations of the thermomechanical studies. This meant that in cases where higher geometrical detail was required, e.g. the jaw taperings, extra finer meshes were used even though the energy deposition gradient did not demand it.

Figure 5-8 shows the peak power density profile for the TCSP model over the active absorber part of the jaw in CfC (left) and in MoGR (right). On the same graph, contributions of different particle types are shown. In contrast to the primary collimators, the peak energy density profile is not determined by the ionizing energy loss of primary protons but by electromagnetic. The main difference lies in the more spread out proton impact distribution on the secondary collimator originating from the diffractive protons escaping the primary. The upstream showers are also visible in the first 40 cm for the graphite block and the first 15 cm of the MoGR where an “abnormal” bump can be seen that is then dissipated and taken over by the EM shower development that originates from the proton inelastic interaction.

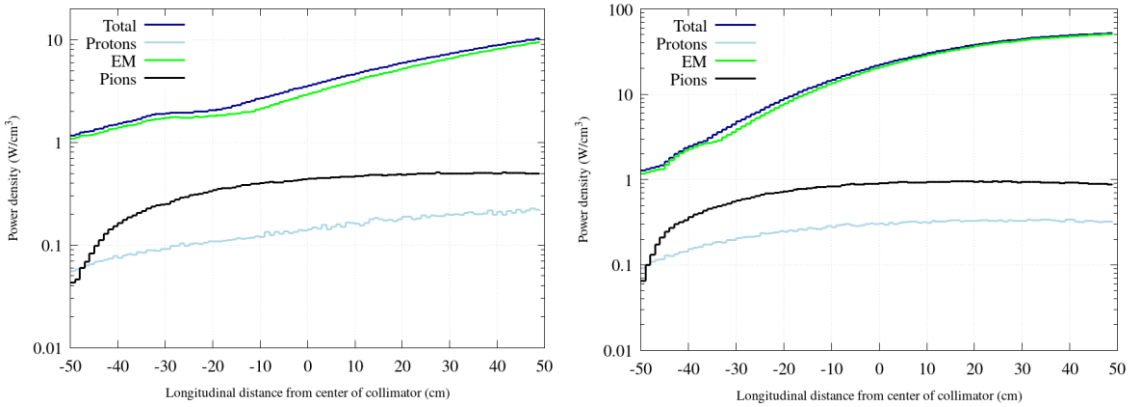

Figure 5-8: Peak power density profiles over the active TCSG blocks in AC150GPH (left) and MoGR (right) for 7 TeV, 1h BLT, 2 sigma retraction.

Looking at the deposition at z = +10 cm for the graphite case, the value of 5 W/cm^3 can be intuitively compared to the EM component of the proton case of Figure 5-4. This is done by scaling the value of 500 W/cm^3 found there, with the 10^{-2} ratio of inelastic interaction between the primary and secondary collimator that can be seen in the loss map of Figure 3-5. The maximum power density of 10 W/cm^3 reached for the graphite case is an effect of the longer absorber block of 1 m compared to the primary 60 cm. The shorter inelastic interaction and radiation length of the MoGR is the main reason that, with all other settings being the same, the peak is increased by a factor of 5 up to 50 W/cm^3.

Figure 5-9 shows a two dimensional cross-section (x, y) of the 3D map at the peak energy density location along the z direction (Figure 5-3). The collimator jaws are shown with respect to the beam reference system with the beam impact and distribution visualised by the non-symmetric losses with respect to each individual jaw. The energy deposition is shown in GeV/cm^3 per proton lost in the collimation system and high values can be seen also outside the active absorber block. These maps are suitable for ANSYS calculations since they can be easily scaled to the desired loss rate for either the 0.2h BLT of the LHC (4.5 x 10^{11} p/s) or of the HL-LHC (8.34 × 10^{11} p/s).

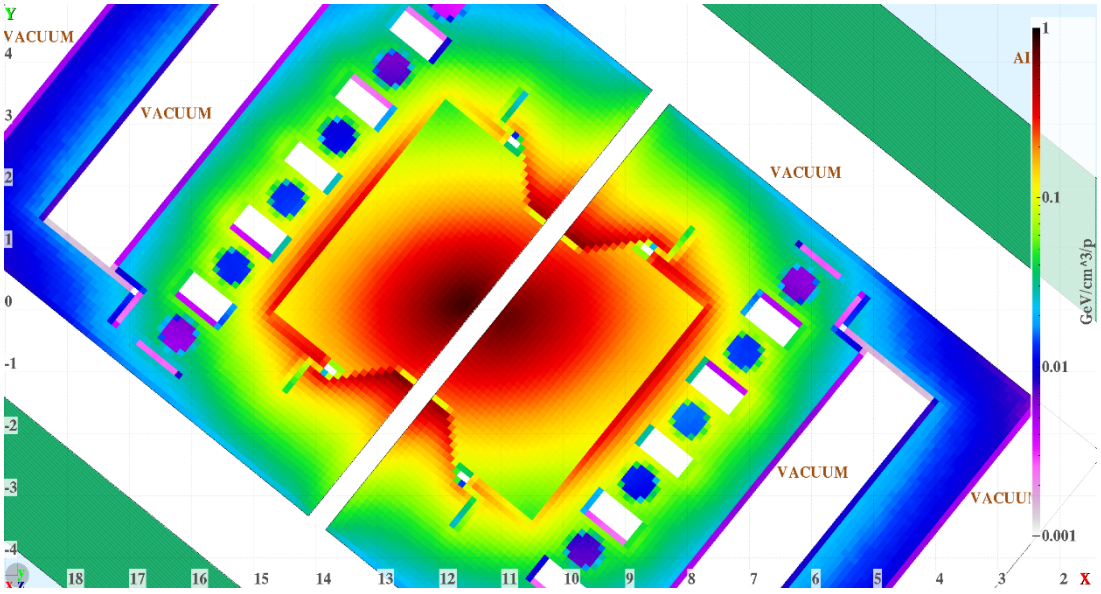

Figure 5-9: Transverse (x, y) cross-section at +50 cm in the Z direction of the energy deposition map on the TCSG.A6R7 with MoGR absorber blocks, 7 TeV protons and HL-LHC settings.

Figure 5-10 shows a sample of the finite element analysis results for the TCSPM jaw in MoGR under a 0.2h BLT of HL-LHC beam (~940 kW) and 2 sigma retraction. On the left side, the maximum temperatures reached on the collimator jaw are shown, under that load for a duration of 10 seconds according to the operational design parameters (67). After the stress test validated that no plastic effects occur, the right side shows the maximum elastic deformations caused by the impacted thermal load, on top of the deformation added by self-weight and assumed tolerances. While this is the most severe situation, it is shown that the maximum deformation is of the order of 500 μm which is enough to break the hierarchy.

Table 5-2 shows an overview of the simulation chain results for all the different cases including the present and the future secondary collimator design. It summarises the total power absorbed by the most impacted jaw assembly, its absorber block, as well as the collimator assembly as whole, including both jaws plus the tank. The two BLT cases of 1h and 0.2h are considered, with the one basically being a scale of the other by the ratio of proton losses per second. For the LHC case, the total power deposited in the TCSP agree with the previous estimation of 3% of the total impacted power, presented in Figure 5-1. Changing to 1 sigma retraction and keeping the absorber block

in CfC, increases the load on the collimator overall by a factor of 2-3. Lastly, changing the absorber block material to MoGR increases the total power absorbed by a factor of 10 while the collimator jaws and assembly are burdened by an extra factor of 5.

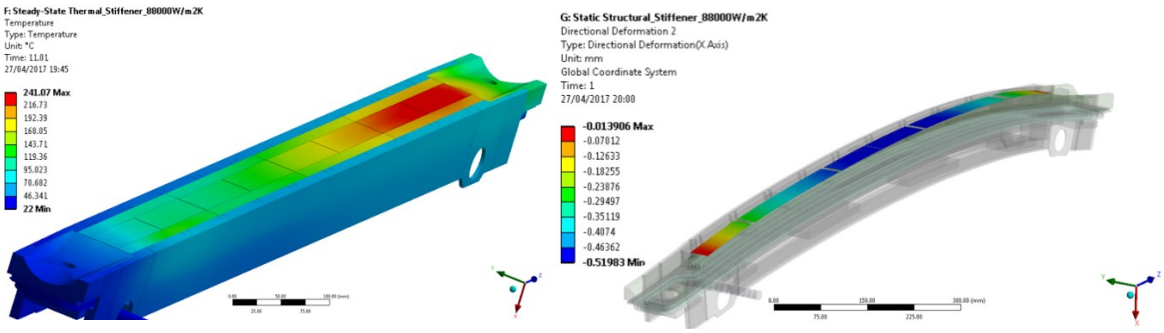

Figure 5-10: Temperature map (left) and total directional deformation (right) of the TCSPM in MoGR 7 TeV protons, 0.2 h BLT (940 kW total power), HL-LHC settings (78))

On the FEA simulations side, all scenarios appear to handle stresses without any permanent plastic effects. However, the specification of a maximum of 100 μm sagitta allowed for nominal usage scenarios (78,79), is not satisfied for 1 sigma retraction cases as well as the 0.2h BLT MoGR case. Even though the 1h BLT 1 sigma case can easily be rectified with some minor tweaks in the jaw design, the large differences for the 0.2h BLT, (a factor of 3 for 1 sigma retraction and a factor of 5 for the MoGR) question the suitability of this new design on this specific role. Follow up studies are planned to address these issues.

Table 5-2: Total energy deposition loads on the new secondary collimator designs of TCSP and TCSPM at the TCSG.A6 positions of IR7 for current LHC and future HL-LHC upgrade scenarios (Last row) Total sagitta of the directional deformation (thermal + self-weight + tolerances) (80)

	Total Energy deposition (kW) https://indico.cern.ch/event/676105/					
	1h BLT (188 kW)			0.2h BLT (940 kW)		
	$TCSP_{CFC}$ (LHC)	***$TCSPM_{CFC}$ (HL-LHC)***	***$TCSPM_{MoGr}$ (HL-LHC)***	***$TCSP_{CFC}$ (LHC)***	***$TCSPM_{CFC}$ (HL-LHC)***	***$TCSPM_{MoGr}$ (HL-LHC)***
Retraction (σ)	*2*	*1*	*2*	*2*	*1*	*2*
Most loaded jaw	2	5.5	9.4	10	27.5	46.9
Absorber of most loaded jaw	0.4	1.5	4	2	7.5	20
Both jaws + Tank	**5.5**	**12.6**	**20.7**	**22.5**	**63**	**103.5**
Total sagitta (um)(REF)	**83**	**110**	**86**	**96**	**300**	**505**

Lastly, on the FLUKA simulations side the energy density on the proposed 1 μm thick molybdenum coating (81) was studied. The coating is suggested as an alternative way to reduce impedance, without further increasing the material density (e.g. changing the absorber block to Cu). Figure 5-11 shows the 3D power deposition map for 1h BLT for an LHC beam with the MoGR block coated with pure molybdenum. On the same plot the equivalent 1D peak power density on both the coating as well as the rest of the assembly is shown.

Due to the higher density of Molybdenum the maximum power density is increased by a factor of 3, reaching 150 W/cm^3 compared to the 50 W/cm^3 reached in the absorber block. Noteworthy is the fact that large values of power density are also reached outside the absorber block, especially in the block housing that is made out of the dense Glidcop. One can see high values being reached at the beginning of the collimator that is mainly impacted by upstream showers.

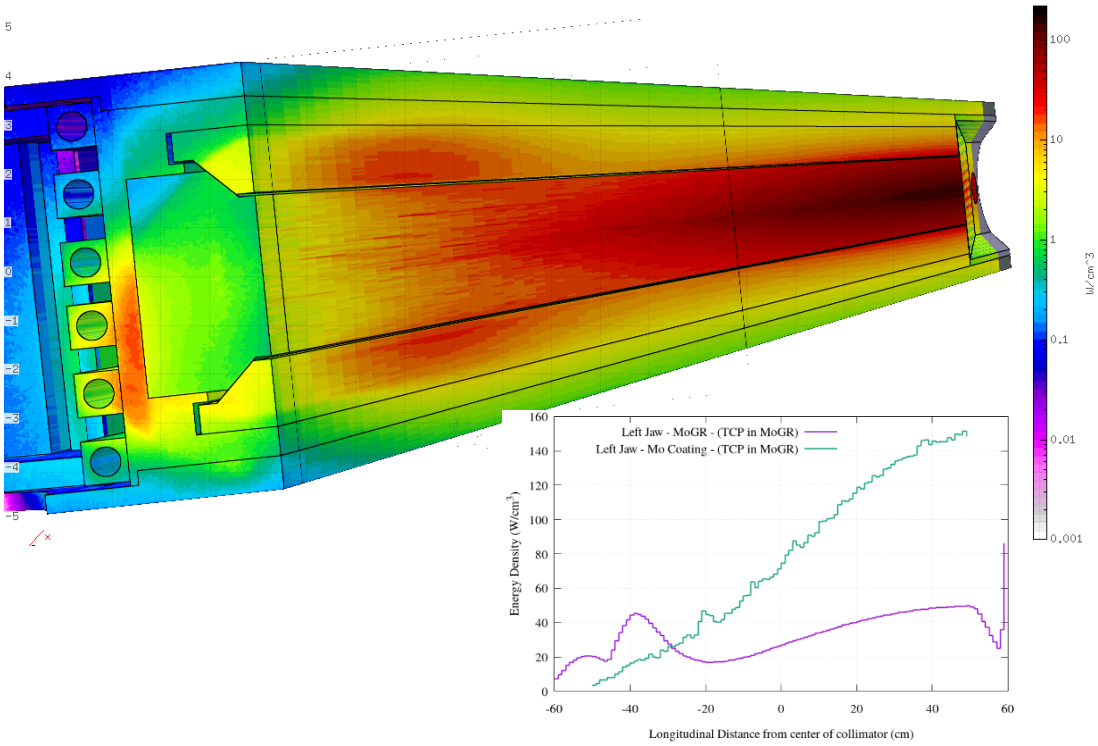

Figure 5-11: (top) 3D power deposition map on the most impacted TCSPM jaw with a Molybdenum coating. 7 TeV protons, 0.2 h BLT (500 kW total power), LHC settings.
(bottom) 1D peak power density over the jaw length, same collimator and settings.

5.4 Long-term displacement damage on collimator absorber blocks

This section aims to quantify the peak Displacements per Atom (DPA) in the most impacted primary and secondary collimators, considering the presently used absorber material (CfC) and the one considered for HL-LHC (MoGR). Moreover, the contribution of primary protons and secondary particles (e.g. Recoiling nuclei, inelastic interaction products etc.) to DPA is disentangled. The values for DPA presented in the plots are evaluated for an assumed total proton losses of 10^{17} for the full HL-LHC lifetime, while the final summary table takes into account the conservative safety factor of three as presented in Chapter 4.

5.4.1 Setup for calculating DPA in the collimator jaws

In order to quantify the consequences of long-term presence of materials in a mixed radiation environment, it is essential to be able to predict the lattice damage under irradiation. FLUKA requires as input from the user the average minimum energy, over all crystallographic directions, necessary to produce a defect also known as the threshold displacement energy (E_{th}). This value depends on the material and in this study we adopted the ones typical used by the NJOY code (82) which is also employed by FLUKA in several calculation steps.

For the collimator materials used in the current design (AC150GPH) and planned for the HL-LHC upgrade (MoGR), the threshold energy of graphite, $E_{th\ (gph)} = 35$ eV, was used. In addition, estimates for the considered pure molybdenum coating of the secondary collimators are provided, adopting a threshold energy of $E_{th\ (Mo)} = 60$ eV. By definition, this approach does not take into consideration the various differences in induced DPA depending on the crystallographic direction which in reality might reduce or increase the final DPA values. Lastly, the code calculates DPA by utilising a modified Kinchin-Pease damage model and taking into account the effect on the displacement efficiency for higher recoil energies due to recombination and migration of the Frenkel pairs (83).

In order to estimate the displacement damage in the absorber blocks, a detailed account of physical interactions is required to fully simulate the microscopic defects induced by the secondary particles generated in the hadronic and electromagnetic cascades and the recoiling heavy nuclei. Consequently, the same physical processes had to be enabled as for the heavy ion study reported in section 3.5. Furthermore, relatively low particle thresholds were required. In this study, the precision default values of general particle transport thresholds of 100 keV were adopted, with the exception of electrons (500 keV) and neutrons (10^{-5} eV). These values were chosen after a series of tests with various thresholds (lower and higher), comparing the total DPA obtained from particles above and below threshold. The selected thresholds offered the best compromise between CPU time and accuracy, with a minimal penalty due to the use of less accurate physical models below transport threshold.

In addition, the disentangling of the contribution to DPA of the different families of particles for both primaries and secondary collimators is also presented. These studies, however, required a much lower threshold of 1 keV for general particle transport to accurately explore each particle's contribution to DPA. These kind of low thresholds made the simultaneous study of both the primary and first secondary collimators impractical and a similar two step simulation technique as for cold section simulations Chapter 3 had to be adopted to explore the DPA the TCSG.A6.

Injection energy protons were also studied and found that, per proton lost, they induce a factor of 2 less peak DPA in the primary horizontal collimator and a factor of 10 less in the primary skew and the most impacted secondary. Consequently, it is expected that in the worst case scenario they should contribute by less than a factor of 2 in the peak DPA in the primary impacted collimator (e.g. the horizontal). On the skew and most impacted secondary their contribution should not surpass 10% to the peak DPA. Both cases should be masked by the safety margin that was adopted for the prediction of HL-LHC top energy losses. Therefore, a detailed analysis of the DPA of injection protons is not presented in this thesis but it should be noted that they might play some role in the primary collimator depending on the expected injection losses.

5.4.2 Primary collimators

Disentangling DPA contributions

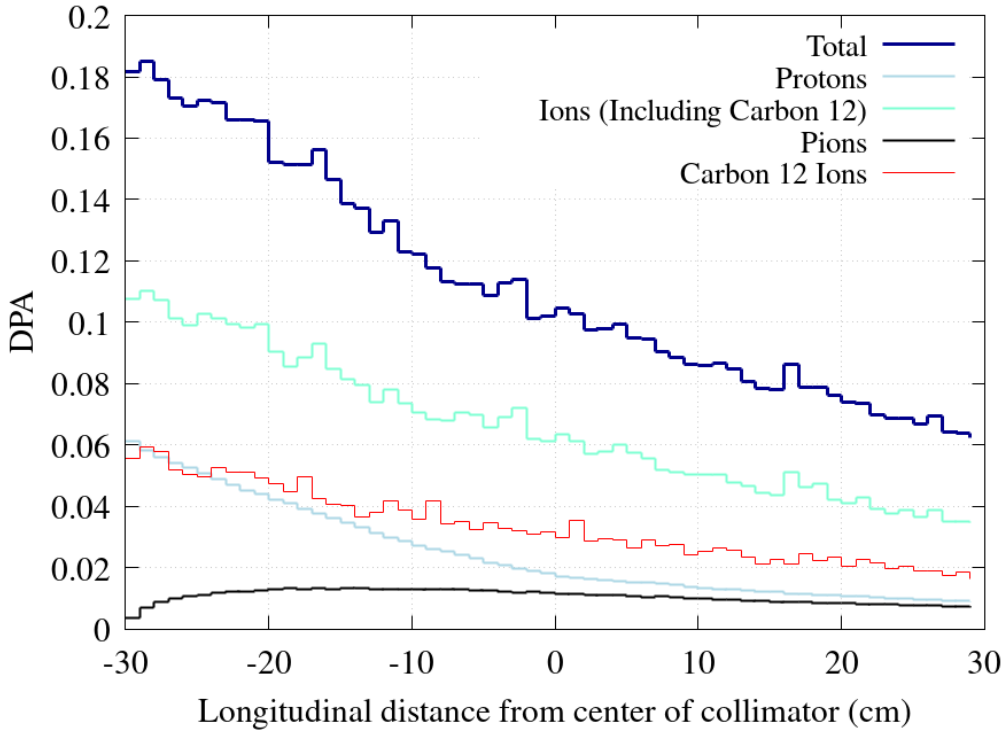

Figure 5-12: Longitudinal profile of DPA in the TCP.C jaw (AC150GPH) predicted for $Np_{7TeV} = 10^{17}$ lost protons. The contribution from the different particles is disentangled.

The most impacted primary collimator, in terms of peak DPA, is the horizontal oriented one (TCP.C) located in IR7 assuming horizonal losses. In reality some portion of the cumulative losses may be shared with the vertical collimator, but a conservative approach of fully horizontal losses is adopted in this thesis. Figure 5-12 illustrates the longitudinal peak DPA profile in the TCP.C for $Np_{7TeV} = 10^{17}$ total proton lost in the LHC. In this collimator peak DPA values are dominated by primary proton impacts, meaning that it is the proton's first time interacting with a collimator. Consequently, the peak DPA values are found close to the surface of the collimator jaw (5-10 um) and are heavily sensitive to the particle impact parameters on the collimator.

The contribution of hadronic cascade, represented by the pions and heavy recoils in Figure 5-12, is low at this stage. A large contributor to the DPA upstream stems from

Coulomb interactions of primary protons with nuclei (nuclear stopping) and from the carbon recoils coming out of the elastic nuclear interactions with the jaw material. At deeper levels from the surface, not shown in the plot, DPA steeply falls to lower values and the contribution of particles in the hadronic cascade becomes dominant.

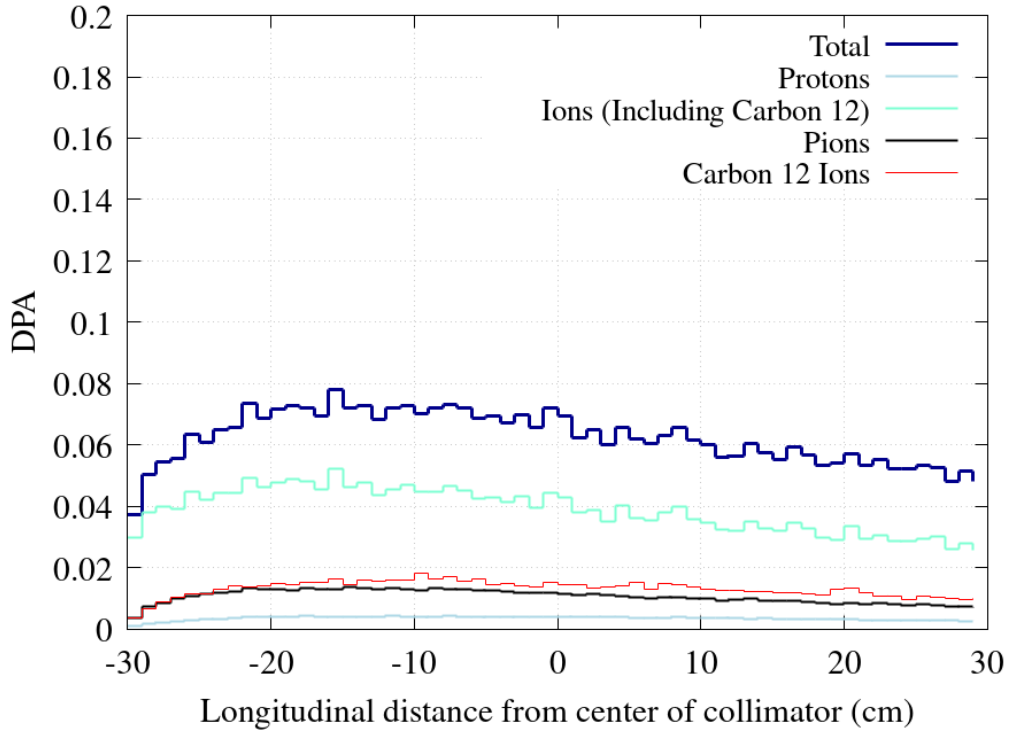

Figure 5-13: Longitudinal profile of DPA in the TCP.C jaw (AC150GPH) predicted for $Np_{7TeV} = 10^{17}$ lost protons. The contribution from the different particles is disentangled. DPA is scored only after the first inelastic interactions of the impacting protons.

These peak values are of importance since this degradation of the material at the impact point may affect the cleaning behaviour of the material. However, due to the small scale, any imperfections (e.g. material roughness, misalignments etc.) could average the DPA in a larger cross-sectional surface. For this reason, it is also of interest to examine the average DPA in a larger surface to provide a minimum level of the estimated peak DPA on the collimator jaw. To achieve this, similar to the previous section, two different sizes of scoring meshes were used for the transversal coordinates x and y: a fine mesh (5x5 μm^2) to match the beam impact parameter and a coarse mesh (400x400 μm^2).

Past studies used to transfer the information of inelastic interactions that were calculated from the tracking studies, to be used as input for the subsequent radiation transport analysis. Figure 5-13 shows the same information as Figure 5-12 with the exception of DPA being recorded only after the initial protons have had their first inelastic interaction in the collimator jaw. One can see that the contribution of pions is identical between the two figures since pions are only produced during inelastic interactions. The differences between the rest of the curves is due to the nuclear stopping of primary protons (i.e. Coulomb interactions with nuclei) and due to recoils produced in elastic nuclear interactions. It is noticeable that downstream the curves are almost identical since there are no more beam protons traversing the end of the collimator due to the negative impact angles explained in section 3.4.

Comparison of peak DPA levels

Figure 5-14 compares the peak DPA in the primary horizontal (TCP.C) discussed above with the peak DPA in the skew (TCP.B) collimator for the current design with the jaw material in AC150GPH. Close to the surface (fine scoring), it is estimated to reach 0.18 DPA while in an averaged out surface of 400x400 μm (coarse scoring) the values drop by a factor 25 to 0.006 DPA. The skew collimator is the second most impacted primary collimator in terms of peak DPA and the most impacted in terms of total energy deposition in the whole jaw. Since the majority of initial impacts and inelastic interactions of the protons happen already in the TCP.C upstream, the DPA in the skew collimator is mainly induced by the products of the hadronic cascade. The maximum DPA for the skew reaches 10^{-3} uniform over a larger cross-section (1x1 mm^2). In this case, a finer mesh is not required since the skew primary collimator is impacted mainly by the spatially spread out particles escaping from the horizontal one.

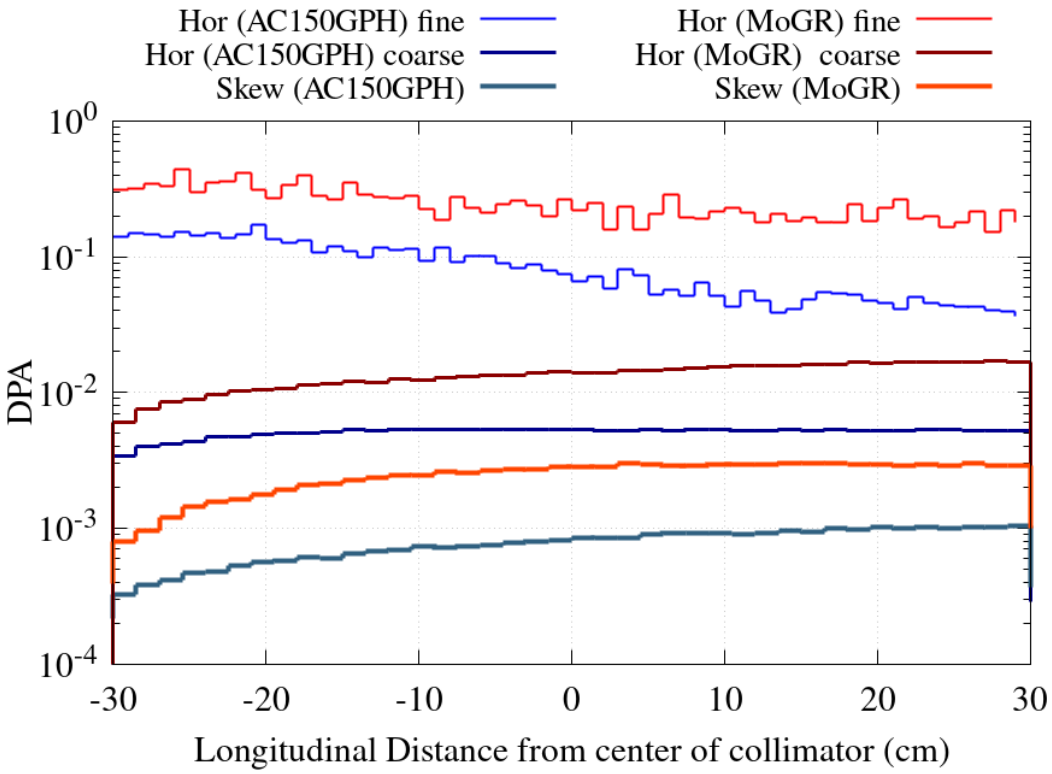

Figure 5-14: Longitudinal profile of total DPA in TCP.C (Hor) and TCP.B (Skew) jaws (AC150GPH and MoGR) predicted for $Np_{7TeV} = 10^{17}$ lost protons with fine (5x5 μm^2) and coarse (400x400 μm^2) scoring meshes.

One of the foreseen upgrades to the LHC collimator system is the change of the collimator material from AC150GPH to MoGR due to various advantageous material properties. To this end, Figure 5-14 presents the results of the same study with jaw material in MoGR. As can be seen in the graph, the overall characteristics of the DPA profiles remain qualitatively the same. However, the values increase by a factor of 2 for the peak in the TCP.C and by a factor of 4 in the other cases, predicting a peak DPA of 0.3 in the TCP.C.

The above results are based on a perfect machine where the beam load is shared almost equally between the two jaws of the collimators. However, as was presented in Section 3.4, in the presence of imperfections (e.g. angular misalignment of the primary collimator), the beam might impact only one of the primary collimator jaws. This implies that in the worst possible scenario where the beam is constantly being cleaned

by only one jaw the values mentioned for the impacted collimator (TCP.C) could increase by a factor of 2 if the misalignment is not corrected.

5.4.3 Secondary Collimator

The expected peak damage in secondary collimators is less than in the primaries, since the former ones are only exposed to a fraction of high energy protons and to diluted showers escaping from the primary collimators. Furthermore, contrary to the primary collimator, impacts on the TCSGs are far less concentrated in a small impact point, lowering the peak but increasing the size of the damaged area. The most impacted TCSG is the first collimator following the initial three primaries, which is located after a set of warm dipoles. The rest of the TCSGs are not explicitly studied at this stage. Nevertheless, judging from the simulated proton impact loss maps (Figure 3-5) and the energy deposition sharing between the collimators (Figure 5-1) similar levels are expected for the downstream secondary of cell 5 (TCSG.A5R7, TCSG.B5R7) while more than an order of magnitude less damage is expected for the rest.

Disentangling DPA contributions

In Figure 5-15, the cumulative peak DPA profile in the most impacted secondary collimator (TCSG.A6), assuming CfC (AC150GPH) as absorber material. The results have been scaled to the estimated number of protons lost during the HL-LHC lifetime. The figure also shows the DPA contributions from different families of particles. The shape of the peak is different than in the primary, with the peak DPA profile increasing along the collimator, reaching its maximum at the collimator end. The main contribution is due to electromagnetic showers (EM) showers which develop inside the absorber block.

It is apparent that the majority of the damage comes from the products of the inelastic interactions of the initial protons and not the protons themselves. On the other hand, the picture does not resemble Figure 5-13. This is explained by the fact that the inelastic interactions in this collimator are far less dense than the primary. Consequently, the far more spatially spread electromagnet showers dominate the total DPA that is averaged out over a larger area.

As a side note, the initial bump observed in the EM showers curve is caused by showers that escaped the primaries and impacting directly on the secondary collimator.

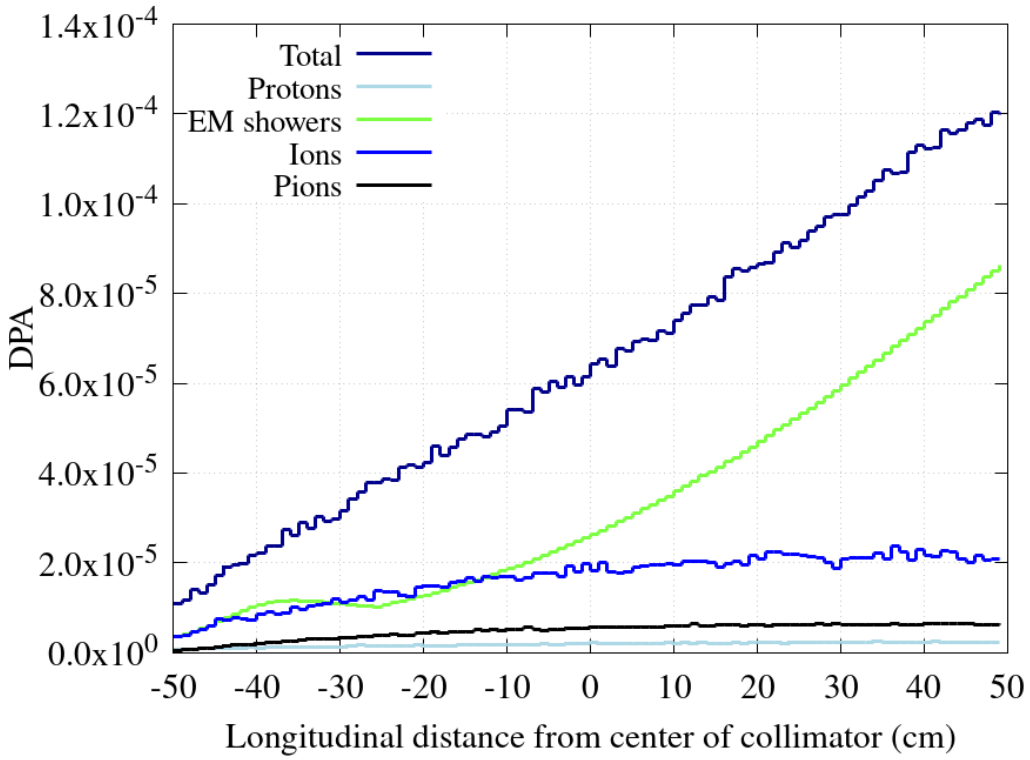

Figure 5-15: Longitudinal profile of DPA in the TCSG.A6 (AC150GPH) predicted for $Np_{7TeV} = 10^{17}$ lost protons in the CS. The contribution from different secondary products is also shown.

Comparison of maximum DPA levels

In Figure 5-16, an overview of the DPA profiles in the TCSG.A6 for current and future absorber materials (AC150GPH and MoGR, respectively) is presented. In addition, in the case of MoGR, a thin layer of 5 μm of Molybdenum coating will be applied at the surface of the collimator in order to further reduce its impedance.

The estimated DPA in this coating is shown as well. As can be seen the peak DPA values reached in this surface coating are about an order of magnitude higher than the DPA in the CfC, reaching 10^{-3} DPA compared to 1.2×10^{-4} DPA in CfC. In the MoGR bulk material the DPA is expected to reach 4×10^{-4} DPA. Qualitatively, the pattern and the secondaries contribution are similar as in the CfC case.

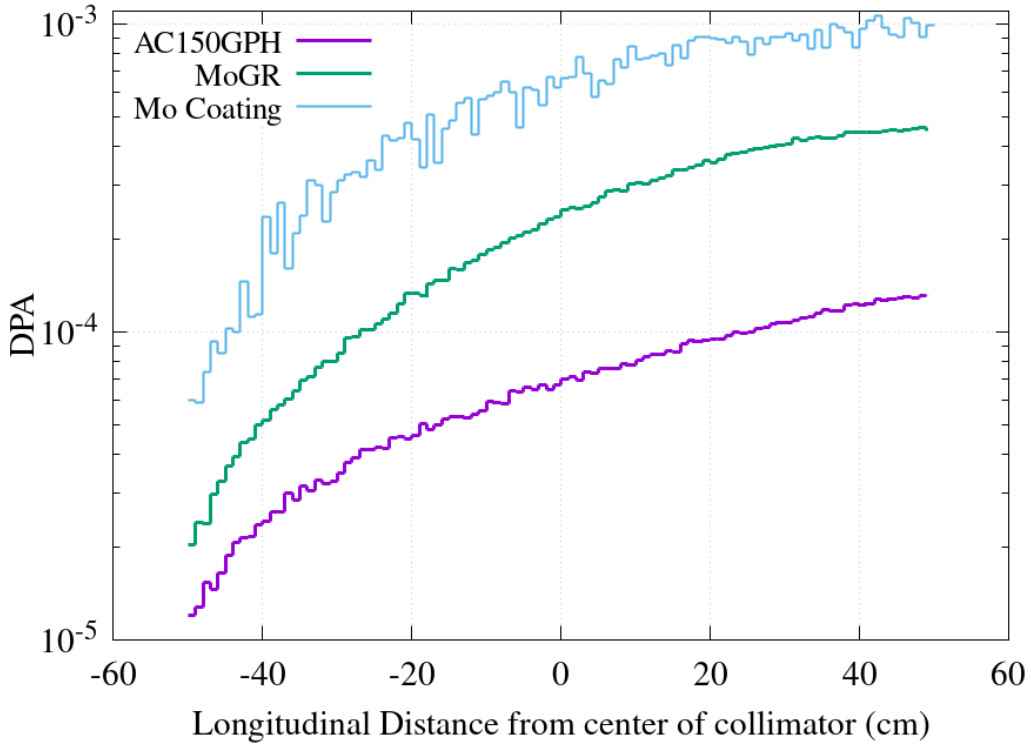

Figure 5-16: Longitudinal profile of total DPA in the active jaw of the TCSG.A6 in AC150GPH and MoGR and in its foreseen Mo coating for $Np_{7TeV} = 10^{17}$.

The higher value of the DPA in the coating could mean a faster degradation of material properties over the HL-LHC lifetime and its effectiveness in reducing the resistive wall impedance could potentially diminish. Therefore, more experimental irradiation campaigns are ongoing in the context of the ARIES European project (84) to evaluate the diminishing properties of the coating as a function of DPA.

5.5 Conclusion

This chapter focused on the radiation impact of the highly energetic proton beams on the LHC collimation system with a strong focus on the betatron cleaning insertion region (IR7). To begin with, by studying the energy deposition sharing between the machine elements, it identified the most impacted points of the machine for further investigation. These were the primary horizontal and skew collimators as well as the first secondary collimator at the position of TCSG.A6. It also showed that the normal

conducting magnets in close proximity to the collimators are highly exposed, leading to further investigation in Chapter 6.

Short term radiation impact on collimators were studied, by considering short beam lifetime scenarios. The presented results highlighted for the first time the effect of realistic highly concentrated proton impacts on the primary collimator material. It showed that due to the small impact parameter the energy density increases due to the energy deposited due to the ionizing energy loss of the primary protons. In cases such as the primary and secondary skew collimators, the maximum energy density is governed by electromagnetic showers which are induced by secondary particles leaking from the upstream primary collimator . In the present LHC a peak power density of $3kW/cm^3$ is found, if one assumes an ideal alignment of the collimator jaws. This value could increase by a factor of 2 if one jaw cleaning is considered due to imperfections (jaw tilt). Moreover, in the case of possible change of material of the primary collimator absorber blocks to MoGR, this value could surpass $10kW/cm^3$ for 0.2h BLT of HL-LHC beam.

In order to estimate the long-term radiation damage, displacements per atom were calculated for the same collimators as above using as normalization the estimated number of protons lost in the collimation system for the full HL-LHC lifetime based on the simulations and measurements presented in Chapter 3.

Table 5-3: Total DPA for the most impacted primary and secondary collimators for the HL-LHC. Results are shown for the presently used CfC grade (if it would be kept throughout the HL-LHC era) and for the MoGR compound.

	Total DPA for Np_{7TeV} = **3 x 10^{17}** (Table 4-8)						
	Primary Horizontal		Primary Skew		Secondary TCSG.A6		
Material	*AC150 GPH*	*MoGR*	*AC150 GPH*	*MoGR*	*AC150 GPH*	*MoGR*	*Molybdenum Coating*
DPA	***0.6***	***1.2***	***3 x 10^{-3}***	***9 x 10^{-3}***	***0.4 x 10^{-3}***	***1.4 x 10^{-3}***	***3 x 10^{-3}***
(Averaged)	***(1.5 x 10^{-2})***	***(5 x 10^{-2})***					

Table 5-3 shows the maximum DPA reached for primary and secondary collimators in various materials for Np_{7TeV} = **3 x 10^{17}** (Table 4-8) which includes a safety margin of a factor of 3. The horizontal collimator is estimated to reach a maximum of the order of 1 DPA. However, due to the very small impact parameter (less than 5 um) uncertainties due to the roughness of the collimator etc. may change this result. For this reason, an averaged value over a 400x400 μm^2 in x and y mesh is presented in addition to evaluate damage in a more tangible size on the primary horizontal collimator. Values of the order of 10^{-2} DPA can be seen for the horizontal and of the order of 10^{-3} for the skew primaries. The most impacted secondary skew collimator reaches similar values of the order of 10^{-3} DPA.

Chapter 6 Radiation Impact on magnets

This chapter aims to examine the limitations that the collimation losses impose on the normal operation of the LHC due to their radiation impact on magnets. The main goal of the studies is to pre-emptively identify machine weak points and examine the effect of possible mitigation measures.

6.1 Introduction

The radiation impact on both the normal conducting (warm) as well as the SC magnets is evaluated. The former are located in the long straight section of the betatron cleaning insertion region (IR7) and the latter in the dispersion suppressor (DS) region downstream of IR7. The harsh radiation environment in the collimation insertion can for example lead to magnet failures due to long-term radiation damage of sensitive magnet components. This mainly concerns the warm magnets due to their proximity to the collimators. On the other hand, particles leaking from the collimation system may also limit the machine performance if they induce quenches of superconducting magnets. Both the risk of radiation-damage induced failures and the risk of magnet quenches is studied in this chapter using particle shower simulations.

Long term effects

It was already demonstrated in Table 5-1 that only about 15% of the beam's energy is absorbed by the collimator assemblies. A large percentage is escaping and about 16% is absorbed by the normal conducting magnets. While these magnets are protected by passive absorbers (TCAPs) and they cannot quench like SC magnets, they are still susceptible to failure due to long term radiation damage. Contrary to the collimators the organic plastic material used for the coil insulations and spacers of the normal

conducting magnets of IR7 degrade in correlation with the cumulative dose that they absorb (85). This chapter presents the study of the cumulative dose absorbed by the sensitive resin insulations of magnets in the proximity of the collimators. The dose is estimated for the full HL-LHC lifetime based on the loss estimations of Chapter 4. Furthermore, it describes the effect of the considered mitigations measures taken with the goal of anticipating possible failures and preventing machine downtimes.

Short term effects

The beam cleaning efficiency of the collimation system is a matter of constant concern, in order to reduce the risk of unwanted SC magnet quenches in the downstream dispersion suppressor (DS) region. However, the quench levels of the SC magnets are not well understood, especially for the future 7 TeV operation. This chapter aims to quantify the power deposition levels in the SC coils that were achieved during the collimation quench tests of 2015 for both protons and ions. Combined with the simulation benchmark presented in Chapter 3, the results provide insight on the quench limits of the SC magnets and consequently the limitations imposed by the performance of the collimation system.

6.2 Radiation-induced failures of normal conducting magnets

The LHC normal conducting (warm) magnets located in IR3 and IR7 consist of dipoles (Magnet Bending Warm, MBW) and quadrupoles (Magnet Quadrupole Warm, MQW). The dipoles are used for enlarging the inter-beam separation at the interaction points from 19.4 cm to 22.4 cm while the quadrupoles are needed for keeping the beam focused. The primary collimators are located at the so-called dogleg, meaning between the set of 2 MBWs that are used for separating the beam. Figure 6-1 shows the layout right of Point 7 starting from the Beam 2 primary collimators on the right, followed by the two most impacted MBWs and, after the most loaded secondary collimator (TCSG.A6R7), arriving at the first set of MQWs of cell 5. Further downstream, the second set of MQWs at cell 4 reside with two secondary collimators before and one

in between them. In order to protect the warm magnets, three passive absorbers are placed, one before each MBW and one before the first cell 5 MQW, the MQW.E5R7 (all elements are listed in direction of the anti-clockwise beam, i.e. from right to left in the figure).

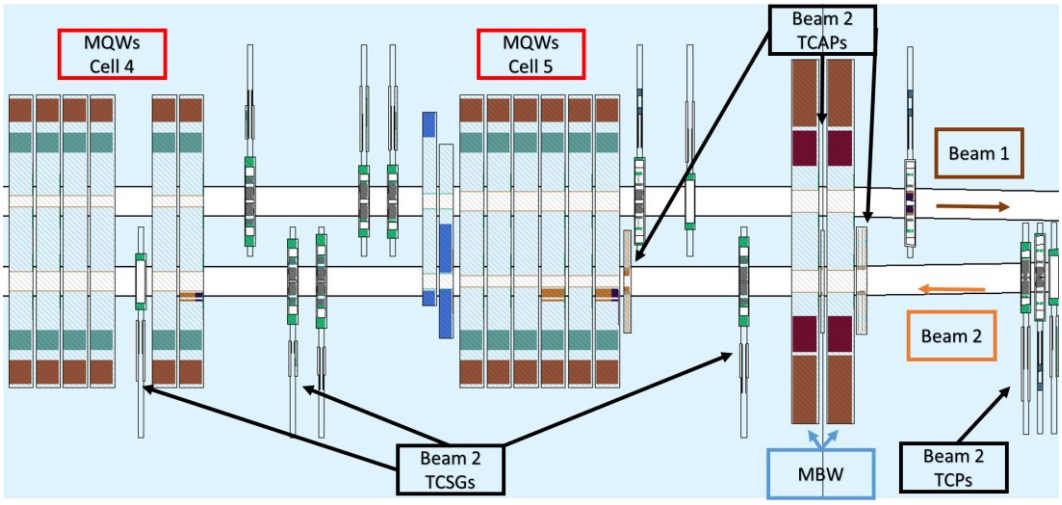

Figure 6-1: IR7 layout of the warm magnets relative to Beam 2 collimators (not to scale).

The warm magnet coils are insulated and supported through the use of various kinds of resins. A detailed experimental study was carried out that reported the degradation of these materials with respect to the cumulative absorbed radiation dose (85). As an example, Figure 6-2 shows the degradation of the resin strength that is used for the coil spacers of the warm quadrupoles. It is shown that the material quickly degrades in strength after a few tens of MGy of absorbed dose. The radiation hardness of the various resins used ranges from a few tens of MGy to a couple of hundreds of MGy depending on the molecular composition and additives. Since failures are statistical by nature, it is estimated (86) that the minimum values that guarantee the mechanical properties of the magnets are 15 MGy for the MQW and 40 MGy for the MBWs.

CERN 98–01/A3/E

Material:	**Epoxy resin**	TIS No. **R 422**
Type	**MY 745 (50) + EPN 1138 (50) + CY 221 (20) + HY 905 (120) + DY 073 (0.3)**	
Supplier:	**Ciba-Geigy**	UL 94: n.m.
Remarks:	used for the ISR dipoles	LOI:

Radiation test results according to IEC Standard 544 (and ISO 178)

Dose rate (kGy/h)	Dose (MGy)	Ultim. strength (MPa)	Deformation ε (%)	Modulus (GPa)
0	**0**	**153±3**	**13.1±1.9**	**3.80±0.03**
0.2	**0.5**	**142±1**	**12.9±0.3**	**3.50±0.02**
0.2	**2.0**	**140±1**	**7.9±0.3**	**3.50±0.02**
180	**5**	**93±2**	**6.1±0.3**	**4.00±0.03**
180	**10**	**73±3**	**4.2±0.2**	**4.10±0.04**
0.5	**12**	**71±6**	**2.1±0.2**	**3.7±0.1**
180	**20**	**13±1**	**1.1±0.1**	**3.40±0.04**

Radiation index (RI) = 6.9 if strength is the critical property

Radiation index (RI) = 6.6 if deformation is the critical property

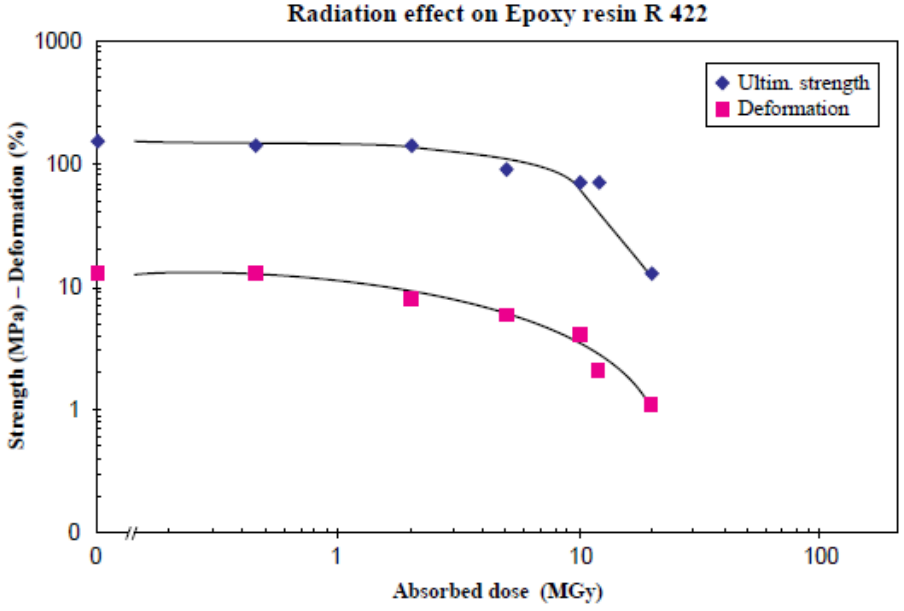

Figure 6-2:MQW spacer resin degradation due to cumulative dose (87)

The two type of magnets are studied separately through FLUKA simulations with the aim of identifying the peak cumulative dose absorbed by the magnet coils and spacers. All results are normalised to the maximum predicted number of proton losses from Table 4-7, Np=10^{17} for the HL-LHC era. In addition, as can be seen on the left of Figure 6-3, that also shows a 3D rendering of the FLUKA geometry of IR7 (right), the effectiveness of a tungsten based radiation shield is studied and presented. The simulation settings and method were identical to the quench test settings presented in Chapter 0 with the exception of the energy that was increased to 7 TeV.

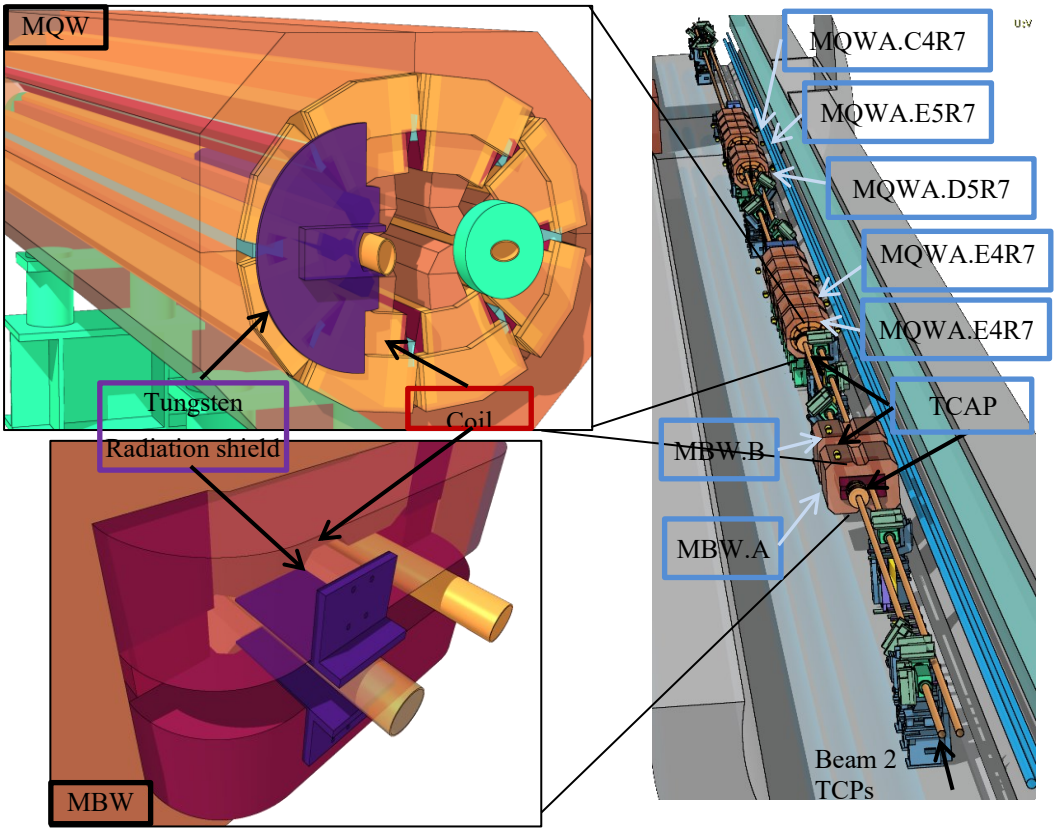

Figure 6-3: FLUKA geometry visualisation of IR7 (right) with notable magnetic elements. Zoom of the MQW (top left) and MBW (bottom right) FLUKA models with their radiation shielding.

Moreover, the results of the dose benchmark study presented in Section 4.4 showed that injection energy proton losses have minimal impact on the warm magnets, with a slight exception of the first MBW.

6.2.1 Warm Dipoles

Figure 6-4 shows a picture of the two MBWs. With the current design, the exposed return coils are the ones that are closer to the beam pipe and therefore to the concentrated showers arriving from the upstream primary collimators. The beam loss monitor dedicated to this device is also seen in yellow colour sitting on top of the magnet. Figure 4-10 shows another perspective with the passive dosimeter holder also being visible. In addition to the dose in the coils, the BLM signals and the passive dosimeter values have also been computed and are available for future studies but are not further discussed here.

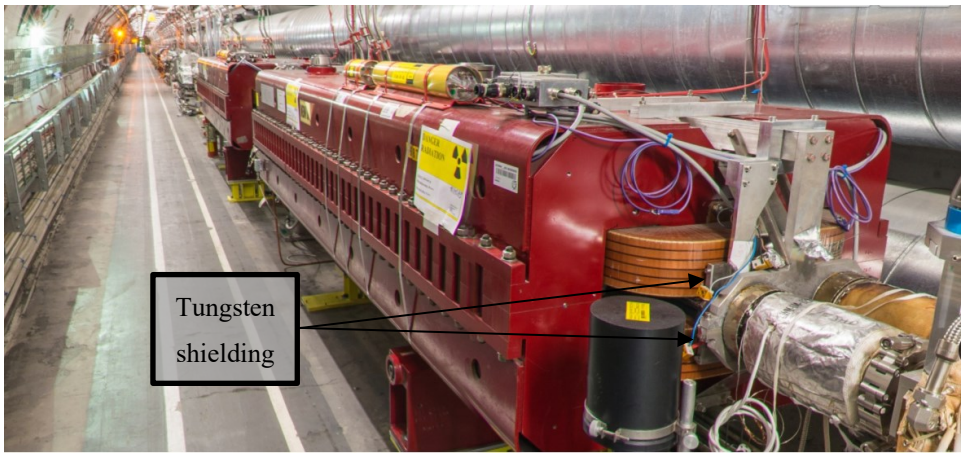

Figure 6-4: Picture of MBW.B6R7 followed by the MBW.A6R7 of the LHC. The tungsten radiation shield is also visible in front of the magnet return coils in the inner Beam 2.

A dose scoring mesh is superimposed on the return coils of the MBW FLUKA geometry in order to quantify the peak cumulative values over the lifetime of HL-LHC. Figure 6-5 illustrates the simulation results on top of the magnet geometry showing that horizontally the peak dose values are indeed at the point closer to the beam pipe. The spatial gradient of the absorbed dose is symmetric in the vertical axis, i.e. the dose is similar between the top and bottom coils.

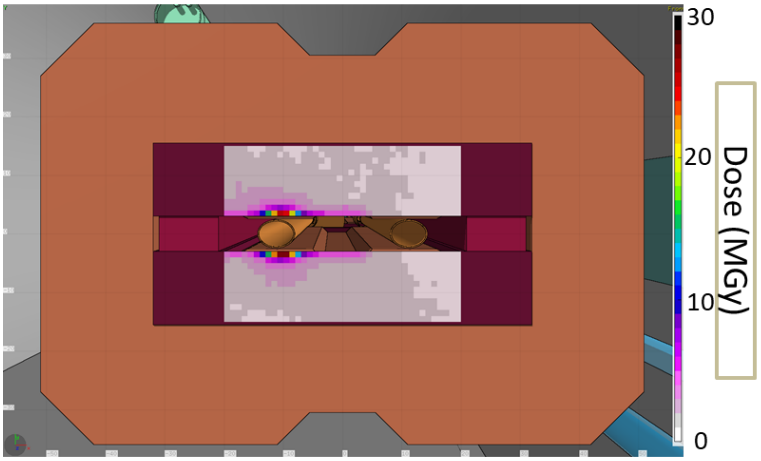

Figure 6-5: Cumulative dose map projected on the MBW return coils for Np=10^{17}. Beam 2 enters the picture in the left beam pipe.

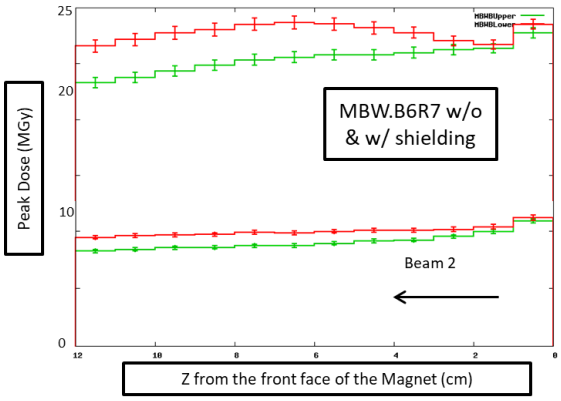

Figure 6-6: Longitudinal peak dose profile for Np=10^{17} in the MBW.B5 front return coil. The dose in the upper and lower coils is shown in green and red, respectively. The two upper curves are for the case without shielding while the two lower curves are with shielding.

The original design of the warm magnets did not include a radiation shield for the warm magnets. However, through these simulations it can be seen that the value of 25 MGy could be reached without considering a safety margin. When a factor of 3 safety margin is considered, the radiation levels that could be reached in the lifetime of the HL-LHC could exceed the damage limit of the organic materials. Consequently, a tungsten radiation shield, designed and manufactured at CERN, was installed on the two most impacted MBWs during LS1 (88).

The longitudinal peak dose profile with and without this shielding (Figure 6-3) is shown in Figure 6-6 for both the top and bottom coils. Indeed, the two coils are equally exposed with slightly higher values on the lower one. The presence of the tungsten masks lowers the peak value by a factor of 3 which automatically translates in an equivalent extension of the magnet lifetime.

Lastly, the effect of the shielding is expected to be much higher for injection energy protons since they induce much less energetic showers. Consequently, the injection proton contribution to the total dose, while not negligible at the entrance of this magnet as measured by the passive dosimeters (Figure 4-11), is not expected to change the conclusion that the shielded magnet should remain functional in the HL-LHC era.

6.2.2 Warm Quadrupoles

Figure 6-7: Picture of MQW.E5R7 of the LHC with the rest of the cell 5 quadrupoles following. The tungsten radiation shield is also visible in front of the magnet return coils in the inner beam 2

Figure 6-7 shows a picture of the six warm quadrupoles located in cell 5. The return coils of the MQW.E5R7 are visible in the front as well as the tungsten alloy radiation shield in silver. The geometry of the quadrupole is much more challenging in terms of modelling with a lot more components of complex geometrical shapes.

In order to identify weak points of the magnets and the components which are mostly affected by the radiation, a large 3D dose scoring mesh covering the totality of the magnet was utilised. Figure 6-8 illustrates the dose predicted by FLUKA per impacting proton on the magnet aperture. While a high proton impact in the warm magnet aperture is highly unlikely, the specific study was used in order to assess the BLM signal threshold to be used in case of an anomalous orbit bump that caused direct losses inside the warm magnets.

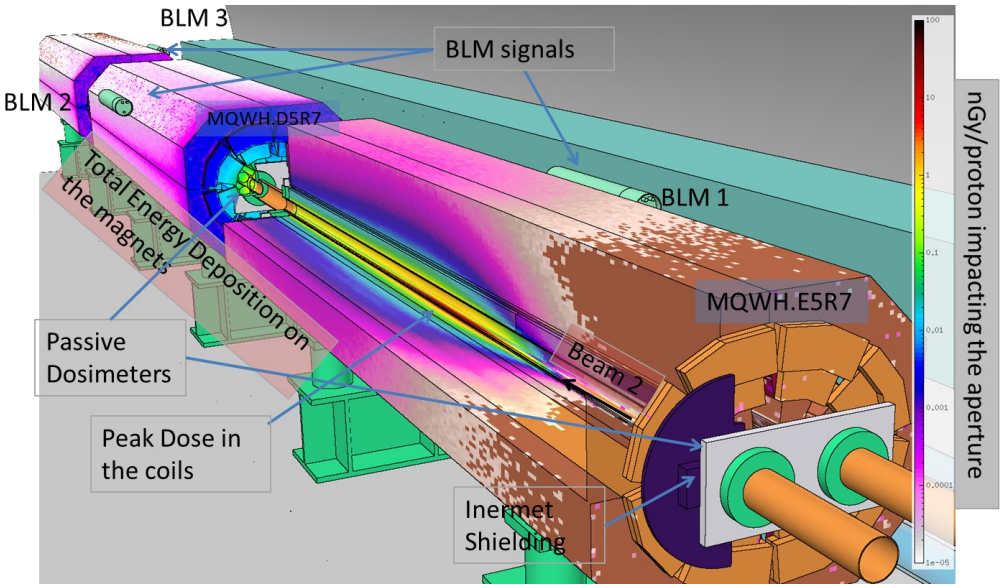

Figure 6-8: FLUKA dose scoring and other quantities of interest of an accidental beam impact in MQWH.E5R7

The total power deposited in the MQW.E5R7 as shown in the Table 5-1 is of the order of 3% of the total power impacting on the collimation system. It was shown experimentally (89) that the MQW cooling system is capable of evacuating the deposited energy even at peak loss rates. To facilitate the experimental testing in mimicking the LHC conditions, a map of the energy deposited per proton loss in the collimation system was generated and is shown in Figure 6-9. This map was experimentally duplicated by utilizing special heaters, placed in key positions inside a spare MQW in the test area. To fully replicate the final power deposition, the water

flow of the magnet cooling was lowered accordingly in order to emulate the power balance difference.

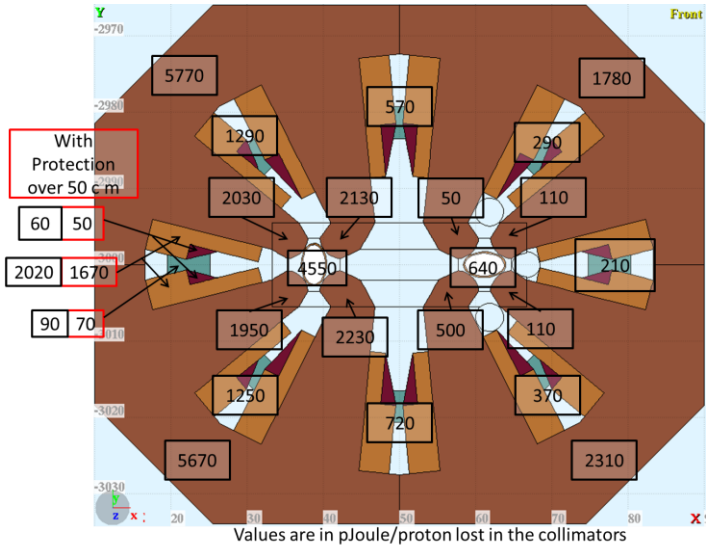

Figure 6-9: Total energy deposited to the various geometrical elements of the MQW.E5R7. Beam 2 enters the left beam pipe.

In analogy to the MBWs, a cross section of the dose map at the longitudinal peak dose position inside the MQWs is shown in Figure 6-10 (right). In this case, no tungsten shield was considered. Moreover, contrary to the MBW case, the peak dose is not found in the return coils that are rather further away from the beam pipe but in the coils running all along the magnet. On the left side of the same figure, a zoom of the map at the most impacted coil cross-section is shown with the values inside the coils reaching nearly 7 MGy. Similar values are reached in the bowtie shaped spacer between the two coils.

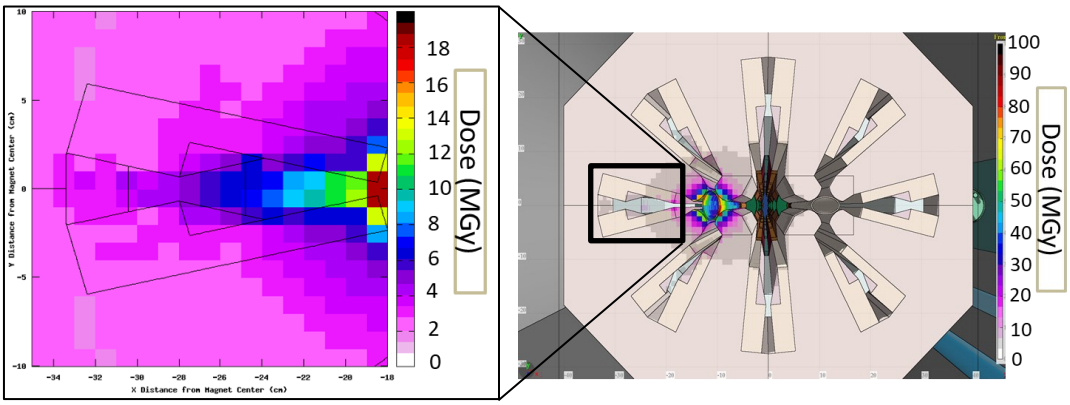

Figure 6-10: Dose map projected on the MQW (right) and a zoom of the most impacted coil and spacer (left) for Np=10^{17}. Beam 2 enters the picture on the left beam pipe.

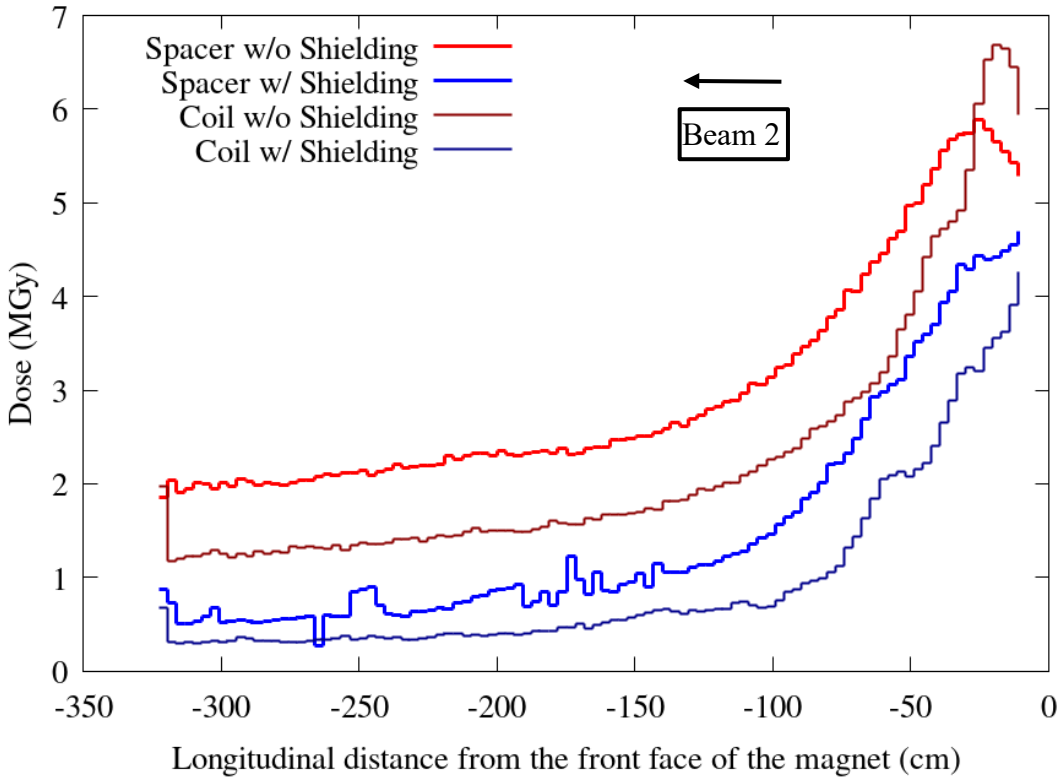

Figure 6-11: Peak dose profile for Np=10^{17} in the MQW.E5 middle centre coil.

It's worth noting that some scoring bins seem to overlap between the air and coil material with higher values than the bins that are fully inside the coil material. These

bins were dismissed as it was identified that they were reporting artificially high values due to an artefact in the scoring at the interface plane between air and coil.

Figure 6-11 shows the peak dose profile over the length of the MQW.E5R7 on the most impacted coil and the spacer as seen in the previous figure. In addition, the effect of the tungsten radiation shield installed is shown. The maximum dose manifests on the front of the magnet with the radiation diminishing deeper in the magnet.

The effect of the shielding is of the order of 40% at the maximum for the coils and 30% for the spacers. These values are once again below the damage limit but as was the case for the MBW it may be the case that in the spacer the damage limit of 15 MGy can be surpassed when a safety margin of factor of 3 is taken in the total losses.

Similar graphs were calculated for all subsequent MQW magnets with and without shielding and the results are summarised in the conclusions Section 6.4. As can be seen in Figure 6-11, the effectiveness of the radiation shield becomes greater in further inside the magnet. Consequently, in the subsequent magnets following this most impacted one the radiation shield is more effective reducing the expected doses by several factors.

6.3 Quench margin for superconducting magnets

The LHC's high-field bending dipole magnets (MB) (Figure 6-12 left), will operate at 12 kA current and generate magnetic fields of 8.33 T when the beam energy will reach the design value of 7 TeV. The main quadrupoles (MQ) (Figure 6-12 right) provide a nominal gradient of 223 T/m when the peak field in the coils reaches 7.5 T. The coils of both types of magnets are wound from NbTi Rutherford superconducting cables (Figure 3) that require to be cooled down to 1.9 K.

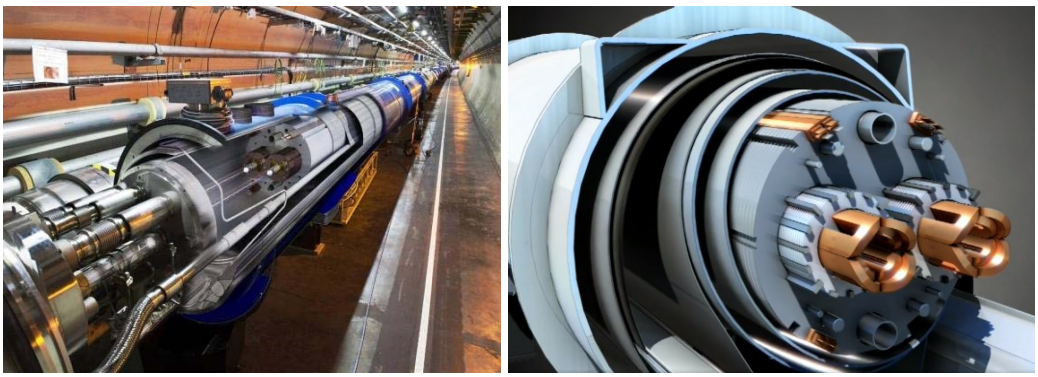

Figure 6-12: The LHC superconducting bending dipole (left) and quadrupole (right) magnets (90)

If the energy deposited by high energy beam losses in the SC coils is above a certain limit, it can cause them to transition to the normal conducting state otherwise known as a quench. A good understanding of the quench levels for the different beam loss scenarios is of high importance in order to ensure an operational stability. Various attributes define what a beam-loss scenario is, such as the type of affected magnet, the beam energy, the duration and magnitude of losses as well as the spatial distribution of the losses. The minimum local power deposition density in the SC coils that, for a given scenario, will result in a quench is defined as the quench limit.

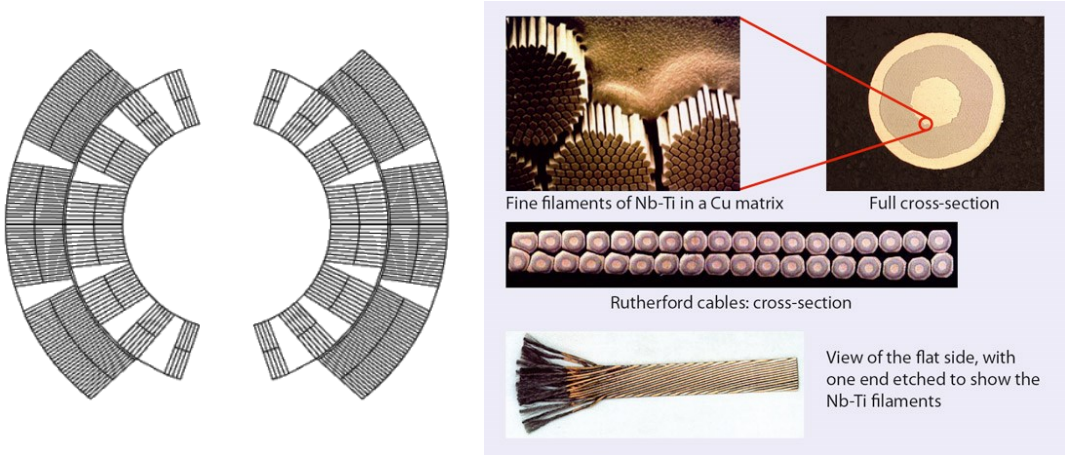

Figure 6-13: (Right) The NbTi Rutherford superconducting cables used at the LHC (91). (Left) The MB coil cross section (92)

In this chapter, the peak power density reached during the conditions of the 2015 collimation quench tests (Section 3.2) is evaluated in an effort to contribute in the understanding of the magnet quench limits.

Evaluation of quench levels for 6.5 TeV

The quench level in the context of steady-state losses, is defined as the maximum power density, that a part of the superconducting coil may sustain without provoking a quench. To quantify the quench levels for certain loss conditions, the power deposition in the coils must be evaluated. Unfortunately, there is no robust and easy direct way of measuring the power deposition in the coils, one must rely on Monte Carlo simulations. An accurate description of all the magnetic elements is required as well as the beam aperture that determines the proton losses in the machine (e.g. the magnet interconnects in Figure 6-14). While one could argue that for the specific study, only the aperture and magnet coils are required, this is not true for scenarios where the benchmark of the simulation is done through a comparison with BLM signals (Chapter 3).

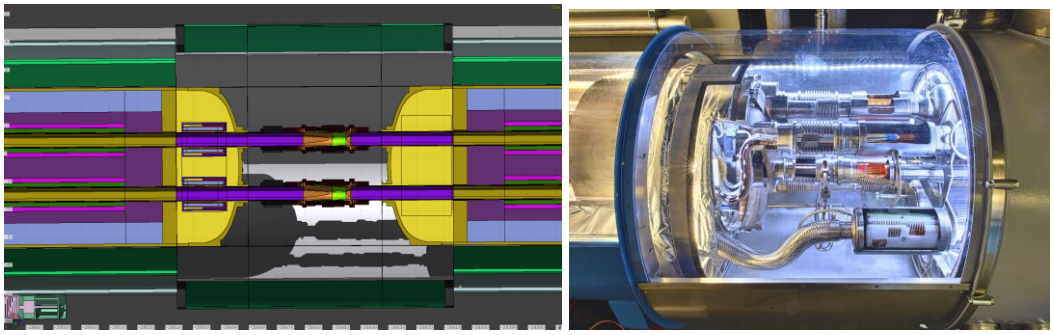

Figure 6-14: LHC interconnect picture (right) and FLUKA model (left).

The energy deposition in the coils were scored at the same time as the BLM signals presented in 3.3 for both the proton and ion quench tests. In addition, a detailed cylindrical energy deposition scoring mesh was utilised with r,φ,z dimensions of (0.2 cm, 2°,10 cm) covering the coils of the 14.3 m of the magnetic length of each dipole and the 3.2 m of each quadrupole. This fine mesh (radially) is used to identify the true peak power density in any part of the coil. However, for the time scale of steady state losses, each cable is considered to have sufficient heat transfer within it. Consequently,

the value of interest is the radially averaged power density in the cable rather than the absolute peak value reached at any given point (42).

6.3.1 The 2015 proton quench test

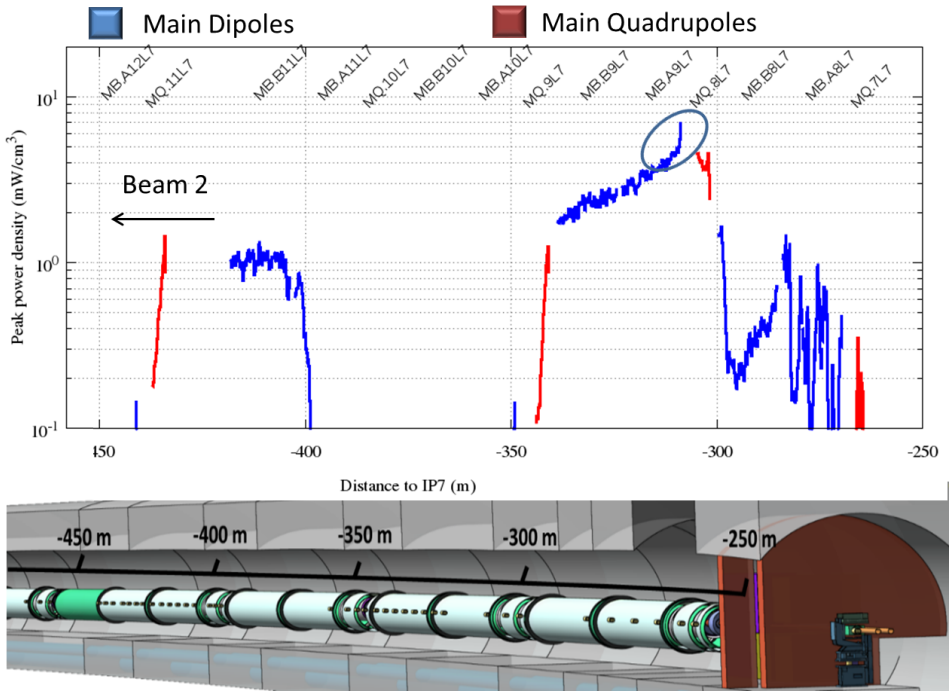

Figure 6-15: Peak power density profile in the SC coils of DS magnets for 585 kW proton losses in the collimation system. The beam direction is from the right to the left.

The results of the experimental test are described in detail in section 3.2.1. The test was carried out at a beam energy of 6.5 TeV. The key values of interest for this study are the peak power loss of 585 kW that was reached during the test and the loss rate profile. The latter can be seen in Figure 3-1 showing a roughly linear increase profile over 5 seconds with the peak loss rate being sustained for the last seconds. Moreover, no beam-induced quench occurred during the test, meaning that the following power density values stand as a lower bound for the quench levels at 6.5 TeV for the specific loss scenario.

Figure 6-15 shows the longitudinal peak power density distribution in the SC coils of DS magnets , produced by the simulation chain. The results were normalised to 585

kW of total proton losses in the collimation system. The blue curve represents the power deposited in the MBs and the red curve the one in the MQs. The very pronounced maximum value of 7.7 mW/cm^3 is reached at the front face of the first dipole magnet of cell 9 the MB.A9L7. Similar levels can be seen also on the upstream MQ.8L7 while in cell 11 magnets downstream a peak power density of 1.5 mW/cm^3 is reached. As expected, the peak power density pattern qualitatively follows the proton loss pattern that is generated by the tracking simulations (Figure 3-5).

Figure 6-16 shows a cross-section of the cylindrical scoring at the maximum location. The peak power density appears in the internal coil on the bending side that the off-momentum protons impacted.

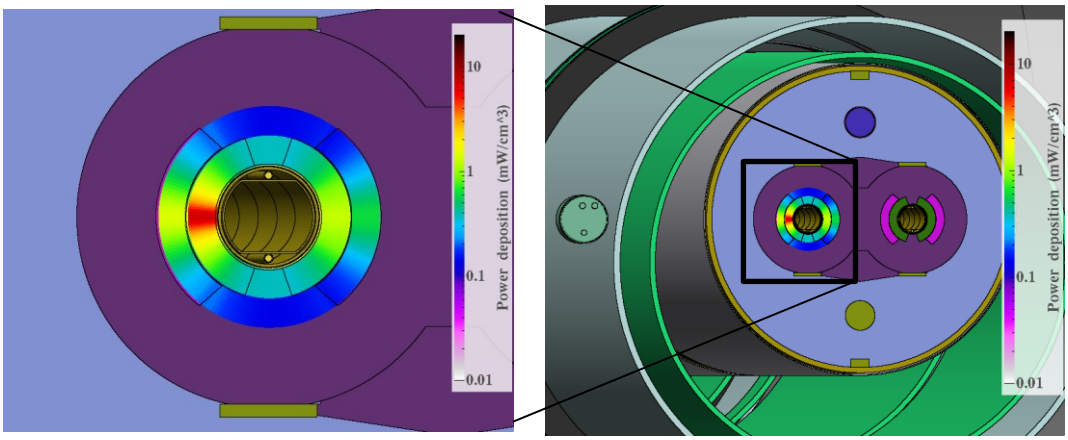

Figure 6-16: Power density cylindrical scoring on the MB.A9L7 FLUKA model (right) and a zoom in the most impacted longitudinal point as seen in Figure 6-15 for 585 kW total losses. Beam 2 enters the picture on the left.

In Chapter 3 it was found that simulated BLM signals were a factor of 3 lower than measured signals up to the Q11, which was attributed to an underestimation of direct proton impacts on the magnet aperture. These results suggest that the peak power density should be scaled accordingly in order to better evaluate the actual power deposition achieved during the quench test. Therefore, a value of 3 x 7.7 ~ 23 mW/cm^3 should be considered as reproducing better the peak power density achieved in the test. In addition, taking into account the power loss profile (Figure 3-1) a 5 sec time average of 13 mW/cm^3 is observed on this overall most impacted magnet.

In order to further evaluate the effect of the possible imperfections on the power deposition in the coils, this section also presents the results for the case of the 400 µrad misalignment of the primary jaws that was introduced in 3.4. Figure 6-17 shows a comparison between the peak power density profiles of the ideal machine, as shown in Figure 6-15, and the 400 µrad jaw misalignment case.

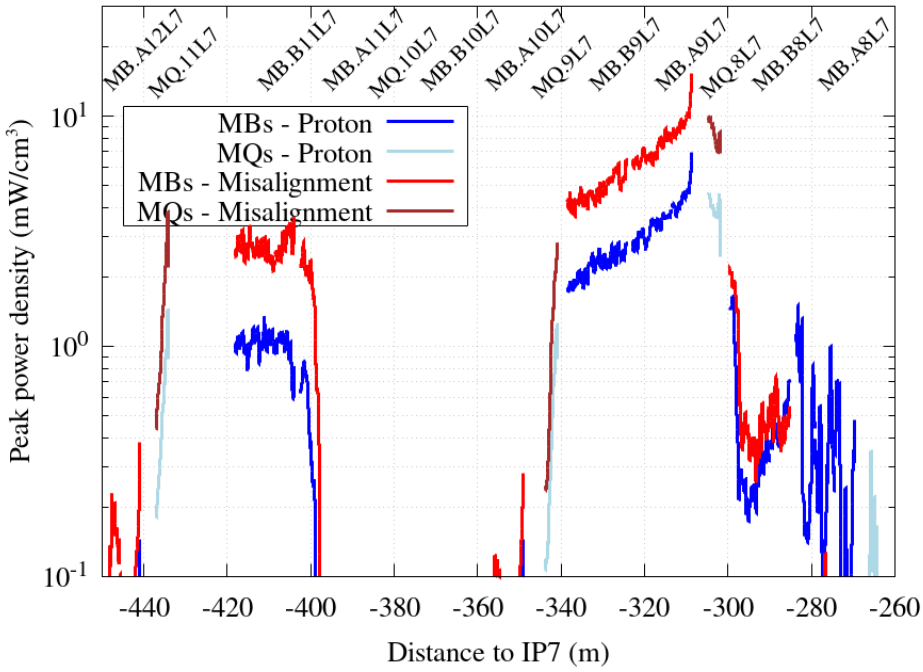

Figure 6-17: Peak power density profile in the SC coils for 585 kW proton losses in the collimation system for perfect machine and with 400 µrad jaw misalignment

The maximum value of 16.5 mW/cm^3 is now found at the same location. The overall pattern is also qualitatively similar between the cases with an overall increase of a factor of ~2 for cell 9 and a factor of 3 for cell 11. This increase is analogous to the improvement of the BLM signal agreement found in section 3.3 leading to the roughly the same scaled up values of 23 mW/cm^3 if the remaining discrepancy in BLM signals is taken into account. This enforces the hypothesis that both the power density inside the coils as well as the BLM signals scale in the same way with the number of protons leaking to the dispersion suppressor. , The latter depends on the presence of imperfections, which can have a great impact on the cleaning inefficiency of the collimation system.

6.3.2 The 2015 ion quench test

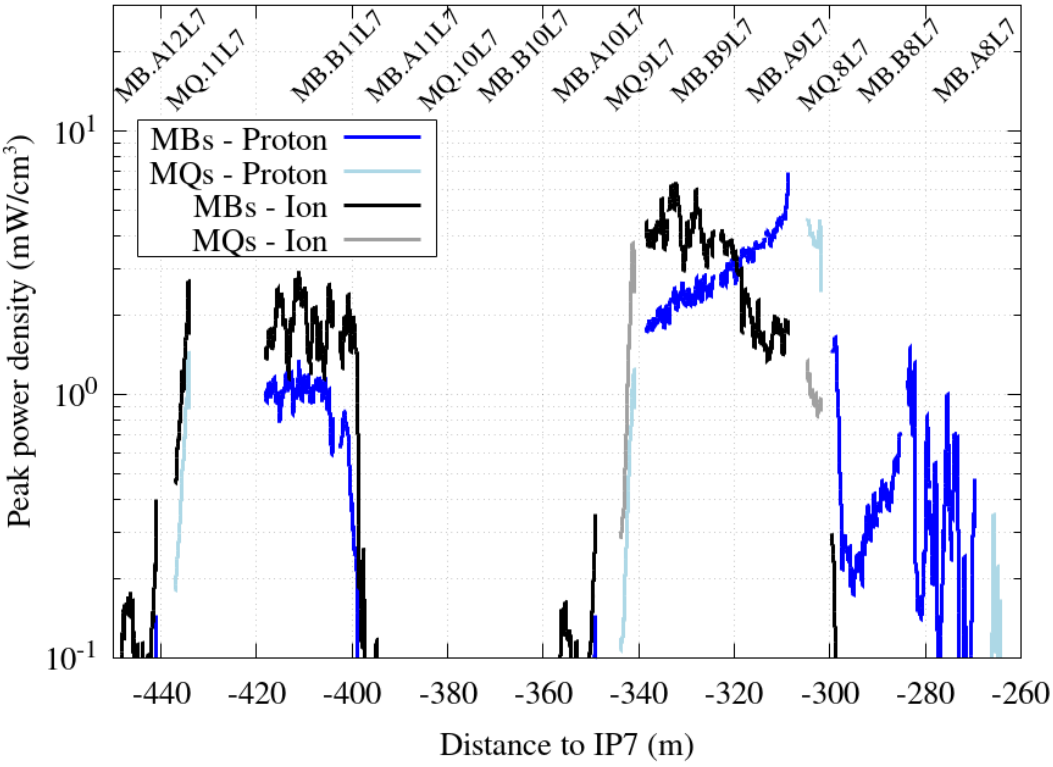

Figure 6-18: Peak power density profile in the SC coils for 15 kW of ion losses during the 2015 ion quench test vs the 585 kW proton losses in the proton quench test.

In the case of the 2015 ion quench test, which was carried out at a beam energy of 6.37 Z TeV, a beam-induced quench was achieved which means that, if the model is accurate, the calculated power deposition presented in this section stands as an upper boundary of the quench limit. Like in the proton case presented above, the power deposition values were scored at the same time as the BLM signals that were reported in 3.5 for the ion case, using the same simulation parameters.

The longitudinal peak power density profile for the 2015 ion quench test is presented in Figure 6-18. The values are normalised for the maximum 15 kW of lead ion losses in the collimation system achieved during the test. A maximum of 6 mW/cm^3 is found for the MB.B9L7 which coincides with the magnet that was subject to a beam-induced quench (3.5). This finding provides extra information on the accuracy of the

simulation chain that was not available for the proton quench test where the location of the losses can only be estimated by comparing with the BLM signals. The overall pattern is relatively noisy related to statistical fluctuations in the simulation results (the statistical error or the maximum peak power density is 20%).

While these numbers seem to be lower than the ones reached for protons where no quench occurred, the BLM agreement is worse than for protons as is was seen in section 3.3. Scaling the Pb results by a factor of 4-5, which corresponds to the observed discrepancy between measurements and simulations, one arrives at a value of 25-30 mW/cm^3 maximum. Lastly, given the power loss profile during the test (Figure 3-3) a time average of 20-25 mW/cm3 is deposited over the last 5 seconds.

6.4 Conclusion

This chapter addressed the short- and long-term effects of radiation impact on the super- and normal conducting magnets because of betatron collimation losses. The results depend on the findings of Chapter 3 and Chapter 4 for either re-scaling the simulation results to account for discrepancies with BLM measurements or utilising the total number of proton losses for making predictions for the HL-LHC era.

Long term effects

As demonstrated in this chapter, the dose deposited in the coils and coil spacers of warm magnets in the betatron collimation insertion can potentially limit the lifetime of the magnets in HL-LHC if no preventive measures are taken. Table 6-1 summarizes cumulative dose predictions for the HL-LHC era, assuming that a total of Np_{7TeV} =3 x 10^{17} protons (7 TeV) are lost in the collimation system, as derived in Chapter 4. The results are colour-coded in two categories; red background if the damage levels are surpassed and green if the magnets are expected to survive the full HL-LHC era. It is shown that the addition of the radiation shields extends the lifetime of the magnets past the HL-LHC era. A notable exception is the MQW.E5 where the dose in the spacers may reach critical values way before that.

Table 6-1: Maximum cumulative dose at the end of the HL-LHC era (Np_{7TeV} = 3 x 10^{17}protons lost) in the coil and the coil spacers of warm magnets in IR7, with and without the tungsten (W) shielding. Red colour indicates that the magnet will not survive the HL-LHC lifetime while green means they will.

Magnet	No shielding		With W shielding	
	Coil	Spacer	Coil	Spacer
MBW.B6	75	n/a	26.1	n/a
MBW.A6	54	n/a	21.0	n/a
MQW.E5	18	18	13.2	13.5
MQW.D5	5.1	6.6	2.1	2.1
MQW.E4	9.0	7.2	3.3	3.0
MQW.D4	3.6	3.6	<1.2	<1.2
MQW.C4	4.8	5.7	<3	<3

In order to mitigate the risk of magnet failure, the MQW.E5 is being replaced by a new copper absorber in Long Shutdown 2, which will also enhance further the protection of the remaining magnets in cell 5 (93,94). The beam optics will be adjusted to compensate for the reduced focussing strength of the Q5 assembly due to the missing quadrupole.

Short term effects

This section attempts to provide an overview of the beam-induced quench studies during Run 2 of the LHC with 6.5 TeV protons and 6.37 Z TeV Pb ions. Table 6-2 shows an overview of the results presented in the previous sections with the addition of the results for the Bound Free Pair Production ion quench test (95). Depending on the presence or absence of quench, the estimated power densities provide a lower or upper estimated of the quench level of LHC dipoles.

One can see that, as was described above, the study of the beam induced quench levels is a very complicated process that is sensitive to many different parameters. Despite this, the study shows that a relatively good agreement of the estimated power achieved during the quench tests at the 6.37-6.5 TeV energies exists despite the small amount of cases under study. The results indicate that the lower bound of the steady-state quench level of the dipoles is around 20 mW/cm3. This value will decrease further for operation at 7 TeV due to the higher magnet current compared to 6.37/6.5 TeV in Run 2.

Table 6-2: Overview of the estimated power density achieved during Run 2 quench tests with 6.5 TeV protons and 6.37 Z TeV lead ions.

	Protons Ideal machine	Protons Imperfections	Ions Ideal machine	Ions BFPP Imperfection (96)
Radial averaged peak power density (mW/cm^3) / Magnet	7.7 / MB.A9L7	16.8 / MB.A9L7	6 / MB.B9L7	20 / MB.B11L5
BLM ratio Measured/ simulated	3	1,4	4-5	<1.1
Radial averaged scaled peak power density (mW/cm^3)	23		25-30	20
Radial Averaged peak power density in the last 5 second (mW/cm^3)	13		20-25	20
Quenched?	No		Yes	Yes

These results do raise concern that the leakage of off-momentum particles from the collimation system might pose a limitation for the upcoming HL-LHC era with an increase in beam intensity. The HL design specifications (67) of sustained 1 MW of losses at 7 TeV protons for 1 minute without a quench might not be feasible without intervention. For the ions the collimation system performs even worse at this point with a severe limitation to the loss rate.

For this reason, it was decided (97) to replace a normal LHC dipole in the dispersion suppressor region of IR7 with two more powerful 11 T magnets (on each side of the collimation insertion). In this way, the obtained space can be filled with a “cold section” collimator in an attempt to absorb the majority of the collimation leakage. Nevertheless, the showers escaping the collimator still pose a threat to the newly 11 T dipoles, the quench level of which is still under investigation. The results of this thesis along with the methodology developed was widely used to estimate the effectiveness of this new collimator. The effect of the misalignment on this new DS collimator is under investigation.

Chapter 7 Conclusions and outlook

The work performed in the context of this thesis establish a frame of reference for the performance and predictive power of the current simulation tools available for studying high energy collider collimation.

The benchmark of the simulation chain, involving tracking and beam matter interaction codes, by comparing against beam loss monitor measurements in terms of absolute dose rate signal, is for the first time studied at such a scale. More than 100 BLMs located in more than 500 m of the betatron collimation insertion region of the LHC were examined, with the remarkable overall agreement between measurements and simulations highlighting the power of the simulation tools. The results offered unprecedented insight in the overall and location specific accuracy of the simulation chain for collimation losses.

The detailed study of the BLM signals in the DS region hinted that the tracking studies of an ideal machine were overestimating the cleaning efficiency with BLMs reporting a factor of 3 higher signals than the simulated. A further analysis of the origin of the BLM signals and the individual discrepancies of each BLM hinted that the origin of the discrepancies lies in the assumptions made during the tracking studies. To this end, the effect that collimator misalignment imperfections could have in the overall cleaning efficiency of the machine was presented and strongly suggested that such an imperfection is present in the LHC for beam 2. At the same time the BLM signal investigations of beam 1 hinted that the imperfections are less pronounced than for beam 2 and therefore the possibly better performance of the beam 1 collimators.

Extended data analysis of the BLM signals for the duration of the Run 2 operational period between the years 2015 and 2018 was performed with the aim of quantifying the total number of protons that was lost in the collimation system each year. The

findings were validated by benchmarking against passive dosimeter measurements and simulations for the different years. The obtained results demonstrated that the originally adopted scaling of the losses with the integrated luminosity achieved in the experiments is not suitable for predicting losses in the HL-LHC. In its place, a new scaling method based on the time-integrated beam intensity was examined with promising results for both injection and top energy protons. Simultaneously it was showcased that the radiation impact of the proton losses at injection energy can be safely included in an overall safety margin included in the top energy predictions. Based on the design parameters of the HL-LHC and the scaling factors established in this thesis the total number of expected protons losses in the collimation system for both injection and top energy protons were estimated.

Taking advantage of the above mentioned results, the radiation impact of the design 7 TeV protons in the betatron cleaning insertion region were thoroughly studied. The most impacted elements of the machine were identified by means of energy deposition sharing simulations. The most impacted collimators and magnets were subsequently studied against short and long term radiation impact scenarios.

The collimators under the heaviest radiation load, the horizontal and skew primaries and the first downstream secondary, were examined against short term losses arising from short beam lifetime scenarios. The thesis presented for the first time the effects of a concentrated realistic beam impact on the primary collimators inducing large power density gradients that may lead to material deformation or damage. The contribution to the radiation impact in the collimator jaws of the primary protons and of the secondary particles generated by elastic and inelastic collisions with the collimator blocks were disentangled. The long-term radiation damage was estimated in the form of DPA calculations for the full HL-LHC lifetime providing the reference values to be used for any present and future material irradiation studies. In all cases the current collimator block material of CfC and the future HL-LHC consideration of MoGR were examined and the differences were evaluated and presented.

The radiation impact on the normal conducting magnets located in the proximity of the bulk of the secondary showers escaping the collimators was evaluated. Their

lifetime was estimated based on the cumulative dose absorbed by the organic insulated materials of their coils and the effectiveness of newly designed radiation shields was quantified. Investigations of new mitigation methods based on the thesis findings are ongoing.

Lastly, the peak power density sustained by the SC coils during the collimation quench tests of 2015 was evaluated for both protons and Pb ions. Utilising the benchmark results the predicted values were scaled according to the BLM signal discrepancies observed and the quench margins for the SC magnets were estimated.

References

(1) Brüning OS, Collier P, Lebrun P, Myers S, Ostojic R, Poole J, et al. LHC Design Report. Geneva: CERN; 2004.

(2) LHC smashes beam collision record - BBC News. Available at: https://www.bbc.co.uk/news/10430234. Accessed 12/14/2019, 2019.

(3) LHC sets world record beam intensity | CERN. Available at: https://home.cern/news/press-release/cern/lhc-sets-world-record-beam-intensity. Accessed 12/14/2019, 2019.

(4) Brüning O, Rossi L. The High Luminosity Large Hadron Collider: the new machine for illuminating the mysteries of Universe. : World Scientific Publishing Company; 2015.

(5) Mangano M. Physics at the FCC-hh, a 100 TeV pp collider. arXiv preprint arXiv:1710.06353 2017.

(6) Collaboration TA, Aad G, Abat E, Abdallah J, Abdelalim AA, Abdesselam A, et al. The ATLAS Experiment at the CERN Large Hadron Collider. Journal of Instrumentation 2008 aug;3(08):S08003-S08003.

(7) Collaboration TA, Aamodt K, Quintana AA, Achenbach R, Acounis S, Adamov\'a D, et al. The ALICE experiment at the CERN LHC. Journal of Instrumentation 2008 aug;3(08):S08002-S08002.

(8) Collaboration TC, Chatrchyan S, Hmayakyan G, Khachatryan V, Sirunyan AM, Adam W, et al. The CMS experiment at the CERN LHC. Journal of Instrumentation 2008 aug;3(08):S08004-S08004.

(9) Collaboration TLHC, Alves AA, Filho LMA, Barbosa AF, Bediaga I, Cernicchiaro G, et al. The LHCb Detector at the LHC. Journal of Instrumentation 2008 08/14;3(08):S08005-S08005.

(10) Rossi L. Superconducting magnets for the LHC main lattice. IEEE Trans Appl Supercond 2004;14(2):153-158.

(11) Holzer EB, Dehning B, Effnger E, Emery J, Grishin V, Hajdu C, et al. Beam Loss Monitoring for LHC Machine Protection. Physics Procedia 2012 2012;37:2055-2062.

(12) Dehning B, others. The LHC Beam Loss Measurement System. Conf.Proc. 2007;C070625:4192.

(13) CERN. 2019; Available at: layout.web.cern.ch, 2019.

(14) Redaelli S. Beam cleaning and collimation systems. arXiv preprint arXiv:1608.03159 2016.

(15) Assmann R. Collimators and beam absorbers for cleaning and machine protection. LHC ProjectWorkshop- Chamonix 2005 01;14.

(16) Assmann R, Magistris M, Aberle O, Mayer M, Ruggiero F, Jiménez J, et al. The final collimation system for the LHC 2006.

(17) Bruce R, Assmann R , Boccone V, Bracco C, Brugger M, Cauchi M, et al. Simulations and measurements of beam loss patterns at the CERN Large Hadron Collider. Physical Review Special Topics - Accelerators and Beams 2014 Aug;17(8).

(18) Redaelli S, Alabau Pons C, Assmann R, Bruce R, Giovannozzi M, Muller G, et al. Aperture measurements in the LHC interaction regions. Conf.Proc. 2012 May;C1205201(CERN-ATS-2012-103):MOPPD062. 3 p.

(19) Hermes PD, Wessels JP, Bruce R. Heavy-ion collimation at the Large Hadron Collider: simulations and measurements .

(20) The collimation system: defence against beam loss – CERN Courier. Available at: https://cerncourier.com/a/the-collimation-system-defence-against-beam-loss/. Accessed 12/14/2019, 2019.

(21) Redaelli S. The collimation system: defence against beam loss. CERN Courier 2013(09).

(22) Martinez NF, Abramov A, Azzopardi G, Gorzawski A, Belli E, Boscolo-Meneguolo C, et al. RUN 2 COLLIMATION OVERVIEW.

(23) Mirarchi D, Redaelli S, Wagner J, Hermes P, Salvachua B, Quaranta E, et al. Collimation: experience and performance. 2017.

(24) Bruce R, Mirarchi D, Redaelli S, De Maria R, Giovannozzi M, Hermes P, et al. ${\beta*} $-reach in 2017. 2017.

(25) Giovannozzi M. Considerations on a possible bump to displace the IP in point 5. presentation in the LHC Machine Committee (LMC) 2016;30:2016.

(26) Schmidt F. Mad-X a worthy successor for MAD8? Nuclear Instruments and Methods in Physics Research Section A: Accelerators, Spectrometers, Detectors and Associated Equipment 2006;558(1):47-49.

(27) Deniau L, Giovannozzi M, Jowett J, Latina A, Shreyber I, Burkhardt H, et al. Upgrade of MAD-X for HL-LHC project and FCC studies. 2019.

(28) Schmidt F. SIXTRACK: version 1, single particle tracking code treating transverse motion with synchrotron oscillations in a symplectic manner 1990.

(29) A new version of SixTrack with collimation and aperture interface. Proceedings of the 2005 Particle Accelerator Conference: IEEE; 2005.

(30) Trenkler T, Jeanneret J. K2, a software package evaluating collimation systems in circular colliders (manual) 1994.

(31) Ferrari A, Sala PR, Fasso A, Ranft J. FLUKA: A multi-particle transport code (Program version 2005) 2005.

(32) Böhlen T, Cerutti F, Chin M, Fassò A, Ferrari A, Ortega P, et al. The FLUKA code: developments and challenges for high energy and medical applications. Nuclear data sheets 2014;120:211-214.

(33) FLAIR: a powerful but user friendly graphical interface for FLUKA. Proc. Int. Conf. on Mathematics, Computational Methods & Reactor Physics (M&C 2009), Saratoga Springs, New York; 2009.

(34) SixTrack-FLUKA active coupling for the upgrade of the SPS scrapers. Conf. Proc.; 2013.

(35) Mereghetti A, Ortega P, Fiascaris M, Cerutti F, Pastor Sinuela D, Zou Y, et al. SixTrack for cleaning studies: 2017 updates. 2017.

(36) Hermes P, Cerutti F, Vlachoudis V, Jowett J, Valentino G, Mirarchi D, et al. Simulation of heavy-ion beam losses with the SixTrack-FLUKA active coupling. 2016.

(37) Mereghetti A, Boccone V, Cerutti F, Versaci R, Vlachoudis V. The FLUKA linebuilder and element database: tools for building complex models of accelerator beam lines. IPAC2012, WEPPD071 2012:2687.

(38) Salvachua B, Mirarchi D, Redaelli S, Wollmann D, Quaranta E, Valuch D, et al. Collimation quench test with 4 TeV proton beams 2014.

(39) Quench tests at the Large Hadron Collider with collimation losses at 3.5 Z TeV. Proc. HB2012 Workshop; 2012.

(40) Salvachua Ferrando BM, Wollmann D, Auchmann B, Valloni A, Valentino G, Mirarchi D, et al. Collimation quench test with 6.5 TeV proton beams 2016.

(41) Hermes PD, Hofle W, Wollmann D, Zerlauth M, Auchmann B, Quaranta E, et al. LHC heavy-ion collimation quench test at 6.37 Z TeV 2016.

(42) Auchmann B, Baer T, Bednarek M, Bellodi G, Bracco C, Bruce R, et al. Testing beam-induced quench levels of LHC superconducting magnets. Physical Review Special Topics-Accelerators and Beams 2015;18(6):061002.

(43) Skordis E, Cerutti F, Vlachoudis V, Ortega P, Bruce R, Redaelli S, et al. Impact of beam losses in the LHC collimation regions 2015.

(44) Skordis E, Cerutti F, Vlachoudis V, Bruce R, Redaelli S, Mereghetti A, et al. Study of the 2015 top energy LHC collimation quench tests through an advanced simulation chain. 2017.

(45) Hofle W, Assmann R, Redaelli S, Schmidt R, Valuch D, Wollmann D, et al. Controlled transverse blow-up of high-energy proton beams for aperture measurements and loss maps. Proceedings of IPAC 2012;12:4059-4061.

(46) Shaposhnikova E, Mataguez S, Manglunki D, Funken A, Coupard J, Meddahi M, et al. LHC injectors upgrade (LIU) project at CERN 2016.

(47) A. Mereghetti et al. Tracking simulations of protons quench test. CERN 2016 7th March:https://indico.cern.ch/event/504706/contributions/1182928/attachments/1239638/1829553/mereghettivalloni.pdf.

(48) Roderick C. Handling of BLM abort thresholds in the LHC. 2011.

(49) Schaumann M, Chetvertkova V, Auchmann B, Giachino R, Alemany Fernandez R, Jowett J, et al. LHC BFPP Quench Test with Ions (2015) 2016.

(50) Lechner A, Auchmann B, Baer T, Castro CB, Bruce R, Cerutti F, et al. Validation of energy deposition simulations for proton and heavy ion losses in the CERN Large Hadron Collider. Physical Review Accelerators and Beams 2019;22(7):071003.

(51) Bahamonde Castro C, Auchmann B, Cerutti F, Jowett J, van Weelderen R, Bruce R, et al. Power deposition in LHC magnets due to bound-free pair production in the experimental insertions. 2016.

(52) Assmann R, Jeanneret J, Kaltchev D. Efficiency for the imperfect LHC collimation system 2002.

(53) A. Mereghetti et al. presentation on "Cleaning Studies with TCP Misalignments". CERN 2016 19 Sep

2016:https://indico.cern.ch/event/570008/contributions/2305346/attachments/1339214/2016471/AM_2016-09-19.pdf.

(54) Roesler S, Engel R, Ranft J. The monte carlo event generator dpmjet-iii. Advanced Monte Carlo for radiation physics, particle transport simulation and applications: Springer; 2001. p. 1033-1038.

(55) Fasso A, Ferrari A, Roesler S, Sala P, Ballarini F, Ottolenghi A, et al. The physics models of FLUKA: status and recent development. arXiv preprint hep-ph/0306267 2003.

(56) Ferrari A, Sala PR, Fasso A, Ranft J. Fluka. CERN-library in: http://fluka.web.cern.ch/fluka 2005;55(99):100.

(57) FLUKA: performances and applications in the intermediate energy range. Proceedings of the Specialists Meeting on Shielding Aspects of Accelerators, Targets & Irradiation Facilities, Arlington, USA; 1994.

(58) LhcDataStorage. Available at: https://twiki.cern.ch/twiki/bin/view/ABPComputing/LhcDataStorage. Accessed 12/15/2019, 2019.

(59) Bilko K, Kadi Y, Brugger M, Stein O, Garcia Alia R, Harden F. Detailed Analysis Of The Baseline Dose Levels And Localized Radiation Spikes In The Arc Sections Of The Large Hadron Collider During Run 2. 2019.

(60) Alemany R, Lamont M, Page S. Functional specification: LHC Modes. ref.doc LHC-OP-ES-0005-10-00 2007.

(61) Eaton JW, Bateman D, Hauberg S. GNU Octave manual. : Network Theory Ltd. Bristol, UK; 2002.

(62) Coninckx F, Schönbacher H, Tavlet M, Paic G, Razem D. Comparison of high-dose dosimetry systems for radiation damage studies in collider detectors and accelerators. Nuclear Instruments and Methods in Physics Research Section B: Beam Interactions with Materials and Atoms 1993;83(1-2):181-188.

(63) Lamont M. Estimates of annual proton doses in the LHC 2005.

(64) Valentino G, Buffat X, Redaelli S, Kirchner D. A systematic measurement analyzer for LHC operational data. 2015.

(65) Iadarola G, Rumolo G, Arduini G, Bartosik H, Shaposhnikova E, Maury Cuna G, et al. Electron cloud and scrubbing studies for the LHC 2013.

(66) R. Garcia Alia et al. Presentation on "Update on IP7 losses from 2018 experience". 2018 31st August,

2018:https://indico.cern.ch/event/739443/contributions/3052406/attachments/1708665/2753856/2018-08_ColUSM107_IP7_scaling.pdf.

(67) Apollinari G, Béjar Alonso I, Brüning O, Lamont M, Rossi L. High-luminosity large hadron collider (HL-LHC): Preliminary design report 2015.

(68) LHC Availability 2016: Proton Run. 7th Evian Workshop on LHC beam operation (CERN, Geneva, Switzerland; 2016.

(69) Rossi L, Brüning O. High luminosity large hadron collider: A description for the European strategy preparatory group 2012.

(70) Koutchouk JP, Szeberenyi A. EuCARD: final project report. ; 2014.

(71) EuCARD-2: Enhanced European Coordination for Accelerator Research & Development |. Available at: http://eucard2.web.cern.ch/. Accessed 12/20/2019, 2019.

(72) Accelerator Research and Innovation for European Science and Society. Available at: https://aries.web.cern.ch/. Accessed 12/20/2019, 2019.

(73) Quaranta E. Investigation of collimator materials for the High Luminosity Large Hadron Collider 2017.

(74) Capeans M, Akesson T, Anghinolfi F, Arik E, Baker O, Baron S, et al. Recent aging studies for the ATLAS transition radiation tracker. IEEE Trans Nucl Sci 2004;51(3):960-967.

(75) Quaranta E, Bertarelli A, Bruce R, Carra F, Cerutti F, Lechner A, et al. Modeling of beam-induced damage of the LHC tertiary collimators. Physical Review Accelerators and Beams 2017;20(9):091002.

(76) Assmann R, Jeanneret J, Schmidt R, Wenninger J, Burtin G, Hayes M, et al. Requirements for the LHC collimation system 2002.

(77) E. Caridaeo et al. Why do we need coated collimators? Available at: https://indico.cern.ch/event/751331/contributions/3113704/attachments/1705707/2748308/Why_coat_the_collimators.pdf. Accessed 12/20/2019, 2019.

(78) Carra F, Bahamonde Castro C, Bertarelli A, Gobbi G, Guardia-Valenzuela J, Pasquali M, et al. TCSPM Compatibility with HL-LHC Slow Loss Scenarios for CFC and MoGr jaws. Available at: https://indico.cern.ch/event/676105/contributions/2767650/attachments/1554131/2444300/LS2Materials_SlowLosses_November2017.pdf. Accessed 12/20/2019, 2019.

(79) Redaelli S, Bertarelli A, Gobbi G, Bruce R, Carra F, Biancacci N, et al. Staged implementation of low-impedance collimation in IR7: plans for LS2 2019.

(80) F. Carra E. Skordis et al. Presentation on "TCSPM Compatibility with HL-LHC Slow Loss Scenarios for CFC and MoGr jaws". 2017 08/11/2017:https://indico.cern.ch/event/676105/contributions/2767650/attachments/1554131/2444300/LS2Materials_SlowLosses_November2017.pdf.

(81) Mechanical robustness of HL-LHC collimator designs. Journal of Physics: Conference Series: IOP Publishing; 2019.

(82) MacFarlane R, Barrett R, Muir D, Boicourt R. NJOY nuclear data processing system: user's manual 1978.

(83) Battistoni G, Boehlen T, Cerutti F, Chin PW, Esposito LS, Fassò A, et al. Overview of the FLUKA code. Ann Nucl Energy 2015;82:10-18.

(84) Romaniuk RS. ARIES 2018-Infrastructure, Innovation, Outreach. International Journal of Electronics and Telecommunications 2019;65(1):119-124.

(85) Tavlet M, Fontaine A, Schönbacher H. Compilation of radiation damage test data, pt.2. Index des resultats d'essais de radioresistance, t.2; 2nd ed. Geneva: CERN; 1998.

(86) Bottura L, Fessia P. What could stop us and when. 2014.

(87) Tavlet M, Fontaine A, Schönbacher H. Compilation of radiation damage test data, pt.2. Index des resultats d'essais de radioresistance, t.2; 2nd ed. Geneva: CERN; 1998.

(88) Fessia P, Mariani N, Cerutti F, Gallay E, Guinchard M, Skordis E, et al. LHC Normal Conducting Magnets Toward HL-LHC and Beyond: Life Span Evaluations, Corrective Actions, and Future Upgrades. IEEE Trans Appl Supercond 2016;26(4):1-5.

(89) Fessia P, Mariani N. MBW-MQW in the LHC Considerations on expected life and available options. Available at: https://indico.cern.ch/event/508156/contributions/2028705/attachments/1243607/1830227/warm_magnets_16_10_pfessia_TRIUMF_visit2.pdf. Accessed 12/20/2019, 2019.

(90) Home | CERN. Available at: https://home.cern/. Accessed 12/20/2019, 2019.

(91) Superconductivity and the LHC: the early days – CERN Courier. Available at: https://cerncourier.com/a/superconductivity-and-the-lhc-the-early-days-2/. Accessed 12/20/2019, 2019.

(92) Simulation of Electro-Thermal Transients in Superconducting Accelerator Magnets with COMSOL Multiphysics®. Proceedings of the European COMSOL Conference; 2016.

(93) Improved Protection of the Warm Magnets of the LHC Betatron Cleaning Insertion. Proceedings, 8th International Particle Accelerator Conference (IPAC 2017): Copenhagen, Denmark, May 14-19, 2017}; 2017.

(94) BE-ABP SR, BE-ABP RB, BE-ABP AM, Aberle O, Albertone J, Adorisio C, et al. Installation of New Passive Absorbers (TCAPM) for Warm Magnet Protection in IR7. 2018.

(95) Schaumann M, Chetvertkova V, Auchmann B, Giachino R, Alemany Fernandez R, Jowett J, et al. LHC BFPP Quench Test with Ions (2015) 2016.

(96) Bahamonde Castro C, Auchmann B, Cerutti F, Jowett J, van Weelderen R, Bruce R, et al. Power deposition in LHC magnets due to bound-free pair production in the experimental insertions. 2016.

(97) International Review of the HL-LHC Collimation System (11-12 February 2019): Contribution List · Indico. Available at: https://indico.cern.ch/event/780182/contributions/. Accessed 12/20/2019, 2019.